

Summer 2021

Development and Applications of Adjoint-Based Aerodynamic and Aeroacoustic Multidisciplinary Optimization for Rotorcraft

Ramiz Omur Icke
Old Dominion University, eromir@gmail.com

Follow this and additional works at: https://digitalcommons.odu.edu/mae_etds



Part of the [Acoustics, Dynamics, and Controls Commons](#), [Aerospace Engineering Commons](#), and the [Other Physics Commons](#)

Recommended Citation

Icke, Ramiz O.. "Development and Applications of Adjoint-Based Aerodynamic and Aeroacoustic Multidisciplinary Optimization for Rotorcraft" (2021). Doctor of Philosophy (PhD), Dissertation, Mechanical & Aerospace Engineering, Old Dominion University, DOI: 10.25777/2vh6-pr05
https://digitalcommons.odu.edu/mae_etds/336

This Dissertation is brought to you for free and open access by the Mechanical & Aerospace Engineering at ODU Digital Commons. It has been accepted for inclusion in Mechanical & Aerospace Engineering Theses & Dissertations by an authorized administrator of ODU Digital Commons. For more information, please contact digitalcommons@odu.edu.

DEVELOPMENT AND APPLICATIONS OF ADJOINT-BASED AERODYNAMIC AND
AEROACOUSTIC MULTIDISCIPLINARY OPTIMIZATION FOR ROTORCRAFT

by

Ramiz Omur Icke

B.Sc. June 2011, Istanbul Technical University, Turkey
M.Sc. Dec 2015, Istanbul Technical University, Turkey

A Dissertation Submitted to the Faculty of
Old Dominion University in Partial Fulfillment of the
Requirements for the Degree of

DOCTOR OF PHILOSOPHY

AEROSPACE ENGINEERING

OLD DOMINION UNIVERSITY
August 2021

Approved by:

Oktay Baysal (Director)

Leonard V. Lopes (Member)

Boris Diskin (Member)

Colin Britcher (Member)

Miltos Kotinis (Member)

ABSTRACT

DEVELOPMENT AND APPLICATIONS OF ADJOINT-BASED AERODYNAMIC AND AEROACOUSTIC MULTIDISCIPLINARY OPTIMIZATION FOR ROTORCRAFT

Ramiz Omur Icke
Old Dominion University, 2021
Director: Oktay Baysal

Urban Air Mobility (UAM) is one of the most popular proposed solutions for alleviating traffic problems in populated areas. In this context, the proposed types of vehicles mainly consist of rotors and propellers powered by electric motors. However, those rotary-wing components can contribute excessively to noise generation. Therefore, a significant noise concern emerges due to urban air vehicles in or around residential areas. Reducing noise emitted by air vehicles is critically important to improve public acceptance of such vehicles for operations in densely populated areas.

Two main objectives of the present dissertation are: (1) to expand the multidisciplinary optimization to utilize adjoint-based aeroacoustic and aerodynamic sensitivities; (2) to optimize the shape of proprotor blades to improve the overall performance of selected rotorcraft from both aerodynamic and aeroacoustic perspectives.

This dissertation reports on the development and application of an unsteady discrete adjoint solver for aerodynamic and aeroacoustic coupling to obtain an improved design for quieter rotorcraft. The optimization framework developed through this dissertation can be utilized for multiple flight conditions, multiple receivers, and multiple optimization objectives within the same design process. SU2-based code development involves the implementation of aeroacoustic analysis, adjoint computations, and integrations into a multidisciplinary rotorcraft optimization suite. A computational aeroacoustics tool is embedded into the SU2-suite to predict

the propagation of the emitted noise from the moving sources with high fidelity. Capabilities of the developed computational aeroacoustics tool are demonstrated for a range of rotor, propeller, and proprotor applications, and they are verified by comparing with wind tunnel data whenever it is available. The aeroacoustic tool also computes sensitivities with respect to the conserved variables and grid coordinates by employing the algorithmic differentiation method. Integration of an acoustic solver into the discrete adjoint solver and related modifications enable the code to compute aeroacoustic sensitivities with respect to the design variables.

Applying the developed optimization framework for a proprotor aims to reduce the noise radiation without sacrificing the required aerodynamic performance value. As an outcome of the optimization during forward-flight and hover, the reshaped blade design emits and propagates lower noise levels as perceived by multiple observers.

The major *contributions* are: (1) a multidisciplinary optimization framework that presents an optimized rotorcraft design for better aeroacoustics and aerodynamics; (2) a novel adjoint-based formulation for aeroacoustic sensitivities with respect to design variables; (3) single acoustic objective function including multiple flight conditions and multiple microphone positions; (4) implementation of Farassat 1A formulation into opensource software, SU2, to compute noise propagation emitted from moving sources.

In summary, this dissertation provides the results with high fidelity, a well-integrated and rapidly converging optimization tool to improve the rotorcraft's aeroacoustic performance while retaining or improving the aerodynamic performance. Among the conclusions are the following: (1) Computational fluid dynamics analyses (SU2-CFD) can produce accurate results for various rotorcraft applications. (2) The developed aeroacoustic code predicts noise propagation emitted from propellers, rotors, and proprotors with high-fidelity. (3) The acoustic interaction between

propeller and wing components can be assessed by employing the aeroacoustic solver. (4) The multidisciplinary optimization framework successively reduces noise level emitted by a proprotor in multiple flight configurations. (5) The optimized design improves emitted noise radiation while satisfying the given aerodynamic constraint(s).

Copyright, 2021, by Ramiz Omur Icke, All Rights Reserved.

This dissertation is dedicated to:

Those who committed their lives to science and followed their idea eternally,

And

My beloved family.

ACKNOWLEDGMENTS

I am deeply grateful to my advisor, Prof. Oktay Baysal, for guiding, enlightening, and supporting me throughout my research. He always trusted me to go forward and motivated me to stay on the lane in this journey. In this unprecedented pandemic period, he never left me alone and always made me believe in myself.

I would like to thank Dr. Leonard Lopes for supporting this research with his expertise and guidance in aeroacoustic developments. I would like to express my appreciation to Dr. Boris Diskin, who has shared his experiences in computational fluid dynamics and adjoint solvers. I would also like to thank the other committee members for their support during my time at the Old Dominion University and for reading this dissertation.

I have always felt the support of my family from afar. They stood behind me through these grueling times. My father has been a model of idealism, principle, and commitment for me. My mother always dedicated herself to make me feel happy and appreciated in my life. My thoughtful sister has never bothered to teach me her life experiences from childhood to today. I wish to thank my girlfriend, Nur Erol, for all her love, support, and understanding. Her untiring efforts for believing in me always encouraged me to accomplish this achievement. I would also like to thank my friends, Ege Konuk, Dr. Jung I. Shu, and Andy Moy, for supporting me along the way.

A NASA Langley Research Center grant has supported this work through the National Institute of Aerospace. The technical monitor was Dr. Leonard Lopes. I also acknowledge the vast computer resources provided by the High Performance Computing of Old Dominion University.

NOMENCLATURE

Acronyms

3BHTP	Three-Bladed Helically Twisted Proprotor
4BITR	Four-Bladed Ideally Twisted Rotor
AD	Algorithmic Differentiation
ALE	Arbitrary Lagrangian Eulerian
ANOPP2	Aircraft NOise Prediction Program 2
BBN	BroadBand Noise
BPF	Blade Passage Frequency
BVI	Blade-Vortex Interaction
CA	Continuous Adjoint
CAA	Computational AeroAcoustics
CFD	Computational Fluid Dynamics
CPU	Computer Power Unit
CT	Caradonna-Tung Rotor
DA	Discrete Adjoint
DDES	Delayed Detached Eddy Simulation
DES	Detached Eddy Simulation
DFT	Discrete Fourier Transform
eVTOL	Electric Vertical Take-Off and Landing
F1A	Farassat 1A
FAA	Federal Aviation Administration

FFD	Free Form Deformation
FGMRES	Flexible Generalized Minimum Residual
FWH	Ffowcs Williams-Hawkings
HPC	High Performance Computer
HSI	High-Speed Impulsive
JST	Jameson-Schmidt-Turkel
LEE	Linear Euler Equations
LES	Large Eddy Simulation
LSAWT	Low Speed Aeroacoustic Wind Tunnel
MPI	Message Passing Interface
NASA	National Aeronautics and Space Administration
PDEs	Partial Differential Equations
RANS	Reynolds-Averaged Navier-Stokes
RPM	Rotation Per Minute
SA	Spalart-Allmaras
SFT	Slow Fourier Transform
SPL	Sound Pressure Level
SU2	Stanford University Unstructured
UAM	Urban Air Mobility
URANS	Unsteady Reynolds-Averaged Navier-Stokes
WIPP	Workshop for Integrated Propeller Prediction

Greek Symbols

α	Design variable vector
----------	------------------------

α^{new}	New design variable vector
Γ_∞	Far-field boundary of the flow domain
δ_{ij}	Kronecker delta
$\delta(f)$	Dirac delta functions
$\Delta\alpha$	Increment vector for design variables
η	Propulsive efficiency
θ	Longitudinal angle
κ	Free constant in SA equations, 0.41
μ_{tot}	Total viscosity
μ_{dyn}	Dynamic viscosity
μ_{tur}	Turbulent viscosity
μ_{tot}^*	Effective thermal conductivity
\square^2	D'Alembertian operator
ρ	Fluid density
ρ_0	Freestream density
σ	Rotor solidity
	Free constant in SA equations
τ	Source time
$\bar{\bar{\tau}}$	Viscous stress tensor
ν	Viscosity
$\tilde{\nu}$	Transported turbulent quantity, eddy viscosity
ϕ	Twist angle of airfoil section
φ	Azimuthal angle

χ Ratio of eddy viscosity and viscosity

Ω Flow domain

$\vec{\omega}$ Fluid vorticity

Alphabets

A Area

A_0, A_1 Coefficient in T_1 for F1A formulation

A_m Complex coefficient in the frequency domain

B_0, B_1 Coefficient in T_2 for F1A formulation

c Speed of sound

C_0, C_1 Coefficient in T_3 for F1A formulation

c_{b1} Free constant in SA equations

c_p Specific heat at constant pressure

C_T Thrust coefficient

c_{v1} Free constant in SA equations

CG_{Face_i} Position of center of gravity for $Face_i$

$CG_{edge_{i-j}}$ Position of center of gravity for edge between i and j points

d Distance to nearest wall

D_0, D_1 Coefficient in T_4 for F1A formulation

dS Area of finite element

Local panel area

E Total energy

F Custom objective function for acoustics

f Frequency

F_{FF}	Part of the objective function for forward flight
F_H	Part of the objective function for hover
\vec{F}_{ale}^c	Convective fluxes
\vec{F}^v	Viscous fluxes
f_{v1}	Coefficient in SA equations
f_w	Non-dimensional function in SA equations
G_{ppm}	Power spectral density
G^n	Iteration of pseudo time stepping
h	Constant height of microphone position
	Step value for complex differentiation
$H(f)$	Heaviside functions
$Im(...)$	Imaginary part of the input
I	Acoustic intensity
$I(...)$	Interpolation function
$\bar{\bar{I}}$	Tensor for Kronecker delta
J	Objective function
K	Coefficient in F1A formulation
L	Lagrangian function
M	Local Mach number
\dot{M}_i	Time derivative of local Mach number
M^n	Mesh deformation equation
N	Number of time steps
\vec{N}_i	Normal vector

n_i	Position of node i
	Unit outward normal
p	Static pressure
p'	Acoustic pressure
p_∞	Freestream pressure
p'_T	Thickness noise
p'_L	Loading noise
p_{rms}	Root mean squared pressure fluctuation
p_{ref}	Reference pressure
Pr_d	Dynamic Prandtl number
Pr_t	Turbulent Prandtl number
Q	Generic source term
R	Gas constant
\mathcal{R}	Residual function
r	Radiation vector
\hat{r}_i	Unit radiation vector
\vec{r}	Position vector
R/D	Nondimensional radial distance
S	Surface boundary of the flow domain
T	Period of acoustic pressure time history
	Temperature
T_{ij}	Lighthill stress tensor
T_1, T_2, T_3, T_4	Breakdown terms of acoustic formulation

t	Observer time
t^*	Desired observer time
U	State variable vector
U	Conservative variables
\bar{U}^n	Flow adjoint vector
\vec{U}_0	Freestream velocity
\vec{u}_Ω	Velocity of a moving domain
\vec{v}	Three-dimensional vector for flow speed
v_n	Surface velocity dotted with the surface normal vector
v_i	Local velocity
W	Acoustic power
W_A	A-weighting function
X	Grid coordinate vector
\bar{X}^n	Grid adjoint vector

TABLE OF CONTENTS

	Page
LIST OF TABLES	xvii
LIST OF FIGURES	xviii
Chapter	
1. INTRODUCTION	1
1.1 Problem Definition	3
1.2 Literature Survey	6
1.2.1 Acoustic Prediction Methods for Rotorcraft	6
1.2.2 Adjoint-based Optimization	8
1.2.3 Capabilities of SU2 in Design Optimization and Aeroacoustics.....	11
1.3 Dissertation Layout.....	13
2. COMPUTATIONAL FLUID DYNAMICS	14
2.1 Governing Equations for Compressible and Unsteady Flow	14
2.2 Rotating Reference Frame	16
2.3 Numerical Schemes	17
3. COMPUTATIONAL AEROACOUSTICS	18
3.1 Ffowcs Williams and Hawking Equation	18
3.2 Farassat 1A Formulation.....	18
4. OPTIMIZATION	21
4.1 Optimization Framework.....	21
4.2 Sensitivities of Gradient-Based Optimization	22
4.3 Objective Functions	26
4.3.1 Method-1	27
4.3.2 Method-2	27
4.3.3 Method-3	28
5. NUMERICAL IMPLEMENTATIONS	32
5.1 F1A Implementation	32
5.1.1 Discretization.....	32
5.1.2 Normal and Area Computation	35
5.1.3 Velocity Computation	37
5.1.4 Computation of Radiation Vector and Observer Time.....	38
5.1.5 Fourier Transform	39
5.1.6 Flow Chart of F1A Solver	40
5.1.7 Parallel Computation	43
5.2 Sensitivities.....	45

Chapter	Page
5.2.1 Algorithmic Differentiation in F1A Solver	45
5.2.2 Complex Differentiation in F1A Solver	48
5.3 SU2 integration.....	49
5.3.1 Modifications on SU2 libraries	50
5.3.2 Extensions in SU2 Configuration File for the Developed Features	52
6. AEROACOUSTICS APPLICATIONS	55
6.1 Flow Past Sphere in Wind Tunnel	55
6.1.1 Rotating Sphere	59
6.2 Caradonna-Tung Rotor	60
6.2.1 Computational Cost Analysis of SU2-CAA Code	65
6.3 XV-15 Tiltrotor.....	67
6.4 Three-bladed Helically Twisted Proprotor	72
6.4.1 Aerodynamic Results.....	73
6.4.2 Aeroacoustic Results	75
6.5 Workshop for Integrated Propeller Prediction (WIPP)	81
6.5.1 Aerodynamic Results.....	83
6.5.2 Aeroacoustic Results	87
6.6 Four-bladed Ideally Twisted Rotor/Propeller	94
6.6.1 Aeroacoustic Results	96
7. APPLICATIONS OF DESIGN OPTIMIZATION.....	101
7.1 Sensitivities.....	101
7.2 Parameterization	104
7.3 Results.....	107
7.3.1 Optimization-I	107
7.3.2 Optimization-II	115
7.3.3 Optimization-III.....	121
8. CONCLUSIONS AND FUTURE DIRECTIONS	128
APPENDIX.....	131
Spalart Allmaras Turbulence Model [68]	131
REFERENCES	132
VITA.....	139

LIST OF TABLES

Table	Page
1. Comparison of CFD and experimental data for XV-15 rotor.....	68
2. Comparison of CFD and wind tunnel results for three-bladed helically twisted proprotor (3BHTP).....	74
3. Number of nodes and percentage of thrust error of the CFD simulations with different grid densities.	84
4. Sensitivity verification of 3BHTP.	102
5. Finite difference validation of the sensitivity for a design variable (movement of the tip inward direction).	103
6. Comparisons for Aerodynamic performance outputs of baseline and optimized design for two flight configurations	122
7. Wall clock time breakdowns for the optimization process.....	127

LIST OF FIGURES

Figure	Page
1. NASA's X-57 Maxwell aircraft [5].	4
2. Tilt wing concept, Langley Aerodrome No. 8, (a) forward flight mode and (b) hovering mode [6].	5
3. Tilt-rotor concept: (a) VTOL configuration; (b) cruise configuration [9].	6
4. Flowchart of computation of adjoint governing equations by Continuous Adjoint (CA) and Discrete Adjoint (DA) methods.	9
5. The gradient-based optimization cycle.	22
6. Flowchart of adjoint sensitivities for coupled aerodynamics and aeroacoustics.	25
7. Flowchart of adjoint sensitivities for coupled aerodynamics and aeroacoustics, including only shape variables.	26
8. Sample demonstration of the coordinate system of microphone position.	29
9. Sample demonstration of a surface grid element with definitions.	36
10. Area of a panel and related definitions.	36
11. Flowchart of F1A solver.	41
12. Demonstration of the halo layer and edge points.	44
13. Registration flags for dependent variables.	46
14. Flowchart of F1A solver for variable registration.	47
15. Flowchart of CAA solver for acoustic adjoints.	48
16. Placement of SU2-CAA in SU2 suite.	50
17. Modifications on SU2_CFD and Common folders.	51

Figure	Page
18. Modifications on SU2_DOT and SU2_PY folders.....	51
19. Configurations for aeroacoustic definition.	53
20. Configurations for optimal design definition.....	54
21. (a) Computed pressure coefficient distribution on a unit sphere and (b) its wake.	56
22. Comparison of F1A computed pressure propagation with CFD results. $M_\infty=0.5$ and the observer at ten diameters away.	57
23. Comparison of F1A computed pressure propagation with CFD results. $M_\infty= 0.5$ and the observer at 14 diameters away.	57
24. Comparison of F1A computed pressure propagation with CFD results. $M_\infty = 0.1$ and the observer at ten diameters away.	58
25. Comparison of F1A computed pressure propagation with CFD results. $M_\infty = 0.1$ and the observer at 14 diameters away.	58
26. Comparison of F1A-computed pressure propagation with CFD results for a rotating unit sphere.	60
27. CFD simulations of Caradonna-Tung rotor: Mach distribution over blades and isosurfaces for tip vorticities.	61
28. Comparison of SU2 and experiment [85] for pressure coefficient distribution along the airfoil at $r = 0.96R$	62
29. Comparison of SU2 and experiment [85] for pressure coefficient distribution along the airfoil at $r = 0.89R$	62
30. Comparison of SU2-CAA and ANOPP2 predictions for the observer location at 100- diameter away in-plane direction.	63

Figure	Page
31. Directivity comparisons of root means squared acoustic pressure values for the observers.	64
32. Distribution of acoustic dipole term over instantaneous sigma surface obtained from (a) SU2-CAA and (b) ANOPP2.	65
33. Number of observers versus wall clock time for different CPUs and time steps.	66
34. Number of observers versus memory usage for different CPUs and time steps.	67
35. (a) Photo of XV-15 rotorcraft; (b) CAD model of XV-15 Rotor.	68
36. Instantaneous vorticity isosurfaces ($Q\text{-criterion}=2s - 2$) in the XV-15 rotor wake.	69
37. Rotor-oriented microphone positions, both one rotor diameter away from the tiltrotor center: (a) Mic 1 located 45 degrees above the rotor plane, and (b) Mic 2 in-plane.	69
38. Comparison of CAA and CFD results for microphone 1 (45 degrees above the rotor plane).....	70
39. Comparison of CAA and CFD results for microphone 2 (in-plane position).....	70
40. Acoustic pressure comparison of SU2 and ANOPP2 for the microphone located at 100 diameters away at 45 degrees above the rotor plane.....	71
41. Acoustic pressure comparison of SU2 and ANOPP2 for the microphone located at 100 diameters away in rotor plane.	71
42. Acoustic pressure comparison of SU2 and ANOPP2 for the microphone located at 100 diameters away at 45 degrees below the rotor plane.....	72
43. Three-bladed, helically twisted propeller (3BHTP): (a) CAD model and (b) wind tunnel model in LSAWT.....	73

Figure	Page
44. Instantaneous vorticity isosurfaces around proprotor and skin friction distribution over the blades: (a) propeller configuration with $Q\text{-criterion}=150\text{ s}^{-2}$; (b) rotor configuration with $Q\text{-criterion}=800\text{ s}^{-2}$.	75
45. Coordinate system for microphone position.	76
46. Time history of acoustic pressure for an observer, located at $R/D=10.5$, $\theta=114.6^\circ$, and $\phi=40^\circ$ (observer-14).	77
47. Time history of acoustic pressure for an observer, located at $R/D=9.5$, $\theta=94.6^\circ$, and $\phi=40^\circ$ (observer-10).	77
48. Spectral comparison of SU2-CAA predictions and LSAWT data for: (a) observer-10 and (b) observer-14.	78
49. Sound pressure values corresponding to fundamental blade passage frequency versus observer locations at different θ angles (with constant $x/D_{prop} = 3.73$ and $y/D_{prop}=4.45$) for: (a) forward flight, and (b) hover conditions.	80
50. (a) Wind tunnel model from WIPP; (b) CAD/CFD model.	82
51. (a) Moving (relative to the stationary) mesh for the rotating hub and the propeller and (b) Computational domain; dimensions normalized by propeller diameter (D).	83
52. (a) Pressure coefficient distribution over wing mounted propeller, WIPP, and (b) drag coefficient time history of CFD analysis.	84
53. Probe line locations corresponding to WIPP geometry: (a) $x=1.5\text{ in}$; (b) $x=5\text{ in}$; (c) $x=13\text{ in}$; and (d) $x=21\text{ in}$.	85
54. Nondimensional axial velocity, U/a_∞ , distributions along the wake line on successively finer grids located at: (a) $x=1.5\text{ in}$., (b) $x=5\text{ in}$., (c) $x=13\text{ in}$., and (d) $x=21\text{ in}$.	86

Figure	Page
55. Nondimensional swirl velocity, $W/a\infty$, distributions along the wake located at (a) $x=1.5$ in., (b) $x=5$ in., (c) $x=13$ in., and (d) $x=21$ in., on successively finer grids.	87
56. Coordinate system for microphone position.	88
57. Time history of acoustic pressure for an observer, x : $R/D=100$, $\theta=90^\circ$ and $\varphi=180^\circ$	88
58. Time history of acoustic pressure for an observer, x ($R/D=100$, $\theta=90^\circ$ and $\varphi=0^\circ$).	90
59. (a) p' distribution over sigma surface of propeller blades and nacelle, (b) Acoustic footprints on full-body WIPP geometry.	91
60. Demonstration of the microphone (observer) positions relative to center of the propeller at 100-diameter away in (a) negative and (b) positive z -direction with different x/D distances.	92
61. Theta vs. BPF SPL for full body and isolated propeller configurations for the observer points located between (-45) - (-135) degrees at the 100-diameter away in the negative z -direction.	93
62. Theta vs BPF SPL for full body and isolated propeller configurations for the observer points located between 45 - 135 degrees at the 100-diameter away in positive z -direction.	94
63. (a) Instantaneous pressure distribution over wing and ideally-twisted-rotor, 4BITR, and (b) drag coefficient time history of CFD analysis.	96
64. Coordinate system for microphone position.	97
65. Time history of acoustic pressure for an observer, x ($R/D=10$, $\theta=90^\circ$ and $\varphi=90^\circ$).	98
66. Sound pressure values corresponding to fundamental blade passage frequency vs. observer locations at different θ angles (with constant $y/D_{prop} = 10$ and $\varphi = 90^\circ$).	98
67. Acoustic scattering on the wing surface due to the excitation by propeller wake flow.	99

Figure	Page
68. Different positions of the wing relative to the propeller with constant height ($dy/R=0.5$)....	99
69. Noise emitted from the propeller for different wing-propeller configurations at different microphone locations.	100
70. Sensitivities with respect to the grid coordinates; (a) $\partial J/\partial x$; (b) $\partial J/\partial y$; and (c) $\partial J/\partial z$ on the blade surface framed with red dashed line.	103
71. FFD boxes wrapping three blades of the proprotor.	105
72. FFD boxes wrapping the blade and parameterization of control points.	105
73. Radial sections of baseline and optimized blade geometries.	108
74. Blade deformation at the tip region.	109
75. Comparison for SPL of baseline and optimized proprotor for the forward flight and hover cases.	110
76. Comparison for SPL corresponding to the second and third harmonics of baseline and optimized proprotor for: (a) the forward flight, (b) hover configurations.	111
77. Comparison of the baseline and optimized surface for observer-10 ($\theta = 94.6^\circ$) in (a) time domain and (b) frequency domain.	112
78. Comparison of the baseline and optimized surface for observer-14 ($\theta = 114.6^\circ$) in (a) time domain and (b) frequency domain.	113
79. Thickness noise and loading noise components of the acoustic pressure emitted from baseline and optimized surfaces for: (a) observer-10, (b) observer-14.	114
80. Revised FFD boxes and parameterization of control points.	115
81. (a) Pressure and (b) suction side of optimized (green) and baseline (gray) surfaces.	116
82. Radial sections of baseline and optimized blade geometries.	117

Figure	Page
83. BPF SPL of the second optimized proprotor in hover and forward flight configurations...	118
84. Second and third harmonics SPLs of the second optimized proprotor in forward flight configuration.	118
85. Second and third harmonics SPLs of the second optimized proprotor in hover configuration.	119
86. Skin friction coefficient distribution over Baseline and Optimized surfaces in forward flight configuration.....	120
87. Skin friction coefficient distribution over Baseline and Optimized surfaces in hover configuration.	120
88. Revised parameterization and identification of the radial planar sections of FFD boxes. ..	122
89. (a) Pressure and (b) suction side of optimized (green) and baseline (gray) surfaces.	123
90. Radial sections of baseline and optimized blade geometries obtained from the optimization when power and omega are included.....	124
91. BPF SPL of the third optimized design in hover and forward flight configurations.....	125
92. Second and third harmonics SPLs of the third optimized design in forward flight configuration.	126
93. Second and third harmonics SPLs of the third optimized design in hover configuration. ..	126
94. A sample demonstration of an unsuccessful mesh deformation when an extensive deformation is requested.	130

CHAPTER 1

INTRODUCTION

Development of the engineering design, which provides feasible performance parameters, is essential for manufacturing viable products. In addition, to increase the profitability and performance of the product, the possibility of additional enhancements is constantly being questioned. Those queries demonstrate the need for systematic optimization studies.

If the optimization system consists of only physical assessments, the process may produce numerous prototypes that result from trial-and-error studies. That approach causes huge costs without assuring optimum design. On the other hand, building an optimization system in the computer environment benefits the designer by reducing overall development costs. Moreover, the generated rich data points enable the researcher to deliver an optimum design point before the manufacturing phase. However, it is challenging to develop those computer-based optimization systems.

The first challenging part is developing or using high-fidelity analysis tools to procure performance parameters of the design. The analysis methods should represent real-world physics and be verified. The second part is to combine all those computational engineering tools in the same platform and run them automatically. Another point is the number of iterations to reach the optimized design. The utilized optimization technique plays a vital role in achieving optimization with less computation time. It is possible to succeed in all those challenging parts for a specified engineering problem by developing code schemes. Herein, it is appropriate to define the engineering problem discussed in the dissertation: noise generation and propagation by a rotorcraft utilized for air mobility and its optimization.

Urban Air Mobility (UAM) is one of the most popular proposed solutions for alleviating traffic problems in populated areas. In this context, the proposed types of vehicles mainly consist of rotors or propellers powered by electric motors. Those rotary-wing components can contribute excessively to noise generation. Therefore, a significant noise concern emerges due to urban air vehicles in or around residential areas.

Herein, the aeroacoustic performance of the propeller/rotor needs to be considered rigorously without any deviation in aerodynamic performance. Therefore, evaluation of the flow solution around the rotorcraft has high importance. Computational Fluid Dynamics (CFD) provides comprehensive data for that requirement. Lots of researchers contribute to the development of the numerical method utilized in CFD tools across the world. As of today, CFD tools have high-fidelity features that are very attractive for the engineer for their developments.

For flow analysis, open-source codes have become popular tools in recent years. Those who need them reach the source code freely and add their patch or modifications as they desire. Stanford University Unstructured (SU2) is one of the trending open source-based software released and developed by the contributions of many researchers all around the world. Comprehensive capabilities of SU2 are demonstrated in Ref. [1] for various disciplines. This dissertation aims to extend those capabilities.

In recent years, numerous publications have been realized by the utilization of the SU2. In that research, SU2-based studies involve a broad spectrum of computation types for flow fields. It has a substantial portfolio, including fluid-structure interface, low and high Mach number flow, multiphysics, optimization, sensitivity, turbulent flow, dynamic mesh problems. With regards to optimization, SU2 is a very competitive tool for discrete and continuous adjoint-based optimization.

However, SU2 does not feature an aeroacoustic computation that complies with the sound pressure level calculation induced by flow around rotorcraft. By developing a computational aeroacoustics (CAA) tool within the SU2, it is possible to utilize state-of-the-art features of SU2 software for the developed CAA code. Some of the built-in tools, such as Algorithmic Differentiation (AD), Message Passing Interface (MPI), and python scripts, contribute to developing the CAA tool in parallel with the dissertation objectives. Besides, by embedding the CAA tool in the SU2 suite, aerodynamic sensitivities, aeroacoustic sensitivities, and optimization can be computed in the same platform.

The objectives of the present dissertation are:

1. to develop a CAA analysis tool embedded into the SU2 platform,
2. to verify CFD and CAA codes by comparing their prediction with wind tunnel data and benchmark tools,
3. to expand the multidisciplinary optimization to utilize adjoint-based aeroacoustic and aerodynamic sensitivities,
4. to apply the developed methodology to selected rotorcraft, and
5. to optimize the shape of proprotor blades to improve the overall performance of selected rotorcraft from both aerodynamic and aeroacoustic perspectives.

1.1 Problem Definition

The fast-increasing population and its consequences, such as excessive carbon emissions, traffic jams, and crowded cities, created a necessity for fast and clean transportation. One of the most popular and convenient solutions is UAM. In UAM concepts, Electric vertical take-off and landing (eVTOL) vehicles are one of the most promising options to meet the demands of rapid, practical, cheap, and accessible transportation.

The architecture of the electric air vehicle consists of lots of small propellers instead of one or two large propellers. That configuration is also called “distributed electric propulsion.” As shown in Figure 1, an experimental aircraft, X-57, driven by NASA, is designed to have 14 propellers [2-5]. Since the electric motors deliver maximum shaft power for a large spectrum of the shaft speed, it is allowable to increase the power usage in low RPM levels [2]. Therefore, utilizing the distributed electric propulsion concept enables us to reduce tip speed of the propeller. The reducing tip speed automatically reduces the overall noise level. However, the shape of the blades needs to be changed to supply enough thrust. That situation requires a novel form of propeller providing required aerodynamic performance and minimum noise emission.



Figure 1: NASA's X-57 Maxwell aircraft [5].

An eVTOL vehicle works in various flight conditions. The thrusters need to give sufficient thrust force while the aircraft is taking off, cruising, landing. The transition between those flight configurations can be accomplished with different concepts of solution. For example, tilt-wing concepts (Fig. 2) are designed to bend the wing installed with rotors [6, 7]. Also, as seen in Figure 3, only rotors and their nacelles tilt instead of tilting the wing. In both

concepts, the utilized blades work in both forward flight and hover conditions. Therefore, the developed blade shape should comply with different flow regimes.

NASA delivered a market study for UAM in 2018 [8]. In that document, eVTOL induced noise is indicated as a problem to be regulated by NASA and FAA. Federal agency and university studies establish a regulation involving UAM. By the possible regulative restrictions, noise level propagated from air vehicles needs to be assessed in detail. The definition of the main problem can be described as producing an eVTOL generating sufficient thrust force and noise under the regulative limits for every condition. The presented dissertation addresses the solutions for that problem by developing a tool.

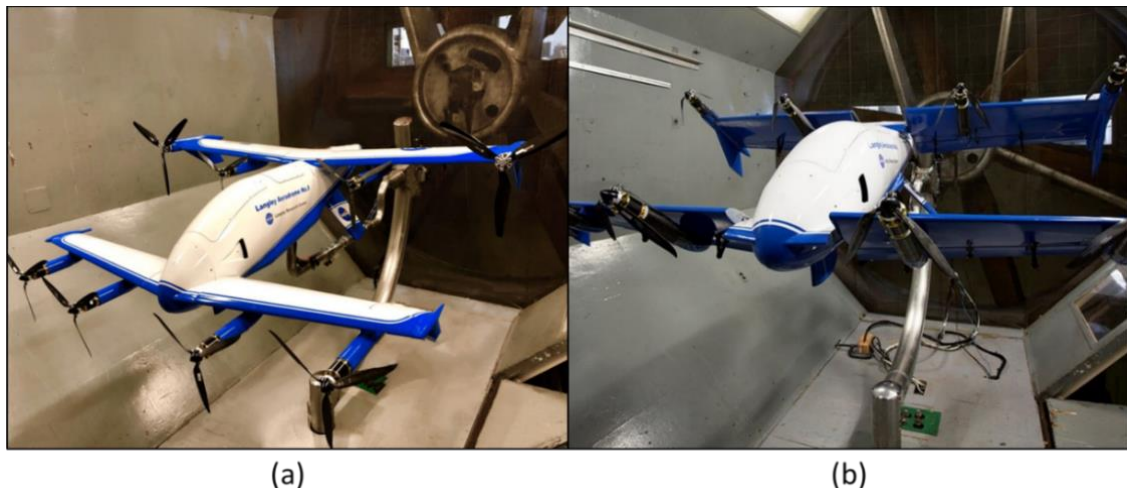


Figure 2: Tilt wing concept, Langley Aerodrome No. 8, (a) forward flight mode and (b) hovering mode [6].

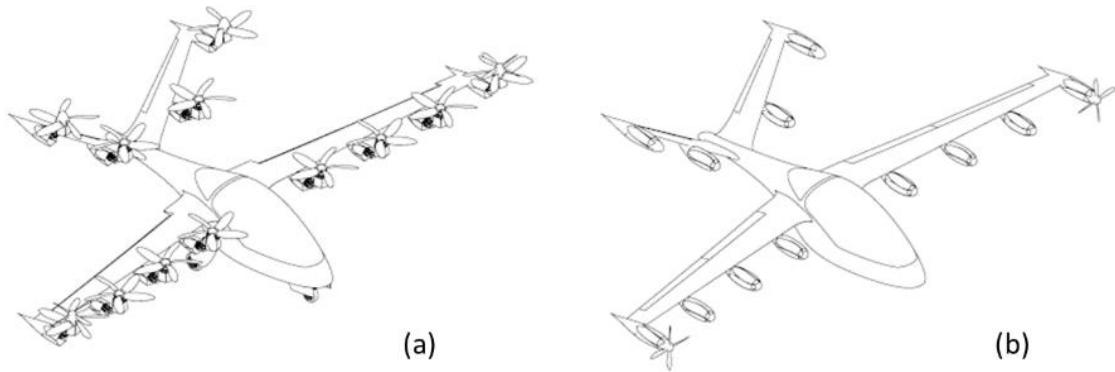


Figure 3: Tilt-rotor concept: (a) VTOL configuration; (b) cruise configuration [9].

1.2 Literature Survey

The literature review is classified according to topics. First, formulations for noise propagation from moving objects are presented. Second, studies for adjoint-based optimizations are cited. Third, the capabilities of the SU2 suite in flowfield analyses and optimization are reviewed.

1.2.1 Acoustic Prediction Methods for Rotorcraft

In the literature, there are a number of numerical approaches to compute noise levels. For example, Lim et al. [10] utilized Linear Euler Equations (LEE) for acoustic prediction for a high-speed propeller, SR-7A. The LEE method extends the CFD solutions to the mid-field. CFD resolves the near-field region, and the LEE method solves mid-field propagation. From the computational cost point of view, it has advantages according to only CFD-based solution techniques. However, using this method for the propagation at the far-field points is not appropriate as shown in Ref [11].

Additionally, the acoustic predictions are performed by utilizing integral methods. Most acoustic research employs these types of methods. The classification can be done by evaluating these methods in two groups: volume integral and surface integral.

Lighthill's analogy [12] propounded the first volume integral approach. The rearranged Navier-Stokes equations constitute Lighthill's equation. Moreover, Curle's modifications [13] extended Lighthill's analogy to include solid boundaries in the equations. However, the acoustic analogy is not in a compact form that makes the equation challenging to compute. Ffowcs Williams and Hawkins [14] proposed a new equation called Ffowcs Williams-Hawkins (FWH), the extended version of acoustic analogy that includes arbitrarily moving surfaces. The equation expresses a quadrupole, turbulent originated, term with volume integral, and monopole and dipole terms with surface integral.

George and Lyrintzis [15] introduced "Kirchhoff Method" terminology into the literature. To evaluate Blade-Vortex Interaction (BVI) originated rotor noise, they expressed an equation consisting of surface integral. The different types of motion and applications have been reviewed by Lyrintzis[11, 16] for the Kirchhoff Method. Farassat and Succi [17] first published the Farassat 1A formulation for propeller noise prediction. Brentner [18] used that formulation by neglecting quadrupole terms and established rotor noise prediction code, WOPWOP. Kuntz [19] performed a study involving comparisons and applications of Kirchhoff, Farassat, and LEE methods for rotor noise predictions. The obtained data were compared with the wind tunnel experiments performed for the UH-1H rotor. According to the results, it was stated that the Kirchhoff method found more accurate results than the Farassat methods. Farassat formulations were not able to predict High-Speed Impulsive (HSI) noise terms. On the other hand, it was found as the most efficient methodology but for low-speed applications. Later, Brentner [20]

presented the far-field quadrupole noise formulation by reducing FWH's volume integral into an integral surface form. The new formulation, Farassat Q1A, was implemented in WOPWOP+ acoustic code that was able to resolve HSI. Farassat and Casper [21] introduced Farassat 2B formulation strictly for broadband noise prediction. The new formulation requires well-resolved turbulence data that is proposedly coupled with LES simulation. Additionally, Najafi-Yazdi et al. [22] demonstrated rearrangement of Farassat 1A formulation for wind tunnel configuration and named it Farassat 1C formulation. Through modification of the radiation vectors in the surface integrals, they obtained the new formulation that is computationally more efficient for non-moving parts in the wind tunnel configuration.

Another critical parameter is the definition of FWH surfaces. It can be defined as permeable (porous) or impermeable (solid) surface approaches. Yin et al. [23] compared results of the acoustic predictions utilizing different types of surface definition for a pusher propeller. It was indicated that permeable surface-based predictions find acoustic pressure slightly higher than impermeable surface-based predictions. Also, they mentioned blade-wake impingement that may cause a large gradient on porous surfaces, hence, incorrect acoustic predictions.

1.2.2 Adjoint-based Optimization

An aircraft design process that includes optimization to minimize noise typically involves many design variables while adhering to aerodynamic performance constraints. The adjoint method enables gradient-based optimization of such problems, where the number of design variables far exceeds the number of design objectives. The computational cost of evaluating the adjoint-based sensitivities is independent of the number of design variables, as shown in Refs. [24-26]. To date, significant progress has already been achieved by adjoint-based aerodynamic shape optimization for both steady and unsteady problems [26-33].

Adjoint-based computation can be classified into two groups, continuous and discrete approaches. The continuous adjoint method employs control theory for shape optimization and the flow equations jointly. Many researchers have applied the continuous approach in their work for the optimization studies in Refs. [24-26, 34-37]. In this approach, the governing equation is linearized to procure adjoint equations, and then it is discretized.

Another method, the discrete approach, obtains the adjoint equations by linearization of previously discretized governing equations. Similarly, another group of researchers pursued that approach for their work related to optimization in fluid dynamics in Refs. [28, 29, 38-44].

Discrete Adjoint (DA) and Continuous Adjoint (CA) have some advantages and disadvantages over each other. Giles and Pierce [45] and Biave et al. [46] compared the DA and CA methods by showing pros and cons. The two methods obtain the adjoint governing equations in different ways, as depicted in Figure 4.

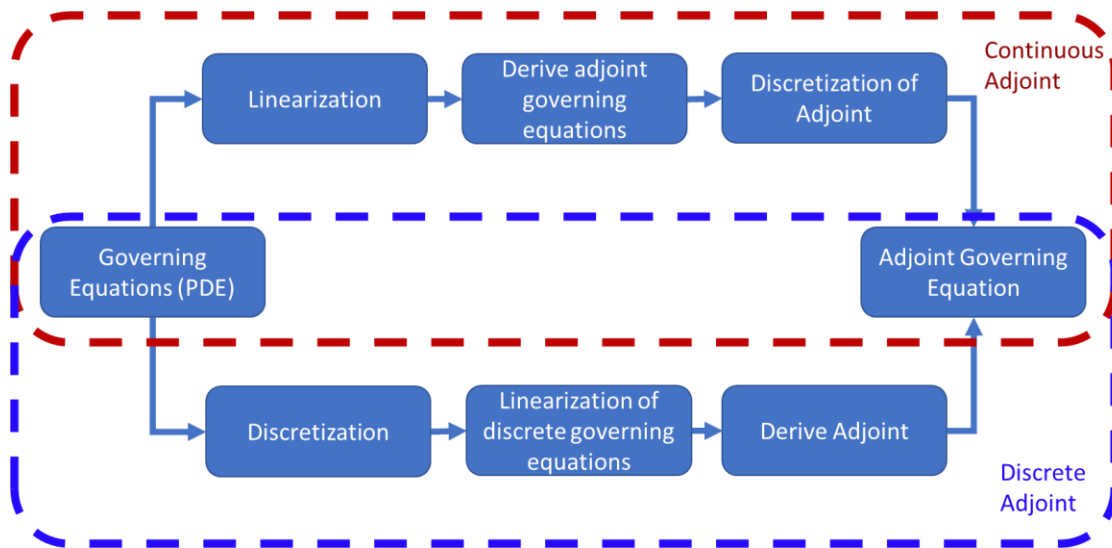


Figure 4: Flowchart of computation of adjoint governing equations by Continuous Adjoint (CA) and Discrete Adjoint (DA) methods.

The differentiation, which is utilized to derive adjoints, can be performed by several methods: hand differentiation, brute force, and algorithmic (a.k.a automatic) differentiation methods. Baysal et al. [47] applied the finite difference method for the optimization studies. Baysal and Ghayour [26] implemented hand differentiation techniques to compute continuous adjoint sensitivities. However, those methods are not efficient to use for DA methods. The complicated structures of the Reynolds-Averaged Navier Stokes (RANS) equations make it difficult to compute the derivative for adjoint computations. The last method, algorithmic differentiation (AD), is the most convenient solution to resolve that problem. AD methods have been utilized to differentiate complete code in Refs. [48, 49] or compute partial derivatives in adjoint computation in Refs. [50-52]. AD method is implemented in many programming languages such as FORTRAN90 and C++ as a differentiation operator. In the present study, both the aerodynamic and aeroacoustic gradients are derived by the adjoint approach, then implemented in the algorithmic differentiation utility, CoDiPack [53].

Wang et al. [43, 54] performed a multidisciplinary adjoint-based optimization for a rotorcraft. Both CFD and comprehensive analysis compose multi-objective functions. Evaluations include both flow and structural analysis. Unsteady case, helicopter rotor, UH-60A, has been investigated in two different flow conditions: forward flight and hover. Therefore, the optimization framework has multipoint optimization features. The desired output from work is to employ the optimized shape in two different flight conditions and improve performance at both conditions. The optimization problem has been defined in detail in the mathematical formulations section, including grid movement, flow, and structural equations. The authors used a Lagrangian formulation to generate sensitivity equations that constitute adjoint-based

optimization. Consequently, both thrust and propulsion coefficients have been improved in two different design points successfully.

Rumpfkeil and Zingg [29] demonstrated a gradient-based optimization for aerodynamic noise reduction of an airfoil geometry. The gradient is determined by the solution of the adjoint equations obtained from a Lagrangian formulation. The authors employed Curle's extension of Lighthill's theory. By utilizing the second-order backward difference method, optimization is conducted with unsteady analyses. The optimized airfoil reduced the noise up to 94 percent, as indicated in that paper.

Enrico Fabiano et al. [55, 56] conducted several studies about aeroacoustic optimization for the rotors. A permeable surface has been utilized to gather acoustic pressure and compute acoustic propagation at the far-field observer points. FWH equations have been employed to calculate noise propagation. As a model, a well-known rotor, HART2, exists in the studies. The rotor was evaluated in the forward flight condition. The objective of the work was to optimize the aeroacoustic performance of the HART2 rotor utilizing adjoint-based shape optimization. Adjoint sensitivities have been verified by using complex differentiation. In optimization cycles, monitoring aerodynamic performance values has been taking account after one full revolution. As indicated in the paper, after 17 design cycles, overall improvement is 3.4 dB by keeping thrust and torque values at the same level.

1.2.3 Capabilities of SU2 in Design Optimization and Aeroacoustics

Palacios et al. [57, 58] demonstrated numerous capabilities of SU2 code for different applications. Economon et al. [30, 59] showed the continuous adjoint methodology and its implementation into the SU2-suite for stationary and moving objects. Albring et al. [60] first

expanded the SU2 capabilities by implementing discrete adjoint methods. Later, Economou et al. [61] revised the SU2 code involving DA and CA methods.

Albring et al. [44] conducted a detailed description of the discrete adjoint solver embedded into SU2 code. Theoretically, the definition of the optimization problem and its linearization place in the paper. The developed code enables solving the adjoint system with the approximate Jacobian approach by utilizing the iterative solver. Besides, to compute gradients, Algorithmic Differentiation (AD) methods are adopted into the solver.

Burghardt et al. [62] expanded the adjoint methods for multizonal configurations. The paper also shows the revised AD flags in the SU2 involving multiphysics environments. The authors presented the results regarding conjugate heat transfer and fluid-structure interaction problems by conducting studies executed only in the SU2 environment.

Zhou et al. [63] demonstrated a discrete adjoint optimization framework involving aerodynamic and aeroacoustic evaluations utilizing the SU2 suite. This paper is the first implementation of the FWH solver into SU2. A simplified version of the Farassat 1A formulation is attempted to be embedded. The acoustic surface is defined as a porous surface located in the flow domain. However, the implementation cannot compute the observer and source time definitions correctly. Additionally, the solver is only valid for non-moving sources and observers. The authors also published a similar framework utilizing frequency-based FWH formulation in Ref. [64]. In another publication [65], they conducted an optimization study to minimize rod-airfoil interaction noise. The presented papers demonstrated that the framework included only flow adjoint, while the grid adjoint was not accounted for.

1.3 Dissertation Layout

Presented in Chapter 2 are the governing equations and numerical schemes that are used in CFD simulations. Chapter 3 provides the details of the employed governing equations for CAA analyses. Chapter 4 contains the framework of optimization, derivation of adjoint components, and methodologies for aeroacoustic objective functions. Chapter 5 explains the implementation of all ideas and equations into the SU2 code. Chapters 6 and 7 present the results for the application of aeroacoustic code and design optimization, respectively. Finally, Chapter 8 concludes the dissertation, provides an overview, conclusions, and some suggestions for future work.

CHAPTER 2

COMPUTATIONAL FLUID DYNAMICS

In fluid mechanics, the physics of fluid flow and its impact on objects are examined. The aerodynamic performance of the vehicle is determined by employing the laws of flow physics. Modeling the fluid flow in a continuum enables resolution of flow problems. That can be done by nonlinear partial differential equations (PDEs).

PDEs govern the fluid flow, and those governing equations are solved by utilizing various numerical methods to predict the aerodynamic performance of the vehicles. CFD consists of combinations of those numerical methods for numerous kinds of flow problems. This chapter is dedicated to discussing the governing equations for compressible and unsteady flow, turbulence modeling, and rotating frame. Lastly, numerical schemes already implemented in SU2 and utilized in the dissertation are discussed in this chapter.

2.1 Governing Equations for Compressible and Unsteady Flow

As given in [30, 58], compressible, time-accurate, and viscous flow are governed by Navier-Stokes equations in SU2. The equations rule conversation for mass, momentum, and energy in the fluid. It is possible to express the conservation equation in arbitrary Lagrangian Eulerian (ALE) [66] differential form as

$$\left\{ \begin{array}{ll} \mathcal{R}(U) = \frac{\partial U}{\partial t} + \nabla \cdot \vec{F}_{ale}^c - \nabla \cdot \vec{F}^v - Q = 0 & in \ \Omega \quad t > 0 \\ \vec{v} = \vec{u}_\Omega & on \ S \\ \partial_n T = 0 & on \ S \\ (W)_+ = W_\infty & on \ \Gamma_\infty \end{array} \right. \quad (2.1)$$

where S and Γ_∞ represent surface boundary and far-field boundary of the flow domain, Ω , respectively. $\mathcal{R}(U) = 0$ is the residual function of conservative variables as given by

$$U = \begin{Bmatrix} \rho \\ \rho \vec{v} \\ \rho E \end{Bmatrix}, \quad (2.2)$$

and \vec{F}_{ale}^c , \vec{F}^v , and Q are convective fluxes, viscous fluxes, and generic source term respectively, and they are given as

$$\begin{aligned} \vec{F}_{ale}^c &= \begin{Bmatrix} \rho(\vec{v} - \vec{u}_\Omega) \\ \rho \vec{v} \otimes (\vec{v} - \vec{u}_\Omega) + \bar{I}p \\ \rho E(\vec{v} - \vec{u}_\Omega) + p\vec{v} \end{Bmatrix}, \quad \vec{F}^v = \begin{Bmatrix} 0 \\ \bar{\tau} \\ \bar{\tau} \cdot \vec{v} + \mu_{tot}^*(c_p \nabla T) \end{Bmatrix}, \\ Q &= \begin{Bmatrix} q_p \\ \vec{q}_{\rho \vec{v}} \\ \vec{q}_{\rho E} \end{Bmatrix}, \end{aligned} \quad (2.3)$$

Here ρ is the fluid density, \vec{v} is the 3-dimensional vector for flow speed, \vec{u}_Ω is the velocity of a moving domain, E is the total energy, p is the static pressure, \bar{I} is the tensor for Kronecker delta, T is the temperature and c_p is the specific heat at constant pressure. Additionally, $\bar{\tau}$ is the viscous stress tensor that can be defined as

$$\bar{\tau} = \mu_{tot} \left(\nabla \vec{v} + \nabla \vec{v}^T - \frac{2}{3} \bar{I}(\nabla \cdot \vec{v}) \right), \quad (2.4)$$

where μ_{tot} indicates total viscosity driven by

$$\mu_{tot} = \mu_{dyn} + \mu_{tur}, \quad \mu_{tot}^* = \frac{\mu_{dyn}}{Pr_d} + \frac{\mu_{tur}}{Pr_t}. \quad (2.5)$$

In these formulas, μ_{dyn} and μ_{tur} represent dynamic viscosity and turbulent viscosity, respectively. μ_{tot}^* is the effective thermal conductivity that includes the dynamic and turbulent Prandtl numbers shown as Pr_d and Pr_t , consequently. The dynamic viscosity, μ_{dyn} , is calculated by Sutherland's law [67]. Lastly, turbulent viscosity, μ_{tur} , is computed utilizing turbulence modeling.

By the assumption of an ideal gas, temperature, T , is obtained by

$$T = \frac{p}{R\rho}, \quad (2.6)$$

where the gas constant, R , is equal to

$$R = \frac{c_p(\gamma - 1)}{\gamma R}, \quad (2.7)$$

γ is a gas constant and taken as 1.4 in the dissertation.

The unsteady Reynolds-averaged Navier-Stokes (URANS) equations need to be compounded with turbulence modeling and boundary conditions to solve the flow problem. Modeling for the turbulence-related terms is to be discussed in the following section. Regarding the boundary conditions, the isothermal no-slip boundary condition is utilized for the surfaces. As previously mentioned, moving surfaces, such as the propeller and rotor, are the main subject of this dissertation. Those parts move together with the domain surrounding surfaces. Boundary conditions for those parts include movement velocity, \vec{u}_Ω . Lastly, the far-field boundary condition is utilized for the external boundaries. In SU2, the turbulence can be modeled by Spalart-Allmaras and the Menter shear stress transport when the URANS solver is used. In the present dissertation, the one-equation Spalart Allmaras [68] turbulence model, a more cost-effective option, is used to compute turbulent viscosity. Details of the turbulence model can be found in the appendix.

2.2 Rotating Reference Frame

To use transport equations for problems dealing with rotating flow domain, the so-called rotating reference frame, previously defined governing equations need to be posed with formulas. That enables the governing equations to solve the flow around the rotating body such as turbomachinery, propeller, and rotor.

To attain the required equation for the rotating reference frame, we need to define the velocity of the domain and the required source term representing the motion of rotation in SU2 [58]. In equation (2.1), source term, Q and domain velocity, \vec{u}_Ω , become

$$Q = \begin{Bmatrix} 0 \\ -\rho(\vec{\omega} \times \vec{r}) \\ 0 \end{Bmatrix}, \quad \vec{u}_\Omega = \vec{\omega} \times \vec{r}, \quad (2.8)$$

where $\vec{\omega}$ and \vec{r} are the three-dimensional angular velocity and the position vectors, respectively.

2.3 Numerical Schemes

The software SU2 solves the Unsteady Reynolds-averaged Navier-Stokes (URANS) equations to analyze compressible, turbulent flows commonly found in aerospace engineering problems. Throughout the simulations, in-house developed code based on SU2-v7.1.1 is utilized. The governing equations are spatially discretized using a finite volume method on unstructured meshes. The time marching of the semi-discretized URANS equations is performed by a dual time-stepping method. The Spalart-Allmaras (SA) turbulence model [68] is employed.

For the multizonal simulation, the interface, called sliding mesh, transmits the conserved variables of the flow from one zone to the other by conservative interpolation methods. For the discretization of the flow equation, the Jameson-Schmidt-Turkel (JST) [69] scheme is utilized with 0.5 and 0.02 second and fourth-order dissipation, respectively, without any limiter. These configurations are based on the best practices reported in Ref. [31]. The Green-Gauss method is employed for the spatial gradients. The resulting linear systems are solved using the Flexible Generalized Minimum Residual (FGMRES) method and the Krylov preconditioner [70] with an error tolerance of 1E-6.

CHAPTER 3

COMPUTATIONAL AEROACOUSTICS

In this chapter, governing equations for the aeroacoustic computation are presented. The well-known acoustic formulation, FWH, and its derivation, Farassat-1A formulation, are demonstrated in this section.

3.1 Ffowcs Williams and Hawking Equation

The FWH equation (Eq. (3.1)) is an alternative form of conservation laws [14]. It includes monopole, dipole, and quadrupole terms with each corresponding to a different source of aerodynamic noise:

$$\square^2 p' = \frac{\partial}{\partial t} [\rho_0 v_n \delta(f)] - \frac{\partial}{\partial x_i} [p n_i \delta(f)] + \frac{\partial^2}{\partial x_i \partial x_j} [H(f) T_{ij}], \quad (3.1)$$

where p' is acoustic pressure, \square^2 is the D'Alembertian operator and $f(x, t) = 0$ represents a moving control surface where n_i is the unit outward normal. $H(f)$ and $\delta(f)$ are the Heaviside and Dirac delta functions, respectively. Lastly, ρ_0 , v_n , p , and T_{ij} are defined as freestream density, surface velocity dotted with the surface normal vector, the static pressure, and Lighthill stress tensor, respectively.

3.2 Farassat 1A Formulation

Farassat derived a family of more practical formulations [71] of the FWH equation. In the F1A formulation, the quadrupole term is neglected, and pressure fluctuation is equal to the sum of thickness noise and loading noise [72],

$$p'(\mathbf{x}, t) = p'_T(\mathbf{x}, t) + p'_L(\mathbf{x}, t), \quad (3.2)$$

where p'_T and p'_L terms are the contributions of the thickness noise and the loading noise, respectively. These terms consist of integral equations as shown in Eqs. (3.3) and (3.4):

$$p'_T(\mathbf{x}, t) = \frac{1}{4\pi} \int_S \left[\frac{\rho_0 (\dot{U}_i n_i + U_i \dot{n}_i)}{r(1 - M_r)^2} \right]_{ret} dS + \frac{1}{4\pi} \int_S \left[\frac{\rho_0 U_i n_i K}{r^2(1 - M_r)^3} \right]_{ret} dS, \quad (3.3)$$

$$p'_L(\mathbf{x}, t) = \frac{1}{4\pi} \frac{1}{c} \int_S \left[\frac{\dot{F}_i \hat{r}_i}{r(1 - M_r)^2} \right]_{ret} dS + \frac{1}{4\pi} \int_S \left[\frac{F_i \hat{r}_i - F_i M_i}{r^2(1 - M_r)^2} \right]_{ret} dS \\ + \frac{1}{4\pi} \frac{1}{c} \int_S \left[\frac{F_i \hat{r}_i K}{r^2(1 - M_r)^3} \right]_{ret} dS, \quad (3.4)$$

where, for an impermeable surface,

$$U_i = v_i \quad (3.5)$$

$$F_i = L_{ij} n_j \quad (3.6)$$

$$L_{ij} = P'_{ij} = (p - p_\infty) \delta_{ij} \quad (3.7)$$

$$K = \dot{M}_i \hat{r}_i r + M_r c - M^2 c \quad (3.8)$$

$$M_r = \frac{v_i}{c} \hat{r}_i. \quad (3.9)$$

Here, r is the radiation vector or distance between observer and source points. Similarly, \hat{r}_i represents the unit radiation vector. \dot{M}_i is the time derivative of local Mach number, M , depending on the speed of sound, c , and local velocity, v_i . In addition, dS , δ_{ij} and p_∞ are the local panel area, the Kronecker delta and the freestream pressure, respectively.

In the present development, the author follows the impermeable surface approach again with the time domain implementation as shown in Eqs. (3.5)-(3.7).

Computations represent a wind tunnel configuration; that is, a stationary observer is placed in a moving medium. This is equivalent to a moving-observer situation with the observer moving at negative freestream velocity, $-\vec{U}_0$, in a stationary medium.

CHAPTER 4

OPTIMIZATION

This chapter is included to provide the content of the optimization setup. Derivations of the equations used for adjoint-based aeroacoustic optimization and utilization in the optimization framework are discussed in this chapter. In addition, definitions of aeroacoustic functions address the objective function of optimization.

4.1 Optimization Framework

Before summarizing the steps of each of the modules, the overall methodology is presented graphically as a flowchart (Fig. Figure 5). First, the aerodynamic and aeroacoustic analyses determine the values of the objective (or cost) function and the constraints on the baseline grid by using shape design variables, α . The optimizer, Scipy-SLSQP [73], a gradient-based optimization tool, requires gradients for the projection. However, if existing gradients are sufficient to proceed with the line searching, the optimizer does not need the gradients. The next step is the checkpoint to evaluate that condition. If gradients are required, the process solves the adjoint equations. Afterward, the tools acquire the derivatives of the objective function and the constraints with respect to the conserved variables. The system utilizes the derivatives and computes sensitivities with respect to the design variable.

After, the optimization cycle continues with the evaluation step that involves the objective function, the constraints, the side constraints, the gradients, and the design vector. Then, another checkpoint controls the condition of convergence by computing the residual of the objective function. If the error is lower than the threshold value, the optimizer computes the new design variable vector, α^{new} . Otherwise, the optimization cycle ends. Next, the system sends the new variable vector to the section performing mesh deformation for surface and volume grids.

Finally, the updated grid is utilized for the computations at the following design steps, and the loop repeats.

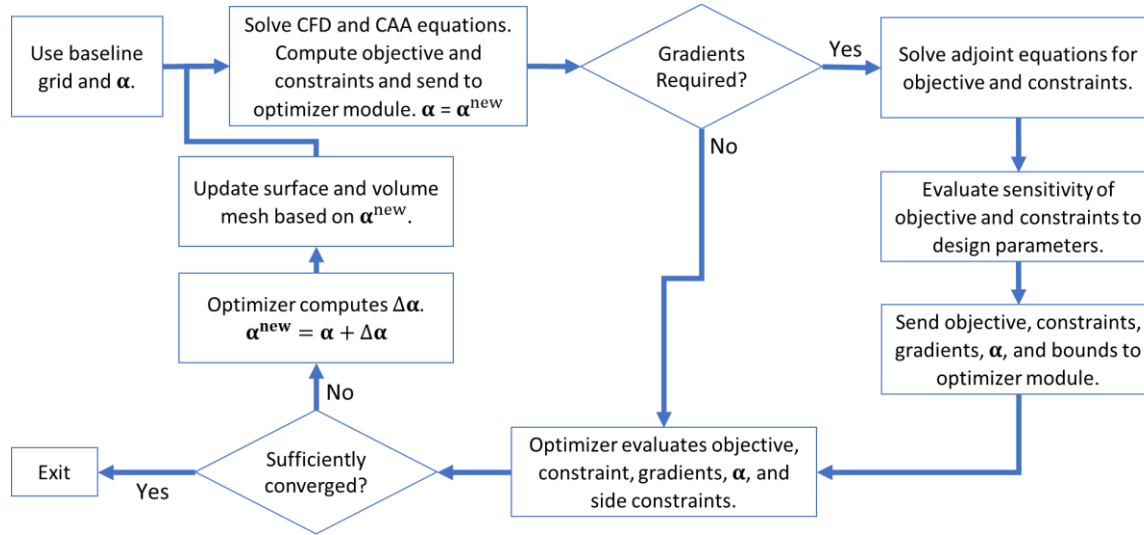


Figure 5: The gradient-based optimization cycle.

4.2 Sensitivities of Gradient-Based Optimization

A powerful feature of SU2 is the availability of algorithmic-differentiation (AD) rendered sensitivities by the tool CoDiPack [53]. By successive applications of the chain-rule differentiation through the SU2 code, both the flow analysis output and its derivative with respect to prescribed design variables are computed simultaneously. A remarkable feature of AD, owing to its construction, is that it does not incur any truncation errors, rendering derivatives that are at machine accuracy.

At the start, an optimization problem is defined. The objective function, J , is chosen as the sound pressure level, which is a function of the state variable vector, \mathbf{U} , and the grid coordinates, \mathbf{X} , which are in turn functions of the vector, α , of design variables. The discretized

residual of the flow and acoustic equations, R , is introduced as a constraint function, which also is in turn a function of vectors, \mathbf{U} and \mathbf{X} :

$$\underset{\alpha}{\text{minimize}} \quad J(U(\alpha), X(\alpha)), \quad (4.1)$$

$$\text{subject to} \quad R(U(\alpha), X(\alpha)) = 0. \quad (4.2)$$

Next, this definition needs to be extended to be utilized for a problem with moving surfaces. It must comply with the unsteady simulations, grid motions, and CFD-CAA coupling. Previously, Zhou et al. [63, 64] applied the adjoint-based discrete optimization for stationary surfaces, where they utilized dual time stepping. Albring et al. [44] showed how to implement the grid motion into the optimization problem. By compounding these two steps and extending for the problem at hand, a new optimization problem definition is introduced as follows:

$$\underset{\alpha}{\text{minimize}} \quad J(U^n, X^n, \alpha), \quad (4.3)$$

$$\text{subject to} \quad U^n = G^n(U^n, U^{n-1}, U^{n-2}, X^n, X^{n-1}, X^{n-2}, \alpha), \quad (4.4)$$

$$X^n = M^n(\alpha) \quad n = 1, \dots, N, \quad (4.5)$$

where M^n denotes the mesh deformation equation and G^n is an iteration of pseudo time stepping. The symbol n represents the time iteration index and the objective function, J , is evaluated for all n up to N . Next, the problem is recast as a Lagrangian (or penalty) function as follows:

$$\begin{aligned} L(\alpha, U^n, X^n, \bar{U}^n, \bar{X}^n) \\ = J(U^n, X^n, \alpha) + \sum_{n=1}^N [(G^n(U^n, U^{n-1}, U^{n-2}, \alpha) - U^n)^T \bar{U}^n] \\ + \sum_{n=1}^N [(M^n(\alpha) - X^n)^T \bar{X}^n]. \end{aligned} \quad (4.6)$$

By differentiating the Lagrangian function with respect to α , \bar{U}^n , and \bar{X}^n , the first-order optimality conditions are obtained:

$$\frac{dL}{dU^n} = 0 = \frac{\partial J}{\partial U^n} - \bar{U}^n + \frac{\partial G^n}{\partial U^n} \bar{U}^n + \frac{\partial G^{n-1}}{\partial U^n} \bar{U}^{n-1} + \frac{\partial G^{n-2}}{\partial U^n} \bar{U}^{n-2}, \quad (4.7)$$

$$\frac{dL}{dX^n} = 0 = \frac{\partial J}{\partial X^n} + \frac{\partial G^n}{\partial X^n} \bar{U}^n + \frac{\partial G^{n-1}}{\partial X^n} \bar{U}^{n-1} + \frac{\partial G^{n-2}}{\partial X^n} \bar{U}^{n-2} - \bar{X}^n, \quad (4.8)$$

$$\frac{dL}{d\alpha} = \frac{\partial J}{\partial \alpha} + \sum_{n=1}^N \left[\left(\frac{\partial G^n}{\partial \alpha} \right)^T \bar{U}^n \right] + \sum_{n=1}^N \left[\left(\frac{\partial M^n}{\partial \alpha} \right)^T \bar{X}^n \right]. \quad (4.9)$$

After rearranging Eqs. (4.7) and (4.8), the adjoints of the CFD and the grid equations become,

$$\bar{U}^n = \frac{\partial J}{\partial U^n} + \frac{\partial G^n}{\partial U^n} \bar{U}^n + \frac{\partial G^{n-1}}{\partial U^n} \bar{U}^{n-1} + \frac{\partial G^{n-2}}{\partial U^n} \bar{U}^{n-2}, \quad (4.10)$$

$$\bar{X}^n = \frac{\partial J}{\partial X^n} + \frac{\partial G^n}{\partial X^n} \bar{U}^n + \frac{\partial G^{n-1}}{\partial X^n} \bar{U}^{n-1} + \frac{\partial G^{n-2}}{\partial X^n} \bar{U}^{n-2}, \quad (4.11)$$

and the general form of the sensitivity derivatives of the objective function Eq. (4.9) becomes,

$$\frac{dJ}{d\alpha} = \frac{1}{N} \sum_{n=1}^N \left[[\bar{U}^n]^T \left[\frac{\partial G^n}{\partial \alpha} \right] \right] + \frac{1}{N} \sum_{n=1}^N \left[[\bar{X}^n]^T \left[\frac{\partial M^n}{\partial \alpha} \right] \right]. \quad (4.12)$$

These equations are solved as presented in the flowchart below (Figure 6). Briefly, the CFD solver outputs the state variables that are fed into the CAA solver and the adjoint computations. Subsequently, the CAA solver obtains the fluctuating component of pressure, p' , and the objective function, J , and its derivatives with respect to the grid and the state variables for the surfaces. Next, the adjoint CFD solver computes the flow adjoints used as input to compute mesh adjoints. Finally, the algorithmic differentiator calculates the sensitivities with respect to the design variable vector, α .

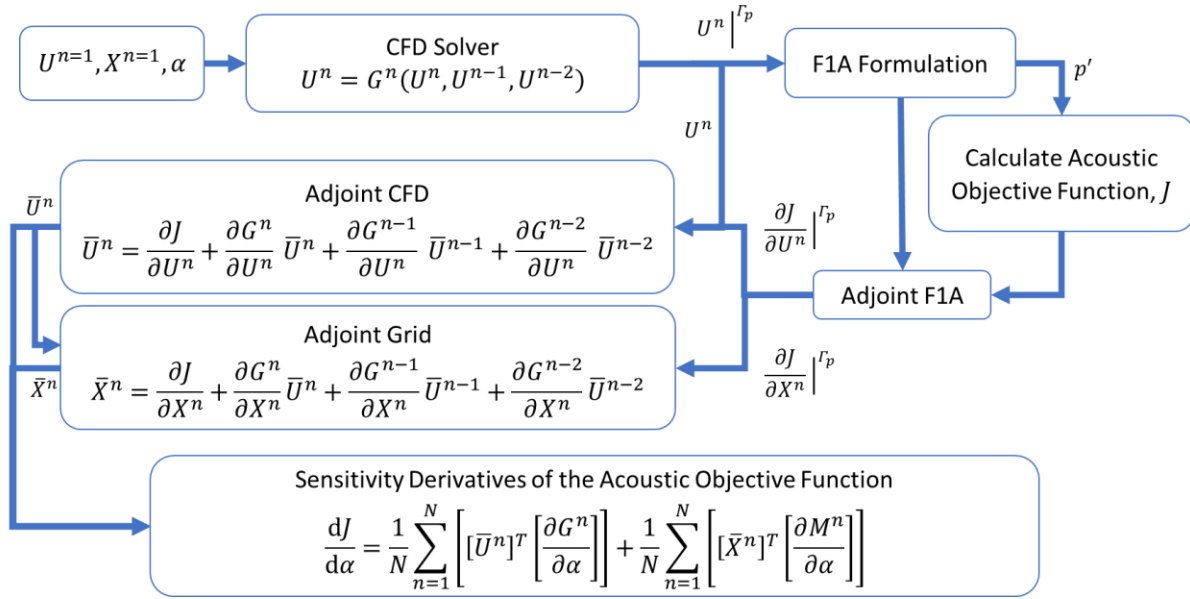


Figure 6: Flowchart of adjoint sensitivities for coupled aerodynamics and aeroacoustics.

The described flowchart can solve optimization problems depending on both flow and geometric variables. In the content of the dissertation, one more approach is utilized for optimization studies. If there is no flow variable, such as angle of attack, rotation rate, freestream Mach number, etc., the formulation mentioned above can be simplified for a simpler computation. By this approach, the flow equation, G , does not depend on α . Therefore, the Lagrangian equation (4.6) reformed as

$$\begin{aligned}
 L(\alpha, U^n, X^n, \bar{U}^n, \bar{X}^n) &= J(U^n, X^n, \alpha) + \sum_{n=1}^N [(G^n(U^n, U^{n-1}, U^{n-2}) - U^n)^T \bar{U}^n] \\
 &+ \sum_{n=1}^N [(M^n(\alpha) - X^n)^T \bar{X}^n].
 \end{aligned} \tag{4.13}$$

Based on this equation, the content of the flow chart changes accordingly, as seen in Figure 7. Similarly, outputs from the CFD solver and F1A formulation enter into adjoint CFD

and grid solver, but flow adjoints, \bar{U}^n , are utilized in only the computation for the adjoint grid. At the last bullet, the system computes sensitivities by using grid adjoints and mesh sensitivities

$$\frac{d}{d\alpha} M^T(\alpha).$$

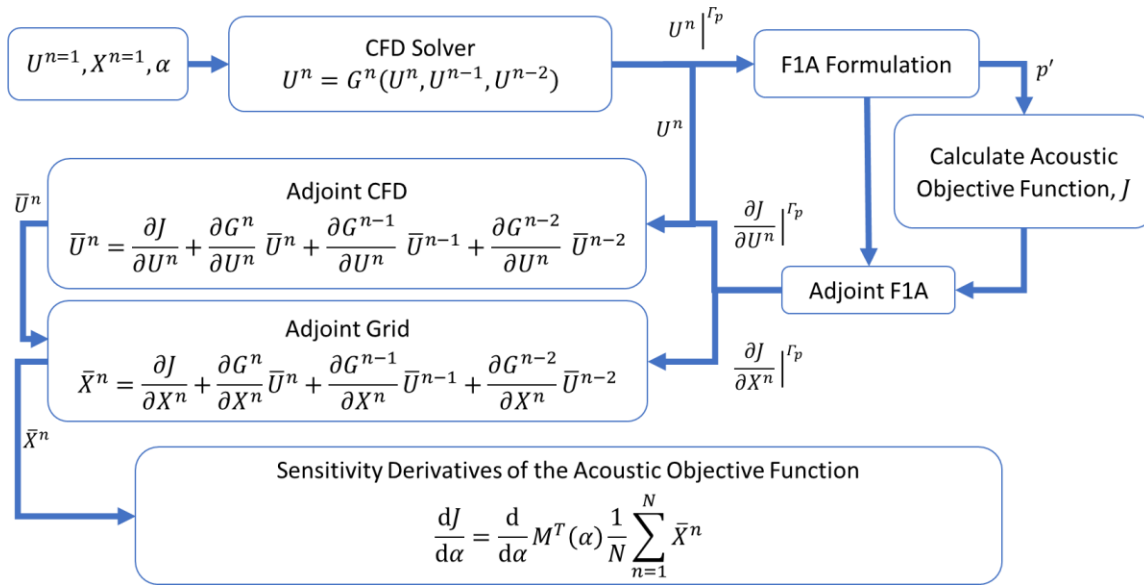


Figure 7: Flowchart of adjoint sensitivities for coupled aerodynamics and aeroacoustics, including only shape variables.

4.3 Objective Functions

When defining the optimization problem, a critical point is how to compute the objective function. Since the work involves multiple observer points and multiple flow regimes, the objective function needs to include all those aspects. Herein, three methodologies are described to represent the objective function.

4.3.1 Method-1

The first method is a more trivial way to create the objective function. Pressure fluctuation, p' , is used as an input that provides root-mean-square calculations as follows:

$$p_{rms} = \sqrt{\frac{\sum_{n=1}^N p'^2}{N}}, \quad (4.14)$$

where N is the sample size of time domain-based acoustic pressure history. This single number can be used to declare noise output only for one observer. To include all observer points, another simple averaging process is presented:

$$p_{rms}^{Total} = \frac{1}{NO} \sum_{i=1}^{NO} p_{rms}^i, \quad (4.15)$$

Here i is the individual observer points and p_{rms}^i represents a root-mean-square value corresponding to a particular observer point. For the total number of microphone points, NO , we define the objective function as p_{rms}^{Total} . Considering for multipoint optimization, two different acoustic computations are held in the optimization cycle. The results obtained from the calculation need to be combined. A simple summation does that combination. For example, if we look at the forward flight condition, objective function, F_{FF} , equals p_{rms}^{Total} . The same equilibrium is applied for the function of hover, F_H . Finally, the objective function is given by

$$F = F_{FF} + F_H. \quad (4.16)$$

4.3.2 Method-2

As anticipated, indicating the noise level by p_{rms} may not be practical. In industry, academia, or the public, the noise level unit is decibel [dB] for common usage. Therefore, the

values of the output which are p_{rms} are converted into sound pressure level (SPL) that is in dB units. A logarithmic function quite simply performs the conversion as given below.

$$SPL = 10 \log_{10} \left(\frac{p_{rms}^2}{p_{ref}^2} \right), \quad (4.17)$$

where p_{ref} represents reference sound pressure level obtained for human ear noise perceptions [74]. In the dissertation, that value is set at 2×10^{-5} Pascals for all aeroacoustic computation. Again, the resulting objective function is driven from SPL values for the multiple observers and multiple flight regimes as similar as the formulation depicted in equations (4.15) and (4.16).

Applying those formulations for the objective function can seem trivial and easy to implement. However, the main drawback of using those formulations is that they are not sensitive to the position of the observers and noise propagation at particular frequencies, such as tonal frequencies and harmonics, sufficiently. Therefore, method-3 may be more convenient to respond to that requirement.

4.3.3 Method-3

The defined methods above do not present discrete values based on the specific frequency. For example, noise generated from a rotor consists of tonal noise or harmonic noise and broadband noise [75]. Also, the obtained pressure fluctuation history may include some numerical artifacts. For those reasons, filtering the acoustic signal becomes a necessity.

The code performs shifting from the time domain to the frequency domain Fourier transform tool in the current implementation. It computes Discrete Fourier Transform (DFT). The details of the implementation will be discussed in Chapter 5. Herein, we will discuss obtaining an objective function based on the sound pressure level corresponding to the blade-passing frequency (BPF). First, the definition of the BPF is given by,

$$BPF = \frac{RPM \times (Number\ of\ blades)}{60}. \quad (4.18)$$

Sound power deals with acoustic intensity over an area defined by spherical coordinates.

$$W = \int I dA = \int \frac{p_{rms}}{\rho c} dA = \int_0^{2\pi} \int_0^{\pi} \frac{p_{rms}}{\rho c} r^2 \sin \theta d\theta d\varphi, \quad (4.19)$$

where W and I represent acoustic power and intensity, respectively. The rotor geometry has a symmetric shape around the rotation axis that provides constant φ angles.

$$W = 2\pi \int_0^{\pi} \frac{p_{rms}^2}{\rho c} r^2 \sin \theta d\theta. \quad (4.20)$$

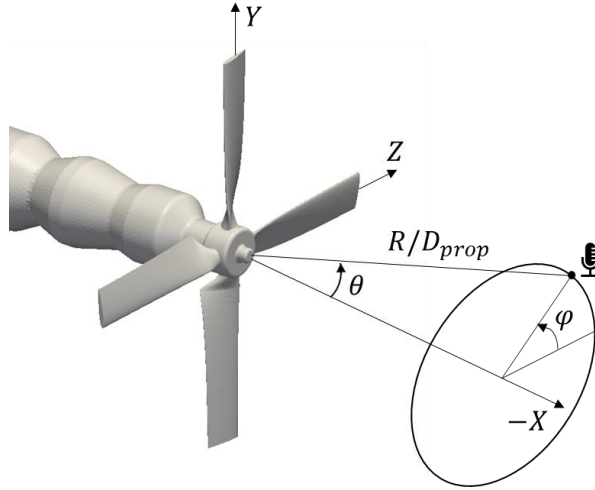


Figure 8: Sample demonstration of the coordinate system of microphone position.

Additionally, in this dissertation, microphone position is distributed at the constant distance in y and z direction. Thus, we introduce a new variable h as

$$h = \sqrt{y^2 + z^2} \text{ and } h = r \sin \theta. \quad (4.21)$$

Then, equation (4.20) becomes

$$W = 2\pi \int_0^\pi \frac{p_{rms}^2}{\rho c} \frac{h^2}{\sin \theta} d\theta = \frac{2\pi h^2}{\rho c} \int_0^\pi \frac{p_{rms}^2}{\sin \theta} d\theta. \quad (4.22)$$

If the scanning in θ angles contains problem-related inputs, the bounds of the integral restricted with θ_l and θ_h which are the lowest and highest angles correspondingly. Thus, equation (4.22) becomes

$$W = \frac{2\pi h^2}{\rho c} \int_{\theta_l}^{\theta_h} \frac{p_{rms}^2}{\sin \theta} d\theta. \quad (4.23)$$

Utilizing DFT, the time history data turns into frequency domain as

$$p(f) = DFT(p(t)). \quad (4.24)$$

The obtained frequency-based data is used for the root-mean-square computation for frequency-based RMS. Additionally, we introduce a new weighting function as in Ref. [76]. Thus, the A-weighted function is found by using an A-weighting function, W_A as follows.

$$p_{f,rms,A}^2 = p_{f,rms}^2 \cdot W_A. \quad (4.25)$$

Function evaluation for W_A is the same as in Ref. [74]. Then, we calculate overall sound pressure level over each frequency as

$$p_{rms,A}^2 = \sum_{f_{min}}^{f_{max}} p_{f,rms,A}^2. \quad (4.26)$$

Finally, if we combine equations (4.17), (4.23), and (4.26) into one equation, we find

$$F = 10 \log_{10} \left(\frac{2\pi h^2}{\rho c} \int_{\theta_l}^{\theta_h} \frac{p_{rms,A}^2}{\sin \theta} d\theta \right) - 10 \log_{10} \left(\frac{p_{ref}^2}{\rho c} \right). \quad (4.27)$$

Here the F is the objective function for a generic application. Also, we need to include hover and forward flight conditions in the objective function. That description is shown with FF and H

abbreviation representing forward flight and hover conditions. Thus, the objective function becomes

$$F = F_{FF} + F_H, \quad (4.28)$$

and

$$F = 10 \log_{10} \left(\int_{\theta_{l,FF}}^{\theta_{h,FF}} \frac{p_{rms,A,FF}^2}{\sin \theta} d\theta \right) + 10 \log_{10} \left(\int_{\theta_{l,H}}^{\theta_{h,H}} \frac{p_{rms,A,H}^2}{\sin \theta} d\theta \right) - 20 \log_{10} \left(\frac{p_{ref}^2}{2\pi h^2} \right). \quad (4.29)$$

The obtained equation includes multiple flight regimes and observers. Although it seems more complicated than Method-1 and Method-2, it provides quite a good alignment with overall acoustic power.

CHAPTER 5

NUMERICAL IMPLEMENTATIONS

This chapter discusses the numerical implementation of the mathematical model and its required submodules inside the code. Herein, the required numerical operations are classified into three groups: F1A implementation, sensitivities, and SU2 integration.

5.1 F1A Implementation

5.1.1 Discretization

For the numerical implementation, Farassat 1A equations (3.3) and (3.4) need to be written in a discretized form. There are a couple of assumptions that we need to mention. The first is about the area of the panel used in the formulation. The surface moving through time-accurate simulation does not change its shape. Presumably, a rigid body has a constant surface area throughout the simulation. That makes finite areas, dS , constant. Also, the formulation can be shown in simplified form with four essential terms, T_1 , T_2 , T_3 , and T_4 . By those adjustments, the formulation becomes

$$p'(\mathbf{x}, t) = \frac{\Delta S}{4\pi} [T_1 + T_2 + T_3 + T_4]. \quad (5.1)$$

Also, we introduce four more coefficients for a segmented formulation as follows.

$$A_0 = \frac{\rho_0}{r(1 - M_r)^2}, \quad (5.2)$$

$$B_0 = \frac{\rho_0}{r^2(1 - M_r)^3}, \quad (5.3)$$

$$C_0 = \frac{1}{cr^2(1 - M_r)^2}, \quad (5.4)$$

and

$$D_0 = \frac{1}{cr^2(1 - M_r)^3} . \quad (5.5)$$

By using A_0 term in the equation (3.3), T_1 term becomes

$$\begin{aligned} T_1 &= \frac{\rho_0(\dot{U}_i n_i + U_i \dot{n}_i)}{r(1 - M_r)^2} = A_0 \sum_{i=0}^{nDim} \dot{U}_i n_i + U_i \dot{n}_i \\ &= A_0 \sum_{i=0}^{nDim} \frac{U_i^{t+1} - U_i^{t-1}}{2\Delta t} n_i^t + U_i^t \frac{n_i^{t+1} - n_i^{t-1}}{2\Delta t} , \end{aligned} \quad (5.6)$$

where the time derivative of the velocity is found by central difference formulation as the same as normal derivatives. Here, we can introduce a new coefficient, A_1 . Then the T_1 term becomes

$$T_1 = A_0 A_1 . \quad (5.7)$$

Similarly, T_2 term can be shown as a series function as given by

$$T_2 = \frac{\rho_0 U_i n_i K}{r^2(1 - M_r)^3} = B_0 K \sum_{i=0}^{nDim} U_i^t n_i^t . \quad (5.8)$$

Again, we introduce a new coefficient, B_1 , and equation (5.8) becomes

$$T_2 = B_0 K B_1 . \quad (5.9)$$

If we apply the same strategy for T_3 and T_4 , we find the following equations.

$$T_3 = \frac{\dot{F}_i \hat{r}_i r + F_i \hat{r}_i - F_i M_i}{cr^2(1 - M_r)^2} = C_0 \left[\sum_{i=0}^{nDim} \dot{F}_i \hat{r}_i r + \sum_{i=0}^{nDim} F_i \hat{r}_i - \sum_{i=0}^{nDim} F_i M_i \right] , \quad (5.10)$$

$$\begin{aligned}
T_3 = C_0 & \left[\sum_{i=0}^{nDim} \left[\sum_{j=0}^{nDim} \frac{P_{ij}^{t+1} n_j^{t+1} \delta_{ij} - P_{ij}^{t-1} n_j^{t-1} \delta_{ij}}{2\Delta t} \right] \hat{r}_i^t r^t \right. \\
& \left. + \sum_{i=0}^{nDim} \left[\sum_{j=0}^{nDim} P_{ij}^t n_j^t \delta_{ij} \right] \hat{r}_i^t - \sum_{i=0}^{nDim} \left[\sum_{j=0}^{nDim} P_{ij}^t n_j^t \delta_{ij} \right] M_i^t \right],
\end{aligned} \tag{5.11}$$

and

$$T_4 = \frac{F_i \hat{r}_i K}{cr^2(1 - M_r)^3} = D_0 K \sum_{i=1}^{nDim} \left[\sum_{j=0}^{nDim} P_{ij}^t n_j^t \delta_{ij} \right] \hat{r}_i^t. \tag{5.12}$$

For T_3 and T_4 terms, by introducing C_1 and D_1 , we obtain the equation as follows.

$$T_3 = C_0 C_1, \tag{5.13}$$

and

$$T_4 = D_0 K D_1. \tag{5.14}$$

Thus, the equation (5.1) also equals to

$$p'(\mathbf{x}, t) = \frac{\Delta S}{4\pi} [A_0 A_1 + B_0 K B_1 + C_0 C_1 + D_0 K D_1], \tag{5.15}$$

where the coefficient K is given by

$$K = \sum_{i=0}^{nDim} \frac{U_i^{t+1} - U_i^{t-1}}{2\Delta t c} \hat{r}_i^t r^t + M_r c + M^2 c. \tag{5.16}$$

Also, some of the terms need to be computed to make the equation a closure problem. Therefore,

here M_r , \hat{r}_i , r , and M terms are respectively given by

$$M_r = \sum_{i=0}^{nDim} \frac{U_i^t \hat{r}_i^t}{c}, \tag{5.17}$$

$$\hat{r}_i = \frac{r_i}{r}, \quad r = \sqrt{\sum_{i=0}^{nDim} r_i^2}, \quad (5.18)$$

and

$$M = \sqrt{\sum_{i=0}^{nDim} \left(\frac{U_i^t}{c} \right)^2}. \quad (5.19)$$

Overall, utilizing those equations, acoustic propagation is possible to be computed. However, some terms need specific calculations. Those particular terms are radiation vector, observer time, source time, normal vectors, and velocity vectors. The following sections discuss the detail of computation for those unknowns.

5.1.2 Normal and Area Computation

In the implementation and scope of the dissertation, the word “panel” is utilized. It is a combination of a node and one-third of the neighbor triangular elements or one-fourth of neighbor quads. In SU2, all calculations proceed with this approach, also known as the node-based solver. A sample element is shown in Figure 9 to show the orientation of the element. In the figure, also some of the definitions that calculations use are demonstrated. SU2 puts the nodes on the surface element in order of the clockwise direction. Here, the face identification is $Face_i$, and similarly the panel is $Panel_i$

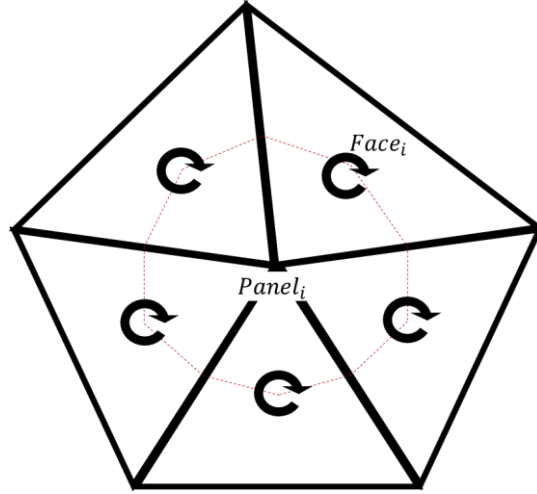


Figure 9: Sample demonstration of a surface grid element with definitions.

There are a couple of definitions to be introduced, as shown in Figure 10. CG_{Face_i} and $CG_{edge_{i-j}}$ are two central points of $Face_i$ and $edge_{i-j}$, respectively. One third area of the $Face_i$ neighbor to $Panel_i$ is named A_i .

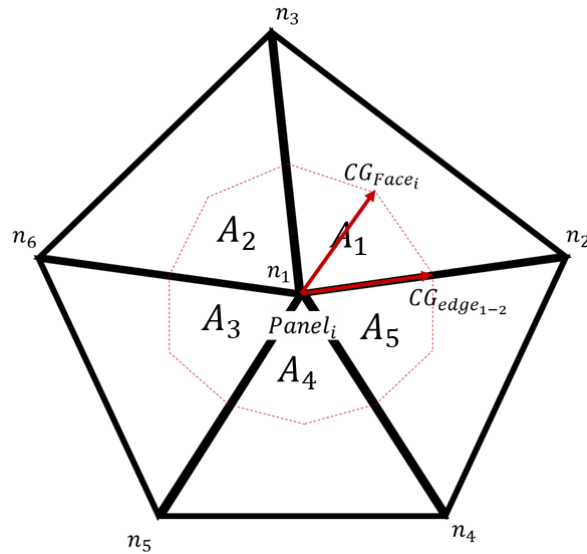


Figure 10: Area of a panel and related definitions.

After the definition, we can move on to compute normal and area. The normal vector is given by,

$$\vec{N}_i = |CG_{Face_i} - n_i| \times |CG_{edge_{i-j}} - n_i|, \quad (5.20)$$

where \vec{N}_i is the normal vector derived from the vectoral multiplication of two vectors depicted in the figure. The area, A_i , equals the magnitude of that vector as follows:

$$A_i = |\vec{N}_i| = Abs \left[|CG_{Face_i} - n_i| \times |CG_{edge_{i-j}} - n_i| \right]. \quad (5.21)$$

Now, it is possible to define the total area of $Panel_i$ and unit vector.

$$S_{Panel_i} = \sum_{i=1}^{NB} |\vec{N}_i|, \quad (5.22)$$

where S_{panel_i} is the area of the panel, and NB is the number of neighbor cells. The normal unit vector can be found by

$$\vec{N}_{Panel_i} = \frac{1}{S_{Panel_i}} \sum_{i=1}^{NB} \vec{N}_i. \quad (5.23)$$

While the calculated area is assigned in the global variable once, the computation of the normal vector continues through time-accurate simulations. The required inputs, coordinates of the nodes, are supplied by the CFD output file for each time step.

5.1.3 Velocity Computation

Velocity values utilized in the F1A formulation need to be obtained from the node coordinates. Output coming from CFD simulations contains only node coordinates and pressure data. By using the position change of the node in the defined time interval, velocity can be found. Herein, we use the 2nd order central difference method. The equation for the velocity of the node is given by

$$U_i^n = \frac{X_i^{n+1} - 2X_i^n + X_i^{n-1}}{2\Delta t} . \quad (5.24)$$

where U_i^n is velocity value for i th dimension and n th time step. Similarly, X_i^n is the coordinate of the node for i th dimension and n th time step.

5.1.4 Computation of Radiation Vector and Observer Time

One of the most challenging parts of the F1A formulation is the computation of observer time. After the acoustic source emits the noise, it takes some time for the observer to hear that noise. The time of that journey changes according to the distance between the observer and the source.

The observer point receives the signal from each source panel at different times based on the distance. Therefore, the elapsed time between noise generation and reception needs to be computed. Besides, as mentioned before, due to the wind tunnel configuration, radiation vectors depend on the time difference. For the moving observer and source, radiation distance can be written as

$$R = \sqrt{\sum_{i=1}^N (x_i - U_0 t - y_i - U_0 \tau)^2} , \quad (5.25)$$

where, τ and t are source and observer time, respectively. N is the dimension of the radiation vector, and radiation distance, R , represents the distance between observer \mathbf{x} and source \mathbf{y} points. Moreover, the time difference can be found by utilizing the following equation:

$$t - \tau = R/c . \quad (5.26)$$

The solution for t can be found by iterative solution by using equations (5.25) and (5.26). Consequently, R , r_i and \hat{r}_i terms are found from the solution of t .

For the sake of the memory load, the code employs a source-time-dominant algorithm. Brentner and Farassat [77] briefly explained the advantages of the source-time-dominant algorithm over the observer-time-dominant algorithm. Basically, the acoustic signal reaches the observer at different times, but they must be gathered in order. Using the source-time-dominant algorithm, first, acoustic propagation is computed based on the noise source. After, according to preferred observer time, the interpolation operator calculates the noise propagation at the observer point. That type of computation enables the aeroacoustic analysis with less memory usage and computation independent of the number of samples.

$$p'(\mathbf{x}, t^*) = I(p'(\mathbf{x}, t), t^*) , \quad (5.27)$$

where $I(\dots, t^*)$ is an interpolation operator and t^* is the desired observer time. In computations, the code employs, preferably, the 2nd order Taylor expansion for the polynomial interpolation as in the following equation.

$$p'(\mathbf{x}, t^*) = p'_i + (t^* - t) \frac{p'_{i+1} - p'_{i-1}}{2\Delta t} + \frac{(t^* - t)^2}{2} \frac{p'_{i+1} - 2p'_i + p'_{i-1}}{(\Delta t)^2} . \quad (5.28)$$

5.1.5 Fourier Transform

SU2-CAA code includes a subfunction to compute Fourier transformation. Employing Slow Fourier Transform (SFT), also called discrete Fourier transform (DFT), acoustic pressure time histories are converted into frequency-based data. Basically, calculations find the spectral power discretely summing of multiplication of exponential function and acoustic pressure as given by

$$A_m = \frac{1}{N} \sum_{k=0}^{N-1} p'(t_k) \exp\left(-\frac{2\pi i m k}{N}\right), \quad m = 0, 1, 2, \dots, N-1, \quad (5.29)$$

where, A_m is a complex coefficient in the frequency domain. N represents the number of samples utilized in the calculations. Now, it is possible to find acoustic power by multiplying the magnitude of A_m and period of acoustic pressure time history as follows:

$$G_{pp_m} = |A_m|^2 T, \quad m = 0, \quad (5.30)$$

$$G_{pp_m} = 2|A_m|^2 T, \quad m = 1, \dots, \frac{N}{2} - 1, \quad (5.31)$$

where, G_{pp_m} is power spectral density [76] and T is the period of acoustic pressure time history.

Then, it can be used to find the objective function described in the previous chapter. the mean square pressure per discrete band, between f_i and f_{i+1} , is given in the following equation.

$$p_{f,rms}^2 = \int_{f_i}^{f_{i+1}} G_{pp_m}(f) df, \quad i = 1, \dots, M-1. \quad (5.32)$$

5.1.6 Flow Chart of F1A Solver

In this section, the flow chart of the algorithm used for the F1A solver is discussed. The implementation principally applies the source time dominant approach described in Ref. [77-79]. Figure 11 demonstrates the details of the algorithm from start point to endpoint that we use to obtain acoustic pressure time history for all observer points.

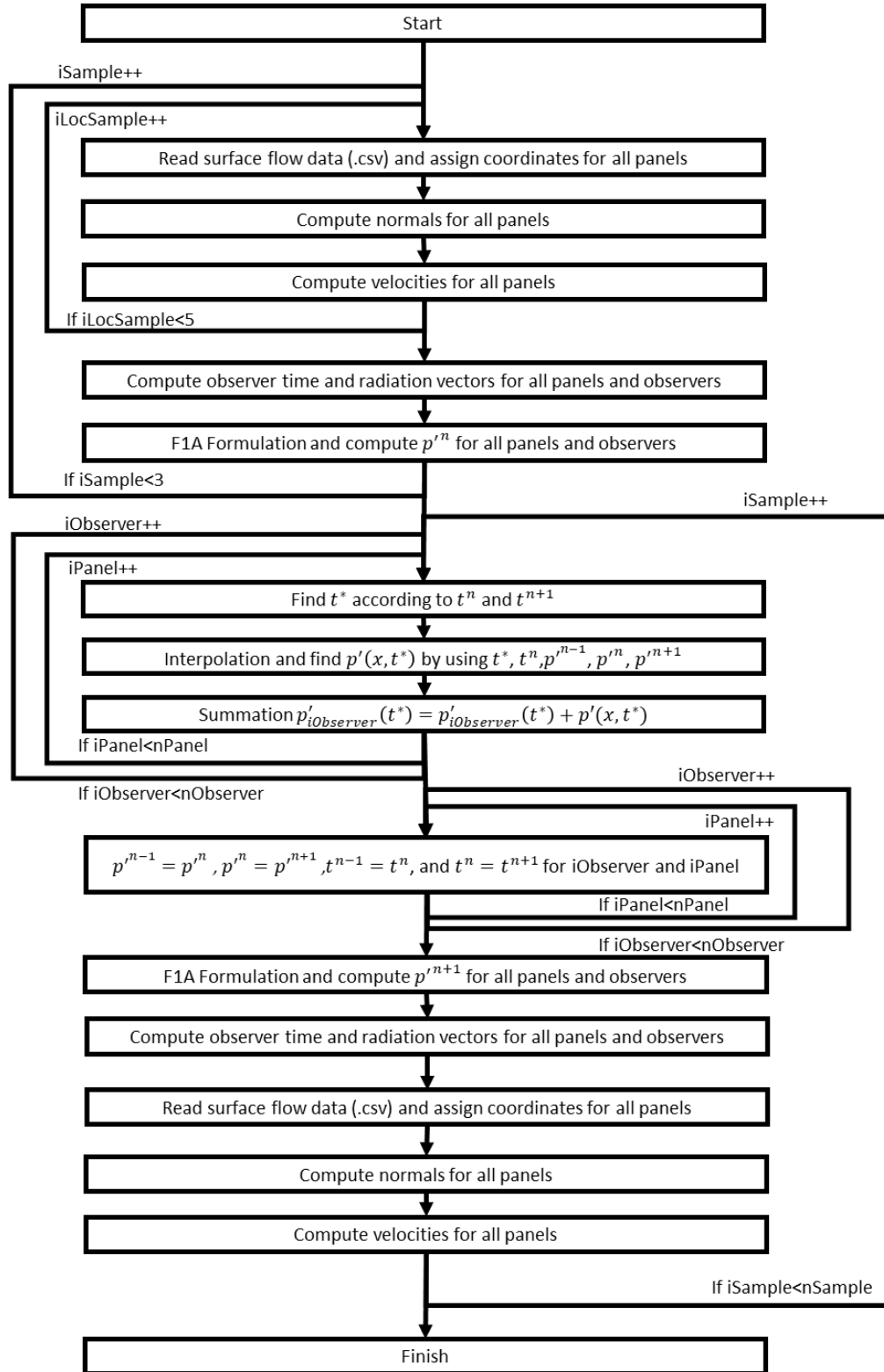


Figure 11: Flowchart of F1A solver.

At the start point, the solver allocates the arrays for pressure, coordinate, velocity, radiation, time, and normal vectors to contain the required operation in C++-based functions that complied with the number of time steps and observers. In the formulation, the time derivative of the velocity needs the velocity data from three-time steps. Moreover, there is velocity data in the CFD output, and the velocity values are obtained from time-accurate node coordinates. Therefore, the sample size of the allocated matrix should be five. The code reads surface flow data containing coordinates and pressure and assigns them into the relevant arrays based on that information. After, normal calculation computes normal vectors for all panels using node positions. The solver also uses the node position to compute velocity values. Then, observer time computation is completed. the time passing between noise propagation and receiving from the observer point is found. That enables the code to find radiation vectors as well. Those processes loop until the end of five consecutive local time steps. Then, p' is computed for the first three time steps and all observers and panels.

The desired time, t^* , is derived by equally dividing the time interval between the maximum and minimum time that the observer perceives the signals. The minimum time corresponds to the latest signal in the first group of the propagated signals from the panels. The maximum time is equal to the first signal in the latest group of the propagated signals.

After the preprocessing section, p' is computed for all time steps, panels, and observers. Here, the solver finds the t^* according to source times t^{n-1} , t^n , and t^{n+1} . Based on those values and obtained interpolation coefficients, we find $p'(x, t^*)$. Then, the code computes the summation as given by,

$$p'(t^*) = \sum_{iPanel=0}^{nPanel} p'(iPanel, t^*), \quad (5.33)$$

and that process repeats for each observer point. After, the code assigns the variables at the current time into one step lower time indices. Next, the algorithm computes p' for the following sample. Similarly, at the next steps, the required values for the F1A solver are computed, such as radiation, normal, and velocity vectors. This calculation continues until the cycle reaches the maximum sample size.

In the end, the solver finds acoustic pressure time history for every observer point. Furthermore, if it is a parallel computation, the MPI operator works and finds combined acoustic pressures. Then, DFT and SPL computations follow, and the code extracts required outputs to assess aeroacoustic results. Also, for post-processing, code can generate the data, including acoustic pressure and its breakdowns, in .vtk format.

5.1.7 Parallel Computation

SU2 software requires an interface to perform parallel computations. The OpenMPI, communicating the multiple processors, is embedded into the SU2 suite. Message Passing Interface (MPI) manages the communication between processors [80]. It has many protocols and functions to combine, distribute and operate the data.

Those functions are fully functional and used in both SU2-CFD and SU2-CAA tools. In addition, the call functions, such as Reduce, Allreduce, Gather, and Allgather (details can be found in Ref. [80]), are employed in various sections of the code. Besides, the domain decomposition is performed by the Parmetis algorithm [81] in SU2. The decomposition algorithm splits the domain into the prescribed number of parts in the most cost-effective ways. The decomposed domain shares the cell called the halo layer, as seen in Figure 12. The edge points composing the halo layer are named edge points. In each processor, information about the halo layer is missing at the beginning. Therefore, it should be calculated by communicating each

edge point. In that way, we can compute the normal vectors and the area so the acoustic pressure can be predicted in parallel.

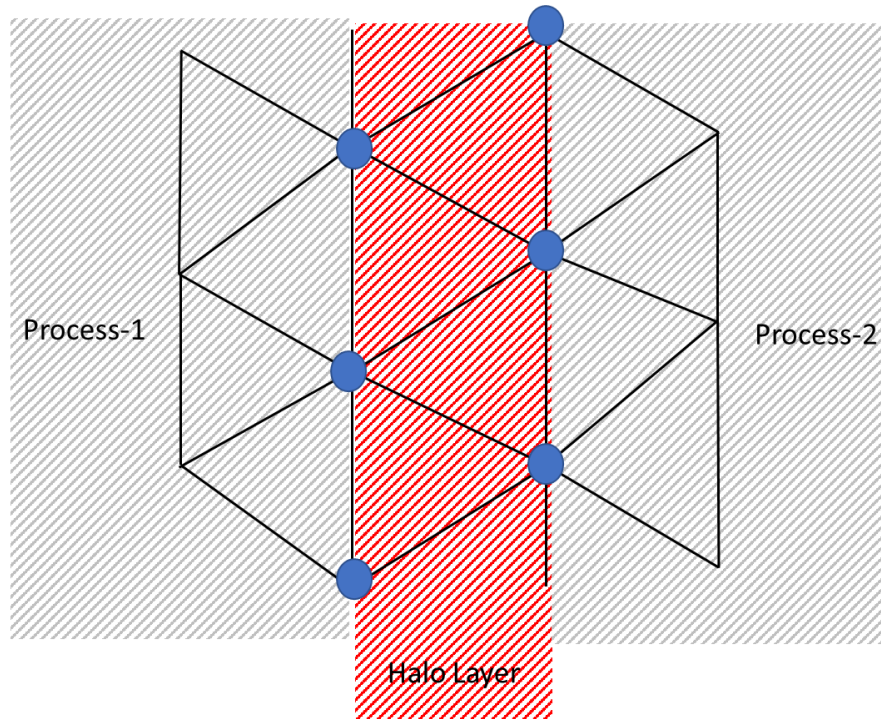


Figure 12: Demonstration of the halo layer and edge points.

Before the essential computation, the code computes connectivity and node-to-face matrices. Additionally, it establishes the arrays allocating halo faces, edge points, and neighbor processors. After obtaining all the required information, the normal and area computations are performed by accounting for the contribution of the halo layer. In the end, SU2-CAA solver can compute acoustic pressure in parallel mode with the same accuracy level. The performance analysis of the computation with parallel processing will be discussed in the application sections.

5.2 Sensitivities

Gradient values with respect to a specific variable, for example the design parameters, can be efficiently calculated by solving the adjoint equation. In the present study, both the aerodynamic and aeroacoustic gradients are derived by the adjoint approach and are then implemented in the algorithmic differentiation utility, CoDiPack [53].

The CoDiPack utility has previously been implemented in SU2 as a built-in function that can be called through the computational processes. First, the developed CAA code includes the adjoints stored for each variable within the panel on the surface and the sample loop. Through the acoustic computations, the recording of the dependencies continues until the determination of the objective function. Once the objective function is introduced, the algorithmic differentiation (AD) tool computes adjoints. the precision of the AD-based partial derivatives needs to be declared. To verify the accuracy of the gradients obtained by algorithmic differentiation, they are compared with gradients computed by complex differentiation (CD) [82, 83].

5.2.1 Algorithmic Differentiation in F1A Solver

Acoustic sensitivities with respect to conserved variables need to be computed in the SU2-CAA solver. The protocol standard is defined in Ref. [44]. Utilizing the same procedure, the partial derivatives are derived. The conserved variables are introduced as dependent variables using the syntax shown in Figure 13. The registration subroutine is embedded into the F1A solver, as depicted in Figure 14. The computed variables, velocity, coordinates, and pressure, enter the subroutine and obtain conserved variables. Then, the obtained conserved variables are introduced as dependent variables.

```

AD::RegisterInput(x);
AD::RegisterInput(y);
AD::RegisterInput(z);
AD::RegisterInput(rho );
AD::RegisterInput(rho_ux);
AD::RegisterInput(rho_uy);
AD::RegisterInput(rho_uz);
AD::RegisterInput(rho_E);

```

Figure 13: Registration flags for dependent variables.

In the solver, the dedicated subroutine, “RegisterVariables,” performs the required computation steps as mentioned above. Next, velocity, coordinates, and pressure are calculated back and fed into the system. Then, the F1A solver proceeds through all panels, samples, and observers. After, the objective function is found, and partial derivatives are computed by using the built-in function, “AD::ComputeAdjoint().” Figure 15 demonstrates a flow chart of the high-level approach for the computation of acoustic adjoints embedded in SU2_CAA.cpp. At the final point, partial derivatives are pulled and devoted to variables. Then, $\partial J/\partial U$ and $\partial J/\partial X$ extracted to be utilized in adjoint solver.

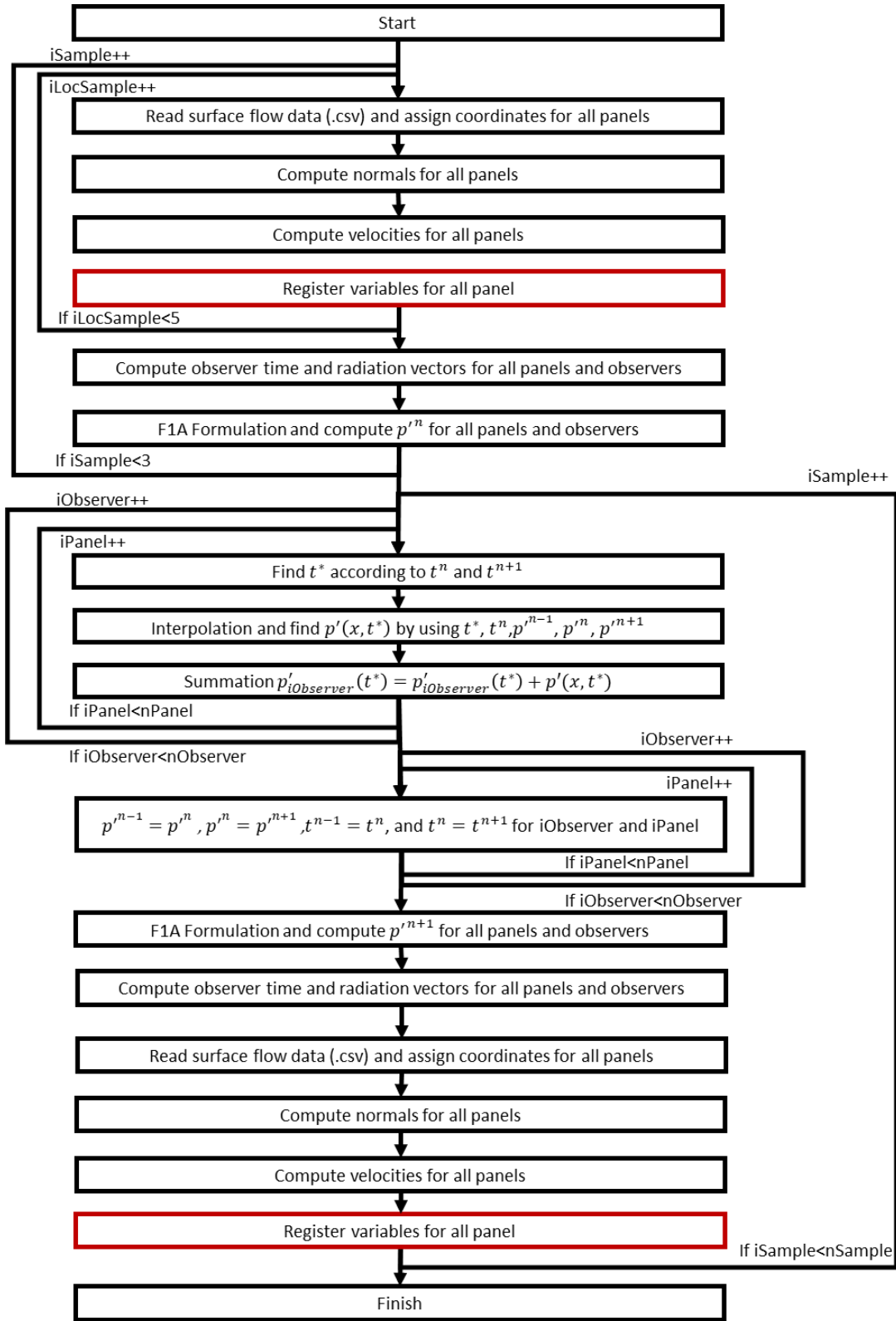


Figure 14: Flowchart of F1A solver for variable registration.

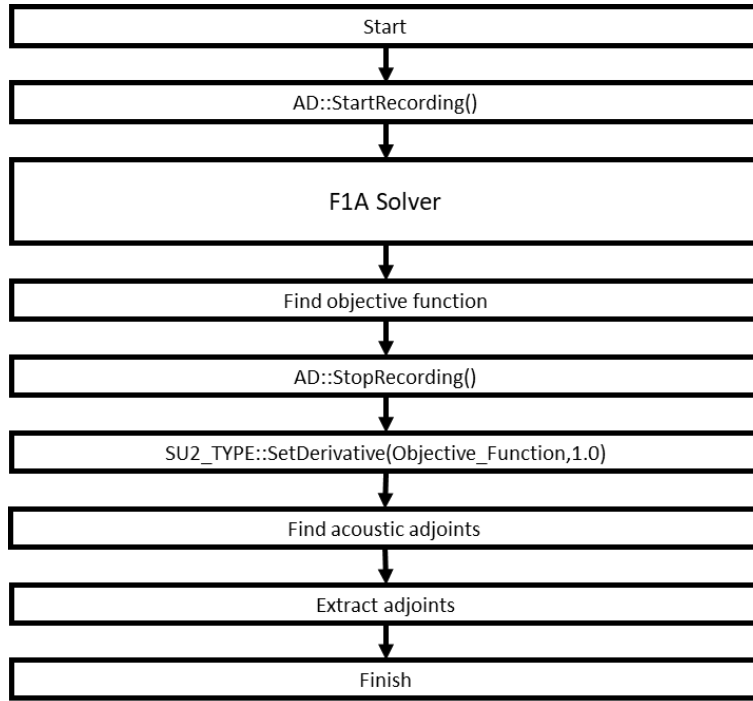


Figure 15: Flowchart of CAA solver for acoustic adjoints.

5.2.2 Complex Differentiation in F1A Solver

For the verification processes, Complex Differentiation (CD)-based results are compared with AD-based results. CD uses the effects of small perturbation in a variable on the objective function. The perturbation is introduced as a complex number and added to the conserved variable. In the end, the imaginary part of the objective function divided by step value gives partial derivatives as follows [83]:

$$F'(x_0) \approx \frac{\text{Im}(F(x_0 + ih))}{h}, \quad (5.34)$$

where the step value, h , is set to 10^{-50} for the perturbation. The reason for preferring that small number is to increase the accuracy of derivatives. The implemented method includes computation for only one node and one sample. Using the applied perturbation on the node, it is

possible to find partial derivatives. utilizing both CD and AD, comparisons of acoustic Adjoint are discussed in Chapter 6, while the results for applications are being evaluated.

5.3 SU2 integration

The developed code should be integrated into the SU2 suite practically. For example, in the standard configuration file, the aeroacoustic functions need to be callable. Also, the addition of the CAA solver must work collaboratively with other SU2 functions. Aligned with those requirements, functions for the aeroacoustic computation are placed in a separate folder called “SU2-CAA,” as in Figure 16. The SU2-CAA folder and its child scripts handle the aeroacoustic operation fully functional and well-integrated with SU2 v7.1.1. For now, SU2-CAA uses only the F1A solver, whereas, in future work, it will be possible to embed a new acoustic solver into the system.

In addition, to employ SU2-CAA in the primal or Adjoint solution process, the contents of some of the libraries differ. The modified libraries are demonstrated in Figure 16 as framed blue. The modifications in those libraries are discussed in the following section.

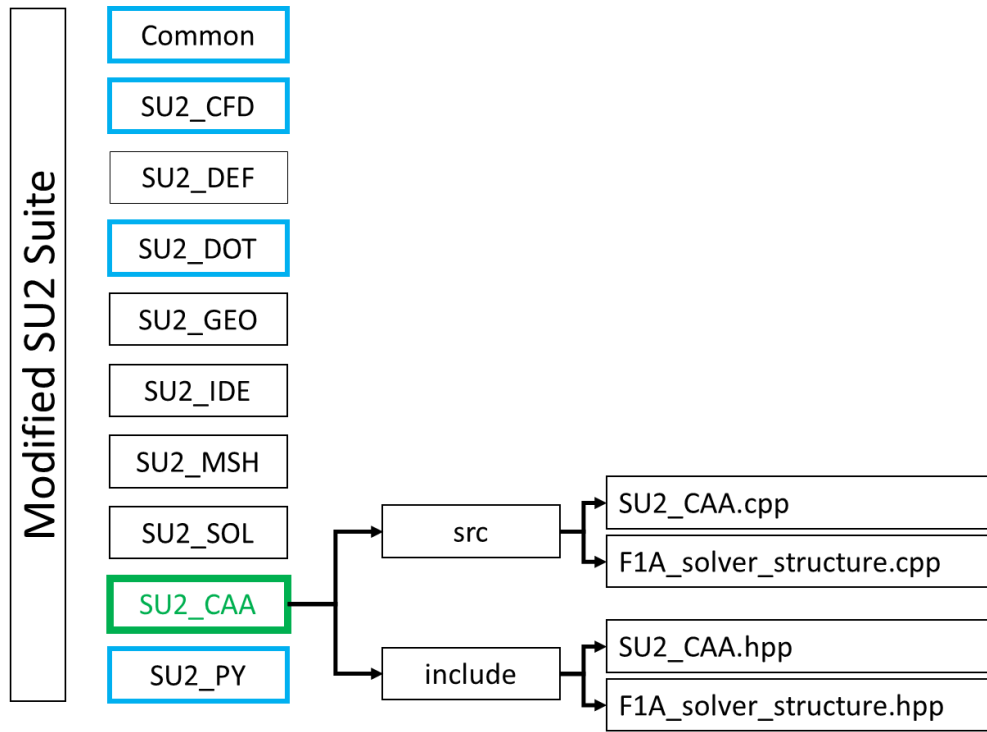


Figure 16: Placement of SU2-CAA in SU2 suite.

5.3.1 Modifications on SU2 libraries

In addition to the SU2-CAA folder, many folders include modifications made during the adjoint-based CAA solver implementation into SU2. The modified child C++ and python files are shown in Figure 17 & Figure 18. First, to use a standard configuration file to handle both CFD, CAA, and optimization runs, the CConfig.cpp file is modified. Besides, part of the adjoint-based sensitivities for the acoustic objective is managed in the CPhysicalGeometry.cpp file. For setting twist angle as a variable for propeller cases, required changes are performed in CSurfaceMovement.cpp. In the SU2_CFD folder, major changes include coupling of flow and acoustic adjoints. The implementation of Lagrangian-driven adjoint formulations exists in that folder.

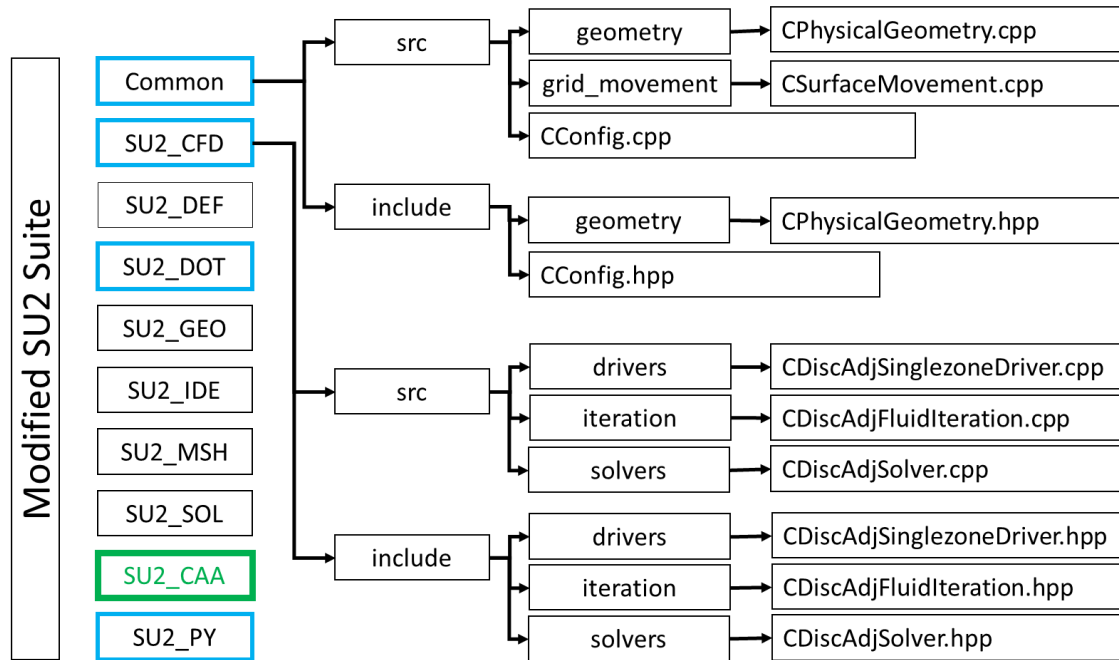


Figure 17: Modifications on SU2_CFD and Common folders.

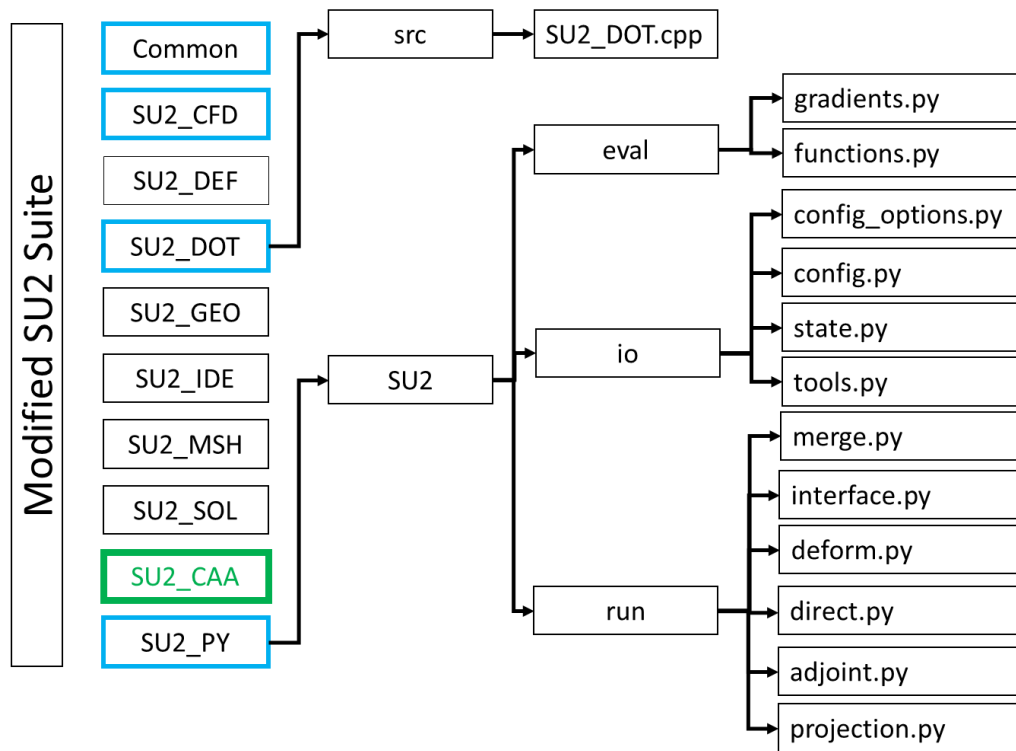


Figure 18: Modifications on SU2_DOT and SU2_PY folders.

The SU2_DOT folder manages sensitivities and gradient outputs with respect to the design variables. In the scope of the dissertation, the acoustics objective function is implemented with some new flow variables that are not covered in the original SU2 suite. Moreover, the Python library, SU2_PY, manages the optimization process. The implemented code schemes are convenient to use multipoint and multidisciplinary optimization, including the developed CAA solvers. Briefly, the modified python library conducts direct simulations for aerodynamics and aeroacoustics. Then, it performs adjoint simulations and obtains sensitivities by projections. In the end, by repeating those processes and evolving design, it optimizes the shape or flow variables of the defined problem. Further details of the code modifications are not delivered in the presented dissertation but may be reachable in Github Sharepoint in the future.

5.3.2 Extensions in SU2 Configuration File for the Developed Features

All implementation covered in previous sections must be manageable by the user. In SU2, all simulations are managed by a single configuration file. The extension, including the flags managing the developed feature, is implemented into the SU2 config file in parallel with that approach. The following flags manage the inputs for the developed features.

First, Figure 19 demonstrates the user inputs for aeroacoustic definitions. If the objective function is defined as “NOISE,” the aeroacoustic solver runs and computes required outputs. Herein, iteration details such as first, last, and interval iterations are given. Moreover, the MARKER_CAA flag includes the acoustic boundaries that the noise emitted. The code reads the locations of the observer from a file given in the ACOUSTIC_OBSERVER_FILENAME flag. Additionally, there are a couple of inputs to describe sensitivity calculations. Those are the switches for types of differentiation, objective function, and output for post-processor.

```

%----- AEROACOUSTIC DEFINITION -----%
%
% Objective function
OBJECTIVE_FUNCTION=NOISE
%
%prescribed motion for acoustic (if yes applicable only for rotation and stationary
% motion) check the motion details.
ACOUSTIC_PRESCRIBED_MOTION= NO
%
ACOUSTIC_FREQ=360
%
% Marker(s) of the surface for the acoustic evaluation
MARKER_CAA = ( blade_3,blade_2,blade_1 )
%
%Restart Iteration
ACOUSTIC_ITER_RESTART= 601
%
ACOUSTIC_ITER_TOTAL= 280
%
ACOUSTIC_ITER_INTERVAL= 1
%
ACOUSTIC_TIME_TOLERANCE=1e-9
%
%Filename for Observer/Microphone locations for CAA sims
%Sample format:
%2
%0.0000 1.0000 3.0000
%0.0000 1.0000 4.0000
ACOUSTIC_OBSERVER_FILENAME= Observer_Locations.dat
%
%CD: Complex diff. if no it uses algorithmic diff
ACOUSTIC_CD= NO
%
%if CD step value
ACOUSTIC_CD_STEP_VAL= 1e-50
ACOUSTIC_CD_IVAR= 0
ACOUSTIC_CD_ISAMPLE= 5
ACOUSTIC_CD_IPANEL= 5
ACOUSTIC_CD_IZONE= 0
%
%Type of Acoustic objective function ( OASPL(YES) or ppRMS(NO) )
ACOUSTIC_OBJ_FUN_OASPL=NO
%
%Output format for Acoustic analysis for postprocessing (TECPLOT or PARAVIEW)
ACOUSTIC_OUTPUT_FORMAT= TECPLOT

```

Figure 19: Configurations for aeroacoustic definition.

In addition, the content of the optimization definition is extended by additional input types, as seen in Figure 20. The multipoint optimization needs inputs for each flight condition, so the definitions of individual inputs are defined here. Moreover, the new objective flag,

MULTIPOINT_NOISE, is introduced in the configuration file. In this work, three main variables, FFD_CONTROL_POINT, FFD_TWIST, and OMEGA, are utilized. FFD_TWIST and OMEGA are the new definitions obtained from the developments.

```
% ----- OPTIMAL DESIGN DEFINITION -----%
%
% Definition of multipoint design problems, this option should be combined with the
% the prefix MULTIPOINT in the objective function or constraint (e.g. MULTIPOINT_DRAG, MULTIPOINT_LIFT,
% etc.)
MULTIPOINT_WEIGHT= (0.5, 0.5)
MULTIPOINT_MACH_NUMBER= (0.11, 0.00)
MULTIPOINT_FREESTREAM_PRESSURE= (101325.0, 101325.0)
MULTIPOINT_FREESTREAM_TEMPERATURE= (288.15, 288.15)
MULTIPOINT_OBSERVER_FILENAME= (Observer_Locations.dat, Observer_Locations.dat)
MULTIPOINT_MACH_MOTION= (0.6663065, 0.6663065)
MULTIPOINT_ROTATION_RATE= (-753.9570247 0.0 0.0, -753.9570247 0.0 0.0)
%
% Optimization objective function with scaling factor
% ex= Objective * Scale
OPT_OBJECTIVE= MULTIPOINT_NOISE
%
% Optimization constraint functions with pushing factors (affects its value, not the gradient in the python
% scripts), separated by semicolons
% ex= (Objective = Value ) * Scale, use '>','<','='
OPT_CONSTRAINT= ( MULTIPOINT_DRAG < -0.006 );
% Upper bound for each design variable
OPT_BOUND_UPPER= 0.012
%
% Lower bound for each design variable
OPT_BOUND_LOWER= -0.012
%
% FFD_CONTROL_POINT ( 11, Scale | Mark. List | FFD_BoxTag, i_Ind, j_Ind, k_Ind, x_Mov, y_Mov, z_Mov )
% FFD_TWIST ( 15, Scale | Mark. List | FFD_BoxTag, j_Ind, x_Orig, y_Orig, z_Orig, x_axis, y_axis,
% z_axis )
% OMEGA ( 201, Scale | 1.0 )
% Optimization design variables, separated by semicolons
DEFINITION_DV=(11, 1.0 | blade_3 | BLADE_3, 0, 0, 0, 0, 0.0, 0.0, 1.0);
(15, 10.0 | blade_3 | BLADE_3, 6, 0, 0, 0, 0.0, -0.86602540, -0.5);
(201, 1.0 | 1.0)
```

Figure 20: Configurations for optimal design definition.

CHAPTER 6

AEROACOUSTICS APPLICATIONS

In this chapter, the results obtained from the application of the developed code are discussed. Various kinds of applications test the code from different points of view. First, a unit sphere is selected as an object to develop the early phase of the code. The investigations for the sphere geometry include two types of noise source definition: stationary and rotating surfaces in the wind tunnel. Secondly, a simple rotor geometry, the Caradonna-Tung rotor, is utilized to demonstrate the rotor application. Thirdly, the propeller geometry of the XV-15 tiltrotor is investigated. The results of the CAA analyses are compared with ANOPP2 software. Next, the simulations for NASA's three-bladed helically twisted prop rotor are conducted. Finally, WIPP geometry and four-bladed ideally twisted rotors are used to show the multizone capabilities of the presented code.

6.1 Flow Past Sphere in Wind Tunnel

A stationary unit sphere is subjected to the flowfield in a wind tunnel configuration. The rationale behind this choice is the simplicity of the geometry, which allows code debugging in significantly less time to generate a mesh and run the case on a computer. The flow disturbances generate the noise as they negotiate the curvature of the sphere. Shown in Figure 21 are the computed pressure field on the sphere surface (Figure 21(a)) and its wake (Figure 21(b)) for flow at Mach 0.5. Also, to observe the effect of changing the freestream Mach number on the wake flow, the computations are also repeated for Mach 0.1 and Reynolds number 1.14×10^6 [84].

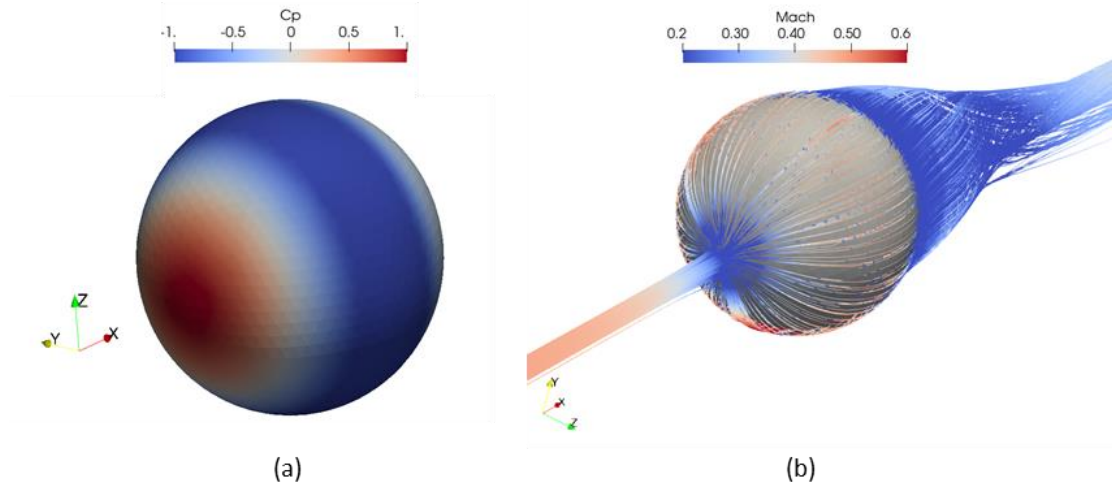


Figure 21: (a) Computed pressure coefficient distribution on a unit sphere and (b) its wake.

The pressure fluctuations on the sphere surface, obtained from CFD, are handed over as input to the presently developed CAA routines of the SU2 code. Presented Figure 22-Figure 25 are the pressure fluctuations propagated to observers at ten diameters and 14 diameters above the sphere center for Mach numbers 0.5 and 0.1. The propagation is predicted in two different ways, then compared, first by the present CFD method, then by the F1A formulation (Figure 22-Figure 25). For these low Mach number flows, the CFD results reasonably match those obtained by F1A. It should be noted that the F1A formulation neglects the quadrupole noise terms, which would represent the noise component due to viscous effects and turbulence. It is expected that with a denser mesh resolution at the observer location, the comparison should improve but only until the acoustic signals succumb to the numerical dispersion error of this second-order CFD method.

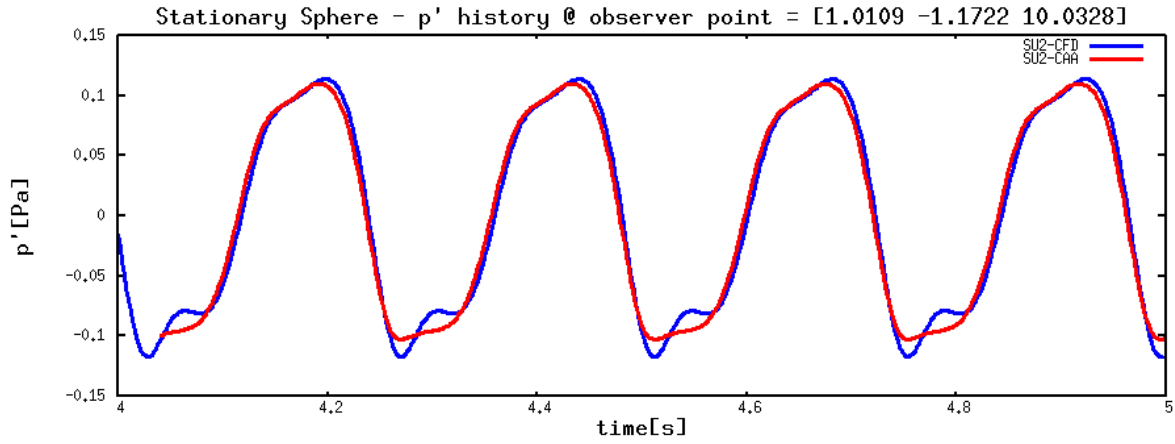


Figure 22: Comparison of F1A computed pressure propagation with CFD results. $M_\infty=0.5$ and the observer at ten diameters away.

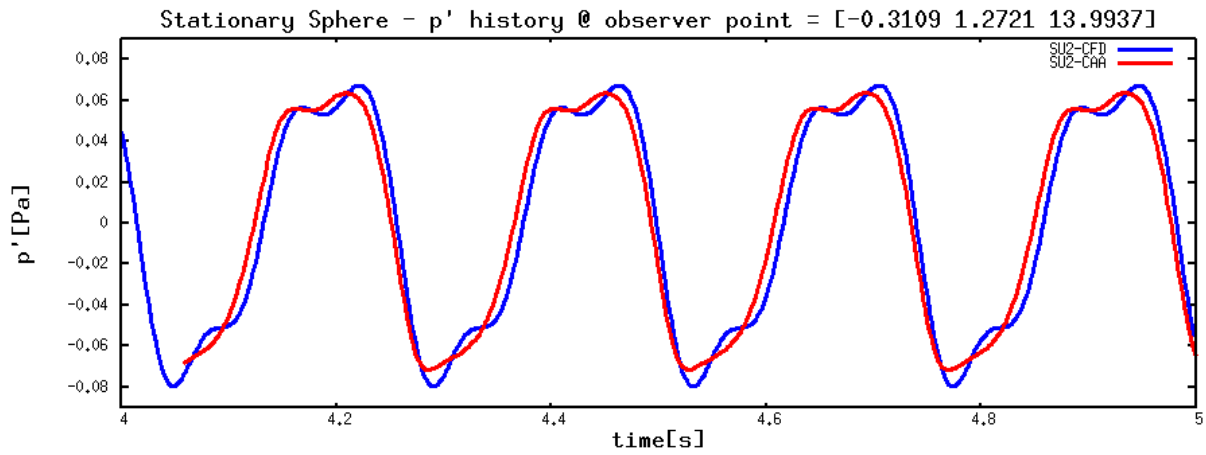


Figure 23: Comparison of F1A computed pressure propagation with CFD results. $M_\infty=0.5$ and the observer at 14 diameters away.

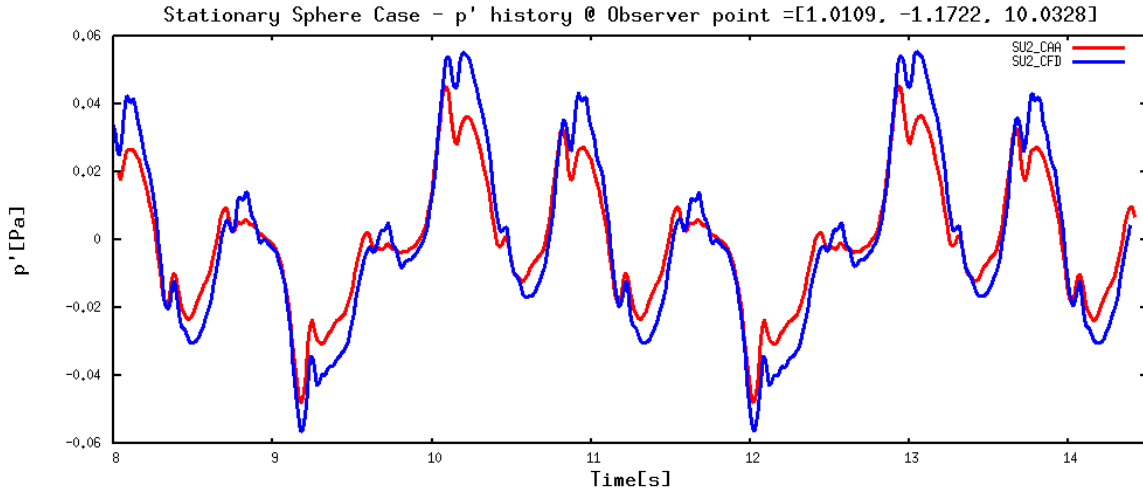


Figure 24: Comparison of F1A computed pressure propagation with CFD results. $M_\infty = 0.1$ and the observer at ten diameters away.

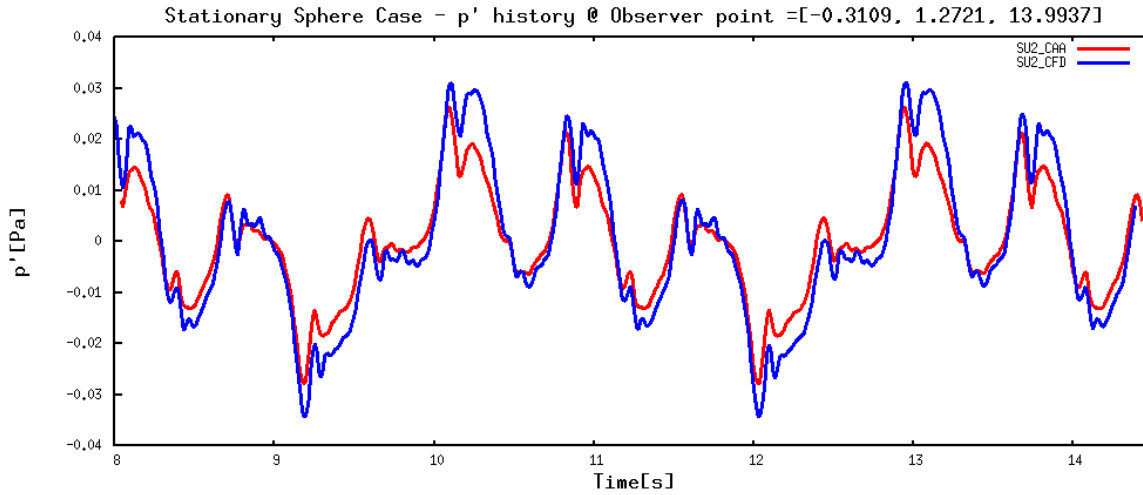


Figure 25: Comparison of F1A computed pressure propagation with CFD results. $M_\infty = 0.1$ and the observer at 14 diameters away.

6.1.1 Rotating Sphere

The previously described sphere is again considered, but now it is rotating. The rotation is computationally accounted for by rotating the entire CFD mesh as a rigid body. That is, there is no mesh deformation, and cells do not move relative to the sphere. For developing the code for a rigid body motion, this case appears to be very relevant due to the simplicity of its geometry and its motion. The rotation rate is 85 rad/s in the flow direction. The freestream flow parameters remain the same as in the stationary sphere example.

As in the stationary sphere case, comparisons are made for the fluctuating term computed at the observer location, which is ten diameters away from the sphere center. Here, the rotating and the freestream Mach numbers are 0.12 and 0.5, respectively. In the CAA analysis, the observer point is considered fixed, e.g., the coordinates are [0.0, 0.0, 10.0]. However, the virtual pressure probe, recording the computed CFD values, is rotating with the sphere's rigid body motion. Therefore, the probe coordinates are not at the same distance from the source. Consequently, the values gathered from the probe show an oscillatory behavior. This is displayed in Figure 26, where pressure fluctuations computed from CFD demonstrate jaggedness, while CAA produces a rather smooth distribution.

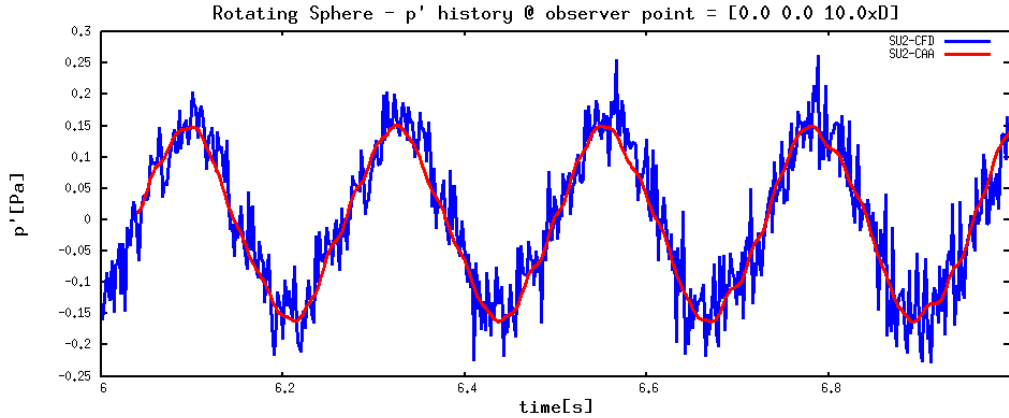


Figure 26: Comparison of F1A-computed pressure propagation with CFD results for a rotating unit sphere.

6.2 Caradonna-Tung Rotor

The first rotorcraft example, the Caradonna-Tung rotor, is introduced here. It is a 2-bladed rotor constituted constant NACA0012 airfoil along the blade. Chord length and pitch angle are also constant in the span direction. There are several configurations with different collective pitch angles, as described in Ref. [85]. The preferred configuration consists of the rotation rate and collective pitch angle equal to 1250RPM and 8-degree, respectively, as demonstrated in Figure 27.

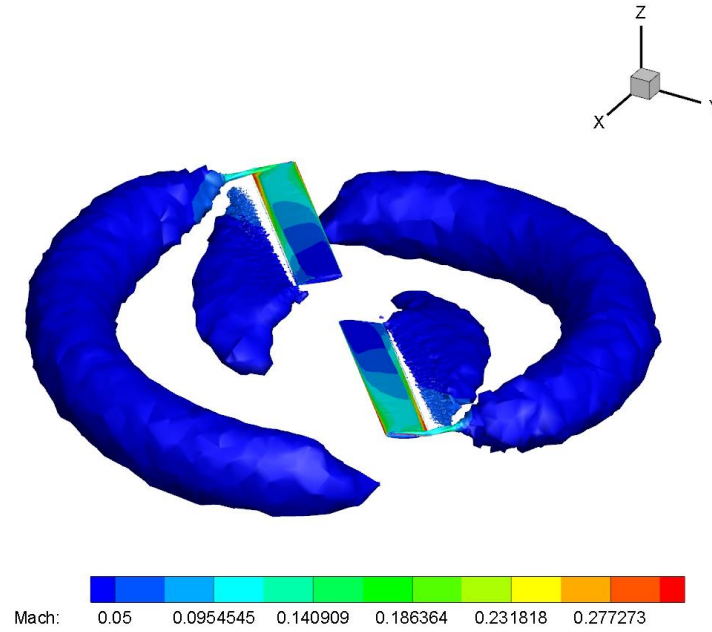


Figure 27: CFD simulations of Caradonna-Tung rotor: Mach distribution over blades and isosurfaces for tip vorticities.

The pressure coefficient distribution along the airfoil at some radial stations of the blade is demonstrated in the reference study for the considered configuration. The first comparisons between experimental data and CFD results are shown in Figs. Figure 28 and Figure 29, indicating the radial station at r equal to $0.96R$ and $0.89R$, respectively. CFD-based results align with the reference study for the pressure coefficient distributions.

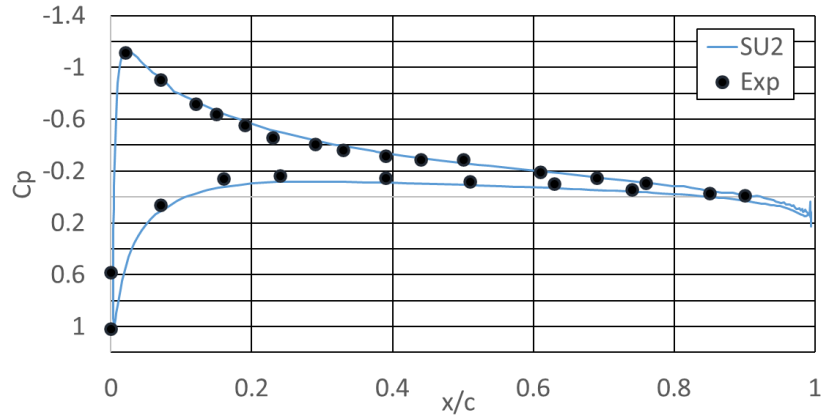


Figure 28: Comparison of SU2 and experiment [85] for pressure coefficient distribution along the airfoil at $r = 0.96R$.

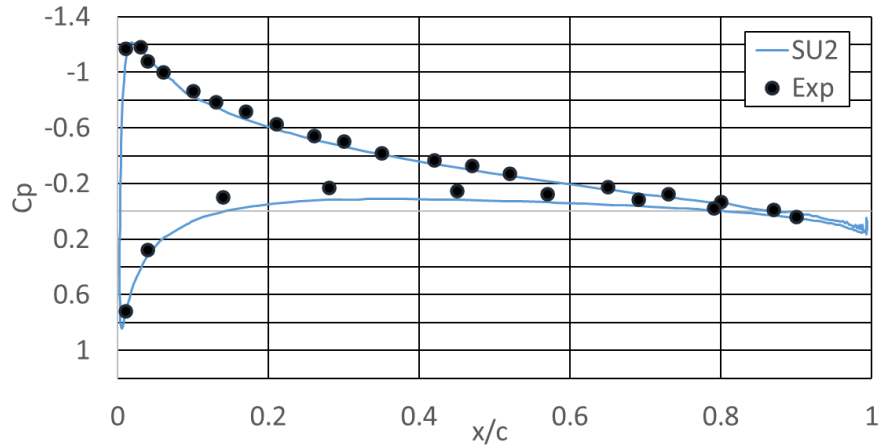


Figure 29: Comparison of SU2 and experiment [85] for pressure coefficient distribution along the airfoil at $r = 0.89R$.

Aeroacoustic simulations are conducted after the flow simulation acquires a regime constituting periodicity in terms of drag and lift coefficient histories. The simulation proceeds to extract the required outputs for CAA simulations for a while. Then, the aeroacoustic simulations are performed. To measure the precision and accuracy of acoustic calculations, a benchmark

study is conducted. As a benchmark tool, NASA's well-known prediction tool, ANOPP2 [86, 87], is utilized. The input data, the node coordinates, and pressures on the nodes are shared with ANOPP2. That provides consistency and assists in finding discrepancies resulting from acoustic solver-only errors. Both ANOPP2 and SU2-CAA conduct simulations and get acoustic pressure time history for the specified observer locations. For this geometry, an acoustic pressure time history data for a far-field observer and directivity of root mean square of acoustic pressure are presented in this dissertation. Firstly, Figure 30 shows the comparison of the aeroacoustic predictions attained from SU2-CAA and ANOPP2 for an observer point 100-diameters away in the in-plane direction.

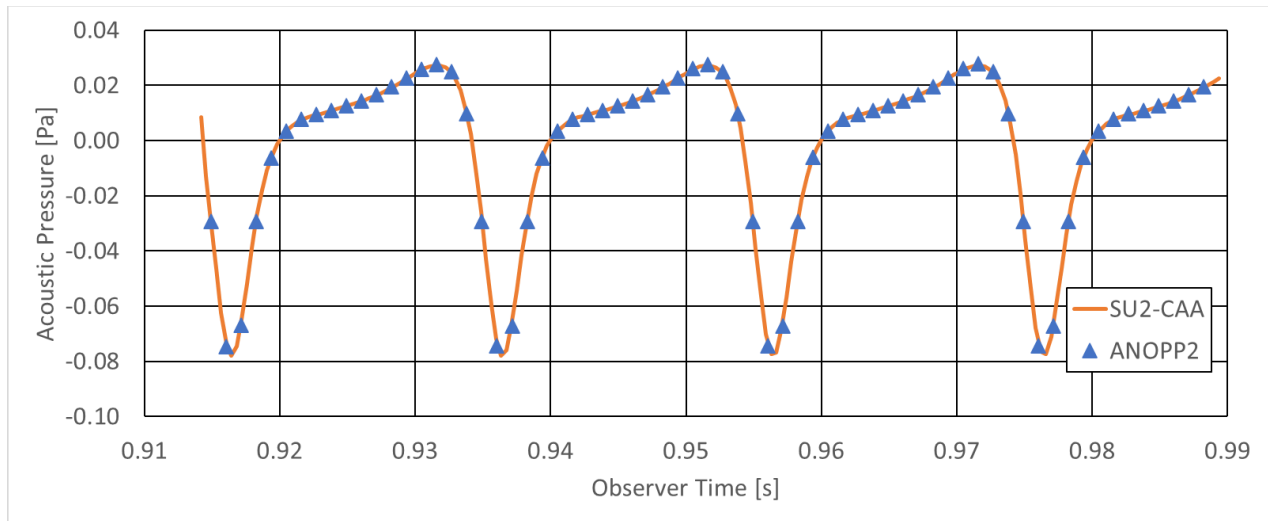


Figure 30: Comparison of SU2-CAA and ANOPP2 predictions for the observer location at 100-diameter away in-plane direction.

Secondly, a conducted directivity analysis demonstrates the comparisons for various microphone positions in Figure 31. The positions of the observers are in polar coordinates. Due to the assumption of symmetrical propagation in the rotation axis, the results are demonstrated

with only one angle and radial distance. As a final comment, The SU2-based results match with the benchmark tool successfully.

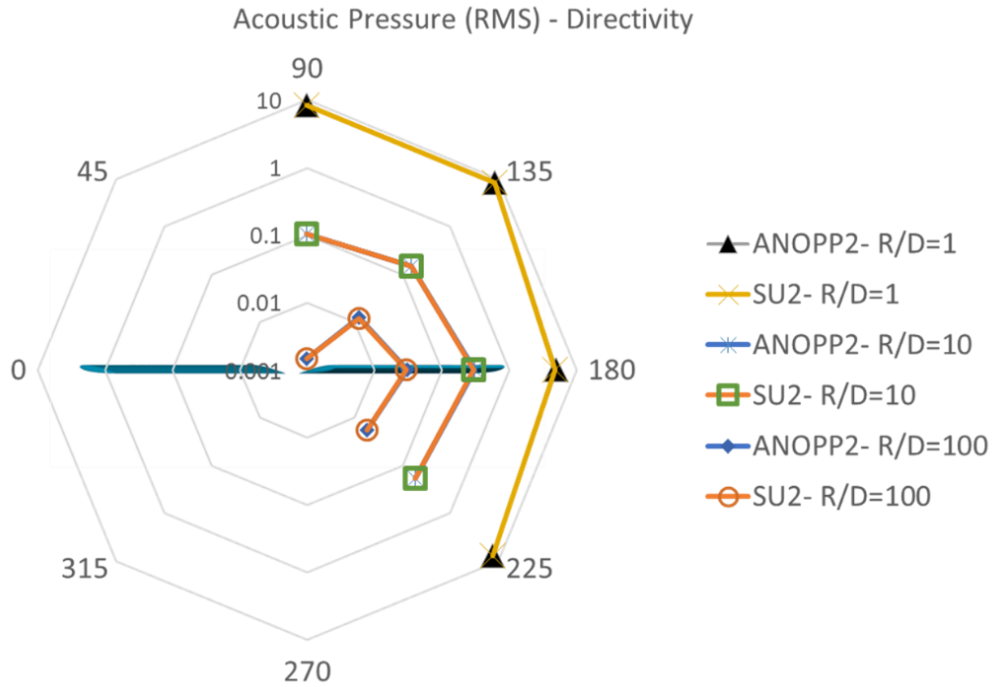


Figure 31: Directivity comparisons of root means squared acoustic pressure values for the observers.

Additionally, a comparison of the breakdown terms can show the precision of benchmarking. The developed code can also extract output that is usable in Paraview for post-processing. The output geometry consists of both actual and sigma surfaces. The sigma surface represents the shape of noise sources that the observer receives with the noise signal at the exact moment. we compare the ANOPP2 outputs in Tecplot and SU2-CAA outputs in Paraview in Figure 32. The distributions of the first term of the dipole component over sigma surfaces appear identical.

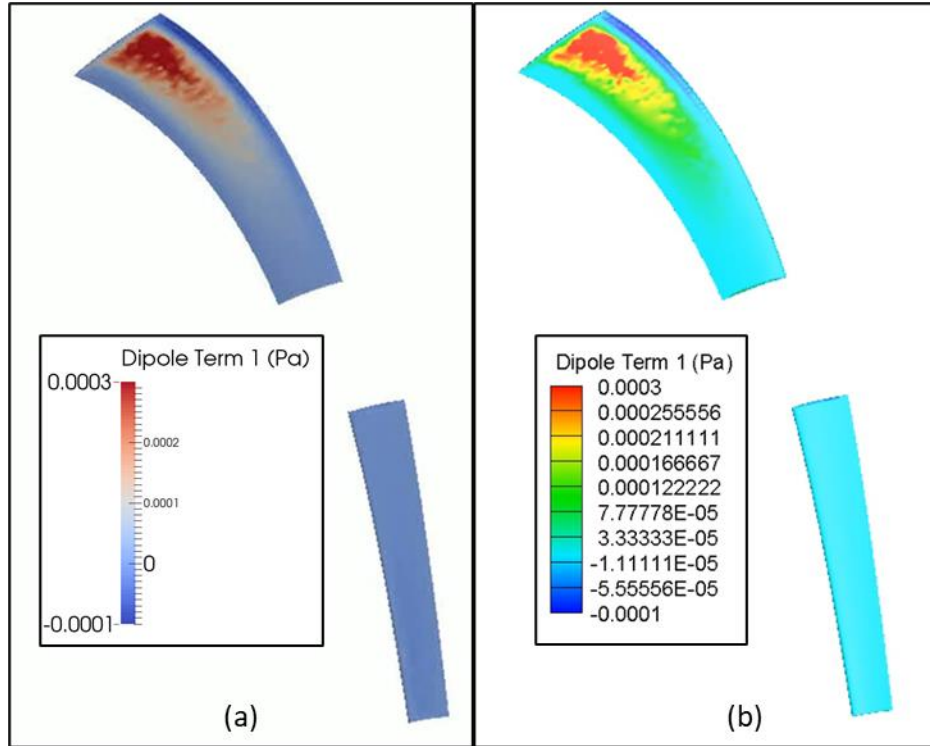


Figure 32: Distribution of acoustic dipole term over instantaneous sigma surface obtained from (a) SU2-CAA and (b) ANOPP2.

6.2.1 Computational Cost Analysis of SU2-CAA Code

Computation time cost and memory usage are critical parameters for code development and, therefore need to be evaluated in detail. Aeroacoustic simulations are executed on Wahab Cluster in High-Performance Computer (HPC) at Old Dominion University. The performance of the computing listed here depends on the computer power at the cluster.

In computations, the effects of the increasing number of observers, samples, and Computer Power Units (CPUs) on computation time and memory are investigated. In further computations, including numerous observers, nodes, and time steps, memory usage must be

constant and independent of those parameters. Besides, the wall clock time and CPU time should be at a reasonable level. Figure 33 shows the number of observers used in the computation versus wall clock time in seconds. In parallel with the expectations, an increasing number of observers increases wall clock time for both cases. Utilizing a larger number of CPUs for parallel computing reduces the time cost but not proportional to increment in CPU usage. Another outcome is that when the total time step in the computation increases two times, wall clock time increments at the same rate as expected.

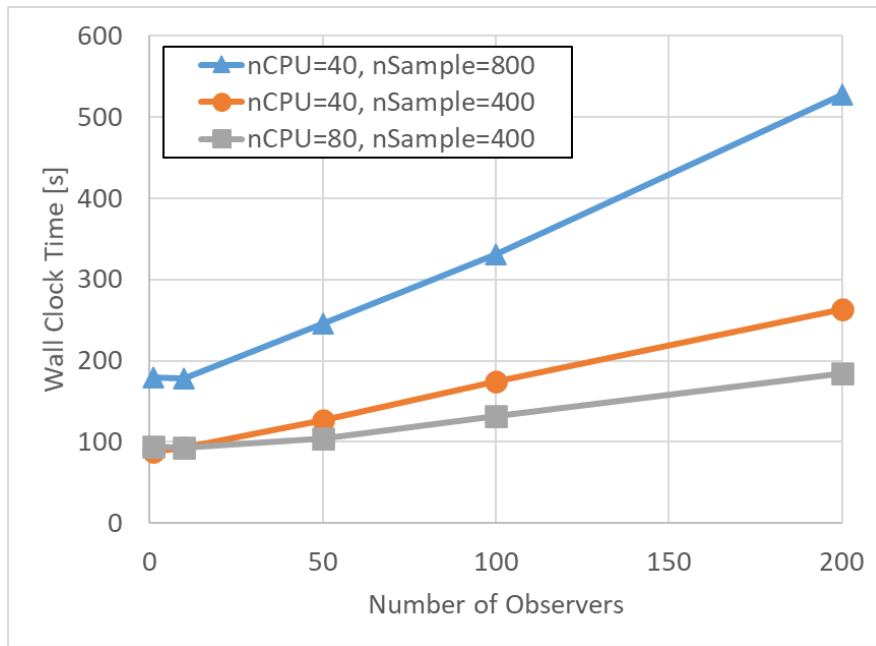


Figure 33: Number of observers versus wall clock time for different CPUs and time steps.

The most crucial performance criterion is memory usage that must be constant despite the increasing number of observer and time steps. Otherwise, when a larger number of time steps or microphones is required, the computation may fail. Figure 34 demonstrates memory usage during the computations for a different number of observers. While the number of microphones

increases, the allocated memory remains constant in every computation. Also, increments in the sample size do not affect memory usage. That situation prevents any memory leak and excessive usage in more complex and refined computations. Considering these demonstrations, the code works efficiently.

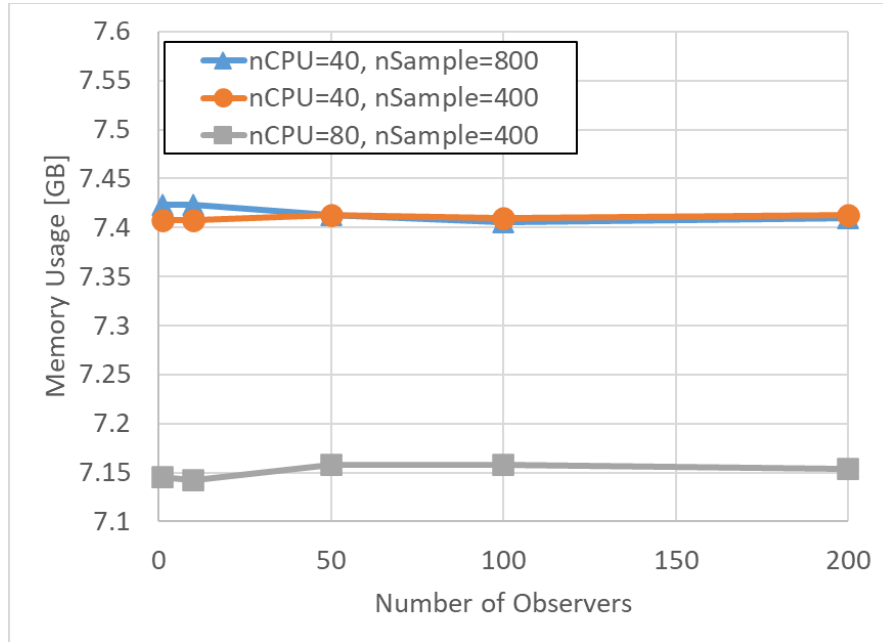


Figure 34: Number of observers versus memory usage for different CPUs and time steps.

6.3 XV-15 Tiltrotor

For further code development, the aerodynamic and the aeroacoustic fields of a propeller are considered. The XV-15 proprotor is a relatively simple yet acceptably good representative geometry, for which data are publicly available (Figure 35(a)). Although the geometric details of XV-15 rotor blades are available in the literature [88-90], the rest of the assembly, that is, the hub and the pylon components, are not available. After making a few assumptions to make up for the missing information, the CAD model and the CFD mesh were generated (Figure 35(b)).

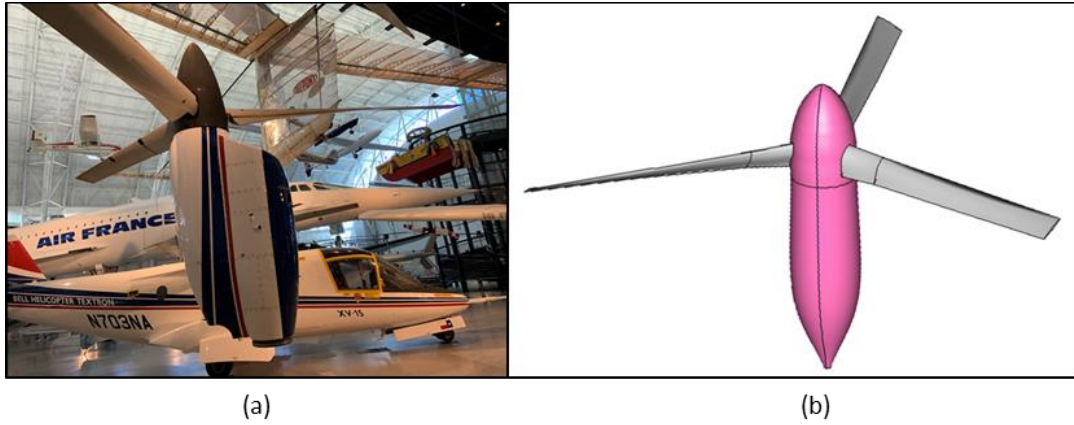


Figure 35: (a) Photo of XV-15 rotorcraft; (b) CAD model of XV-15 Rotor.

The propulsive efficiency and the thrust coefficient predicted by the SU2-URANS solver match the experimental data [89] reasonably well (Table 1). As can be observed in Figure 36, the blade-vortex interaction (BVI) does not exist since this case is in forward flight mode. Hence, the noise generation mechanisms do not include BVI [91]. The CAA computations for the XV-15 in forward flight are observed at the microphone positions shown in Figure 37(a) and Figure 37(b). The time history of the acoustic pressure signals at these microphone locations is observed, as shown in Figs. Figure 38 and Figure 39.

Table 1: Comparison of CFD and experimental data for XV-15 rotor.

	Experiment [89]	SU2-CFD
Efficiency, η	0.9319	0.8456
C_T/σ	0.0372	0.0367

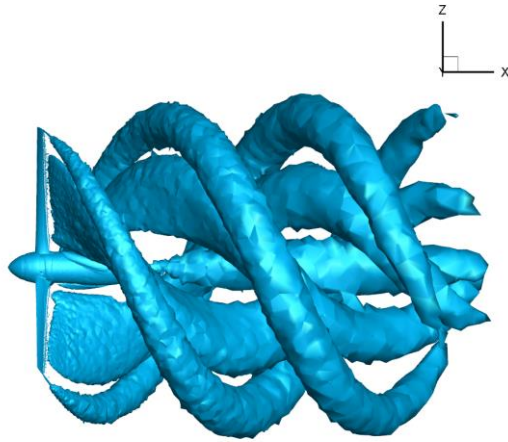


Figure 36: Instantaneous vorticity isosurfaces ($Q\text{-criterion}=2\text{ s}^{-2}$) in the XV-15 rotor wake.

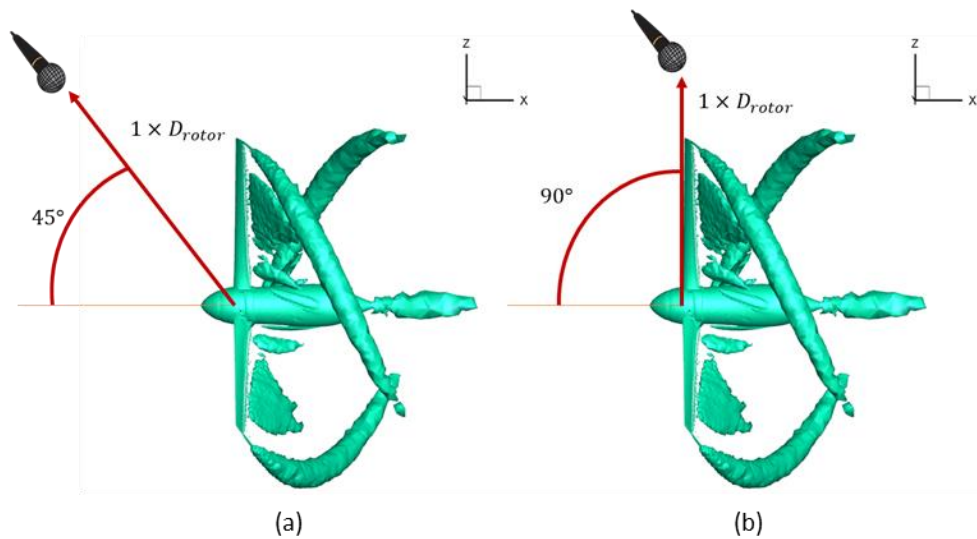


Figure 37: Rotor-oriented microphone positions, both one rotor diameter away from the tiltrotor center: (a) Mic 1 located 45 degrees above the rotor plane, and (b) Mic 2 in-plane.

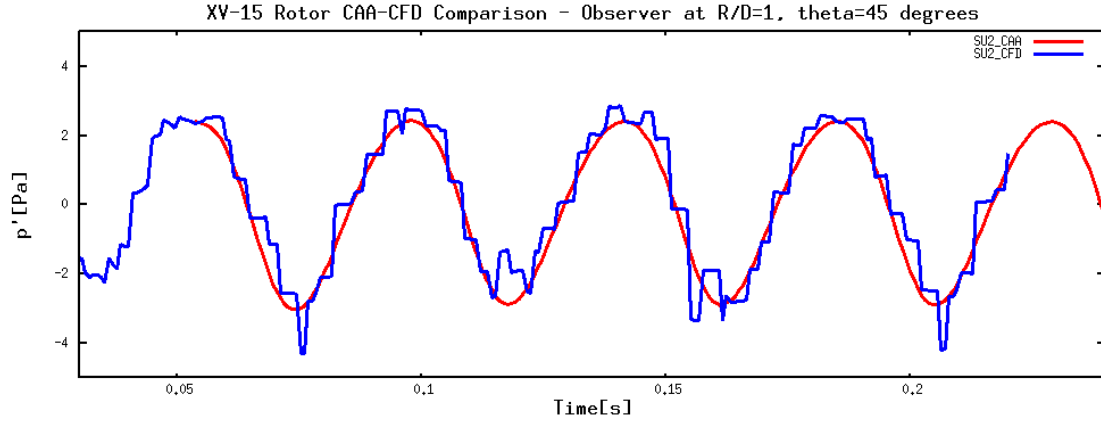


Figure 38: Comparison of CAA and CFD results for microphone 1 (45 degrees above the rotor plane).

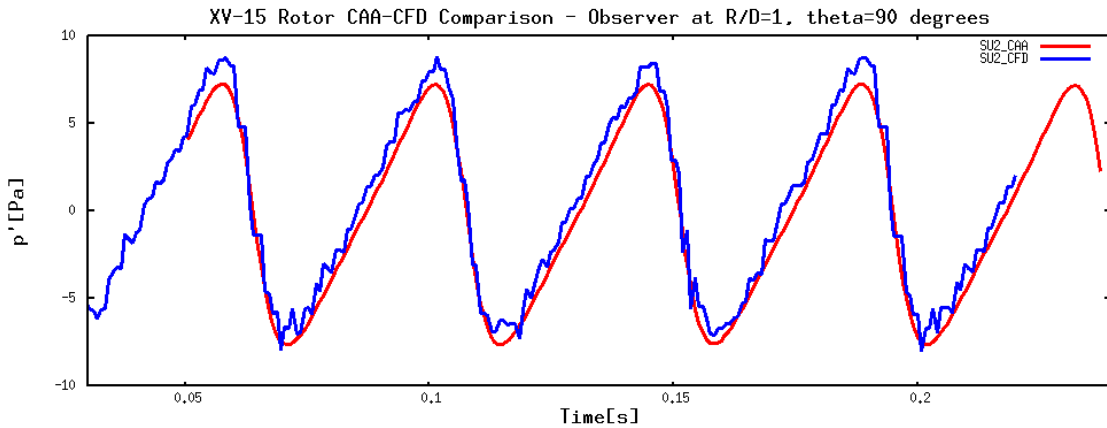


Figure 39: Comparison of CAA and CFD results for microphone 2 (in-plane position).

Comparisons of pressure fluctuations are deemed satisfactory for the tiltrotor case in forward flight. Moreover, the results demonstrate similar characteristics of a propeller described in Ref. [75]. In addition to CAA vs. CFD comparisons, benchmark studies are accomplished using ANOPP2 [86]. As seen in Figs. Figure 40-Figure 42, the acoustic pressures obtained from two different software suites (SU2-CAA vs. ANOPP2) demonstrate excellent matches. In this study, SU2-CFD produces flow data in ANOPP2-readable format and transfers it to both SU2-

CAA and ANOPP2 codes. Note that to make the symbols in Figs. Figure 40-Figure 42 easier to view, only every 4th data point is plotted.

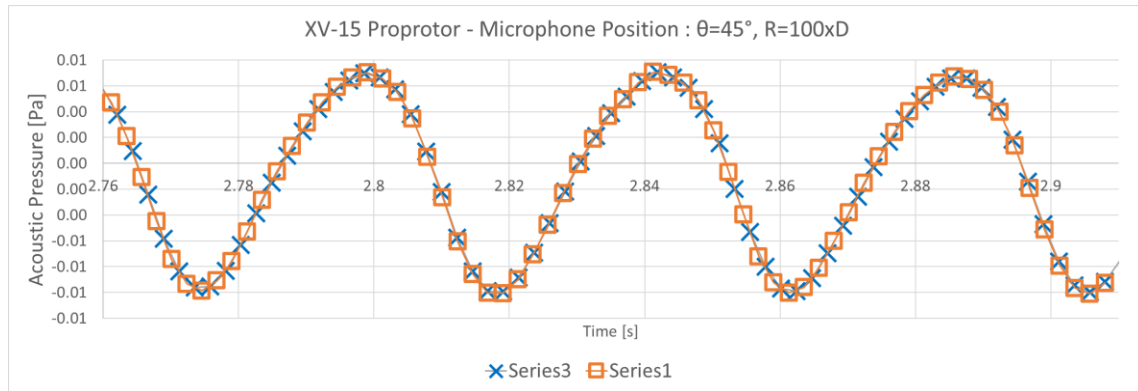


Figure 40: Acoustic pressure comparison of SU2 and ANOPP2 for the microphone located at 100 diameters away at 45 degrees above the rotor plane.

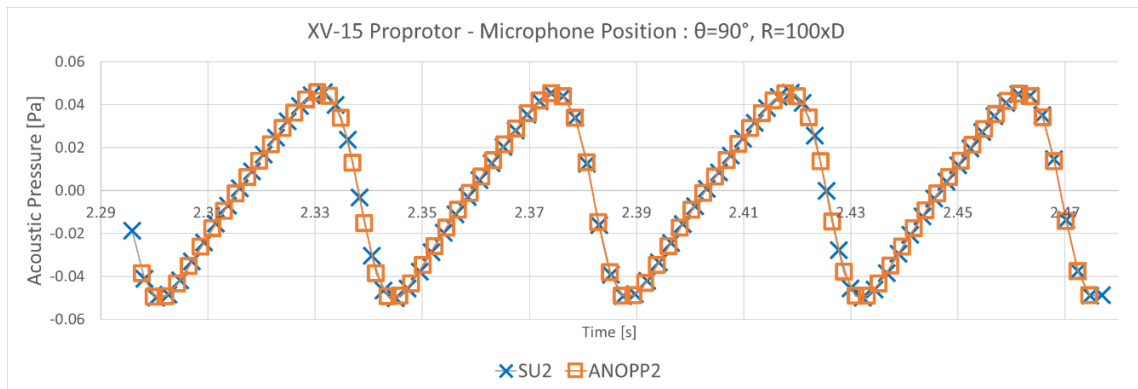


Figure 41: Acoustic pressure comparison of SU2 and ANOPP2 for the microphone located at 100 diameters away in rotor plane.

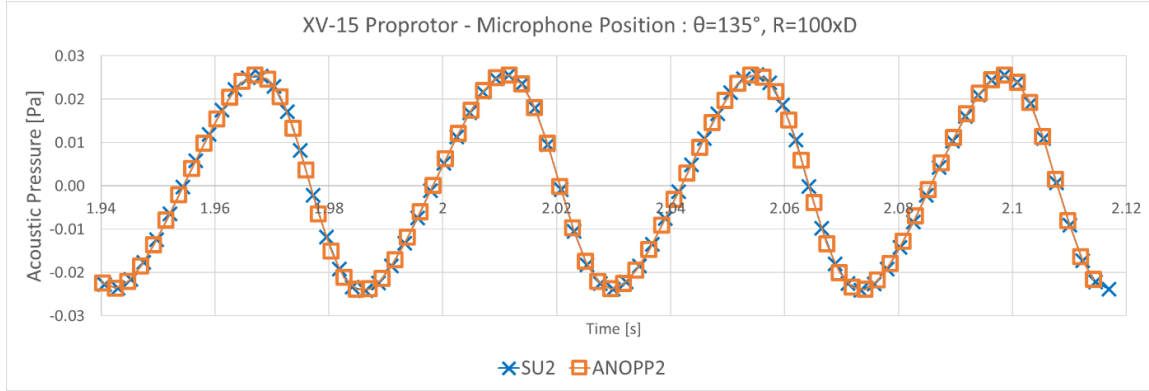


Figure 42: Acoustic pressure comparison of SU2 and ANOPP2 for the microphone located at 100 diameters away at 45 degrees below the rotor plane.

6.4 Three-bladed Helically Twisted Proprotor

The three-bladed helically twisted proprotor (3BHTP) employs an exponential function of blade twist as a function of radius to achieve uniform inflow in hover. The 3BHTP in this study is a small-sized proprotor having three blades, a hub, and a nacelle, as seen in Figure 43. The blade has a constant NACA 0012 airfoil profile from hub to tip, and it is twisted by utilizing the same chord length at each station. The chord length and the diameter of the proprotor are 1.5 in and 24 in, respectively. The distribution of the twist angle is given by,

$$\phi\left(\frac{r}{R}\right) = \text{atan} \frac{P}{\pi D \cdot \frac{r}{R}}, \quad (6.1)$$

where ϕ is the twist angle function of nondimensional radius, r/R , and P is propeller pitch, equal to 16 in.

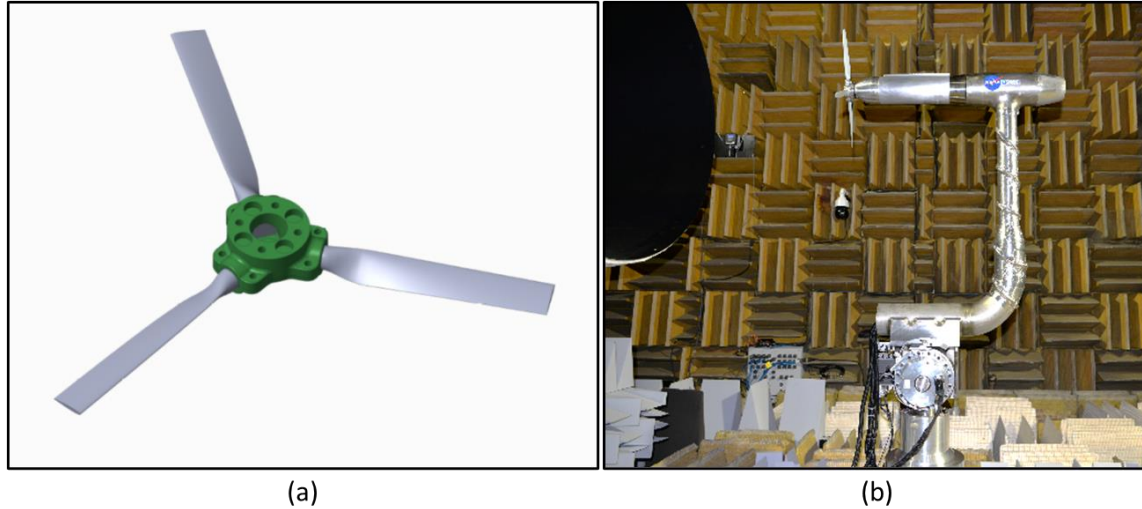


Figure 43: Three-bladed, helically twisted propeller (3BHTP): (a) CAD model and (b) wind tunnel model in LSAWT.

6.4.1 Aerodynamic Results

In the present work, the proprotor is investigated under two different flight conditions. The first is hover in a rotor configuration, where the freestream velocity equals zero. The rotational speed of the proprotor is 7,200 RPM, yielding a tip Mach number of 0.666. When it is investigated in propeller configuration, that is, for the forward flight condition, the Mach number for the freestream velocity is 0.111. The rotational speed and the tip Mach number are also slightly different; they are 7,157 RPM and 0.668, respectively. Those flow conditions are based on the data collected from NASA's Low-Speed Aeroacoustic Wind Tunnel (LSAWT). Comparisons between the thrust and torque values predicted by SU2 and those measured in LSAWT are shown in Table 2. Considering the error values, the numerical results show high fidelity for the forward flight condition.

Figure 44 shows the instantaneous vorticity isosurfaces around blades for (a) propeller configuration (forward flight condition) and (b) rotor configuration (hover condition). Also, the skin friction distribution over the blades demonstrates qualitatively the pressure gradients on the surfaces. These visuals attest to the complexity of the flow in the wakes of the blades. Hover conditions involve complex flow regimes, including flow separations. While the skin friction around the tip region for the forward flight appears smoothly distributed (Figure 44(a)), hover flight causes sharp skin friction gradients on the blade surfaces (Figure 44(b)). Therefore, the error margin between the wind tunnel and CFD may be higher for the hovering proprotor (Table 2). Overall, these predictions from SU2 show satisfactory results to be utilized later in the optimization framework.

Table 2: Comparison of CFD and wind tunnel results for three-bladed helically twisted proprotor (3BHTP).

	Forward Flight			Hover		
	LSAWT	SU2-CFD	Error%	LSAWT	SU2-CFD	Error%
Thrust [N]	115.95	113.07	2.48	262.47	269.63	2.73
Torque [Nm]	8.16	8.14	0.36	16.55	14.86	10.24

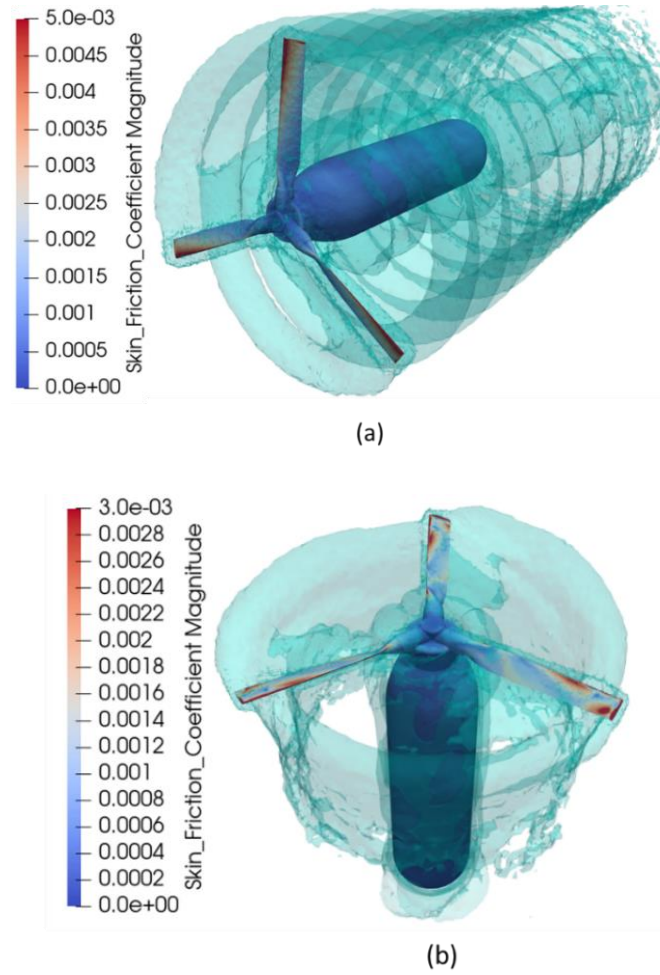


Figure 44: Instantaneous vorticity isosurfaces around propeller and skin friction distribution over the blades: (a) propeller configuration with $Q\text{-criterion}=150 \text{ s}^{-2}$; (b) rotor configuration with $Q\text{-criterion}=800 \text{ s}^{-2}$.

6.4.2 Aeroacoustic Results

As shown above in the flowcharts, after receiving data from the flow analysis, the CAA solver computes the acoustic propagation at prescribed observer locations. In Figure 45, the coordinate system is shown based on the origin point of the propeller for the microphone position. R/D , θ , and φ represent the coordinates of the observer in 3-D space.

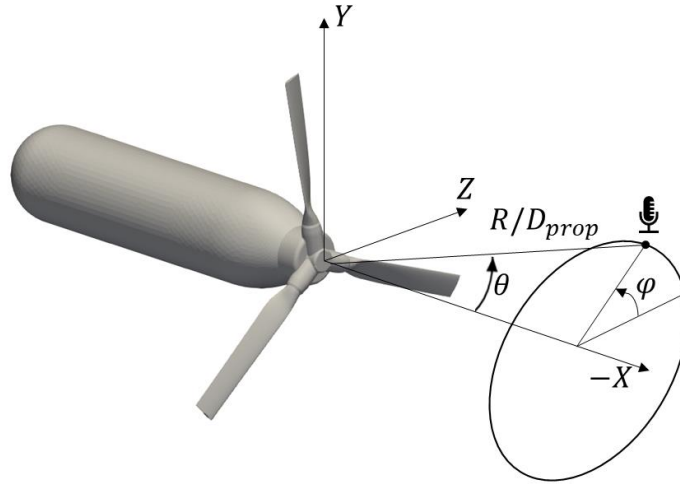


Figure 45: Coordinate system for microphone position.

As the first demonstration, an acoustic simulation is conducted for the propotor in the forward flight case. Figure 46 and Figure 47 show the time history of acoustic pressure attained from SU2-CAA and LSAWT for a randomly selected pair of observers. Here, one observer is placed 10.5 propotor diameters away with described θ and φ angles, which are set as 114.6 and 40, respectively. For the second observer, those numbers are 9.5, 94.6, and 40, respectively. The obtained data show the noise propagation generated only by the propotor blades and hub. The predicted results and the wind tunnel results show reasonable agreement. Although not shown here, comparisons were made for many other observers, and the selected figures here are indicative of those comparisons.

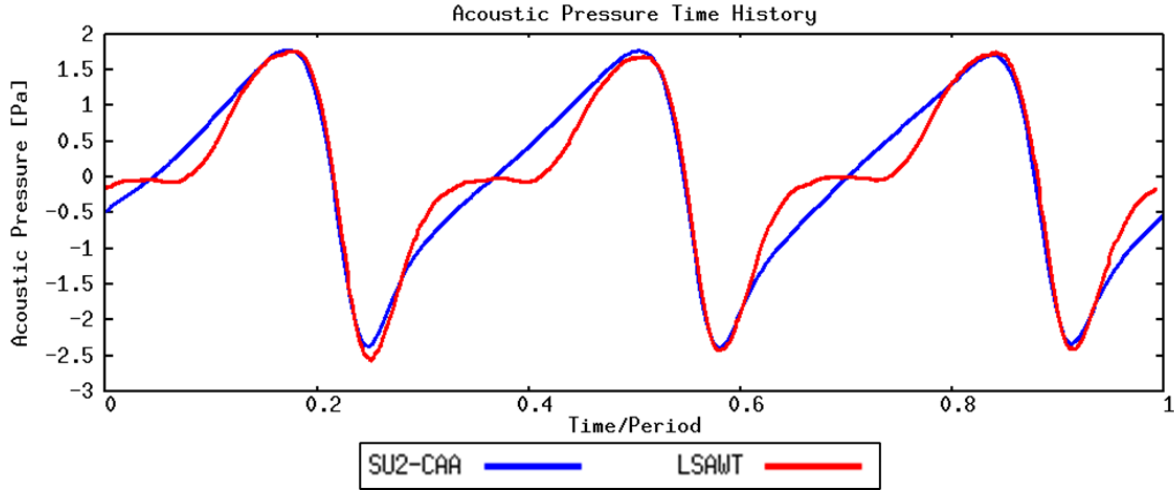


Figure 46: Time history of acoustic pressure for an observer, located at $R/D=10.5$, $\theta=114.6^\circ$, and $\phi=40^\circ$ (observer-14).

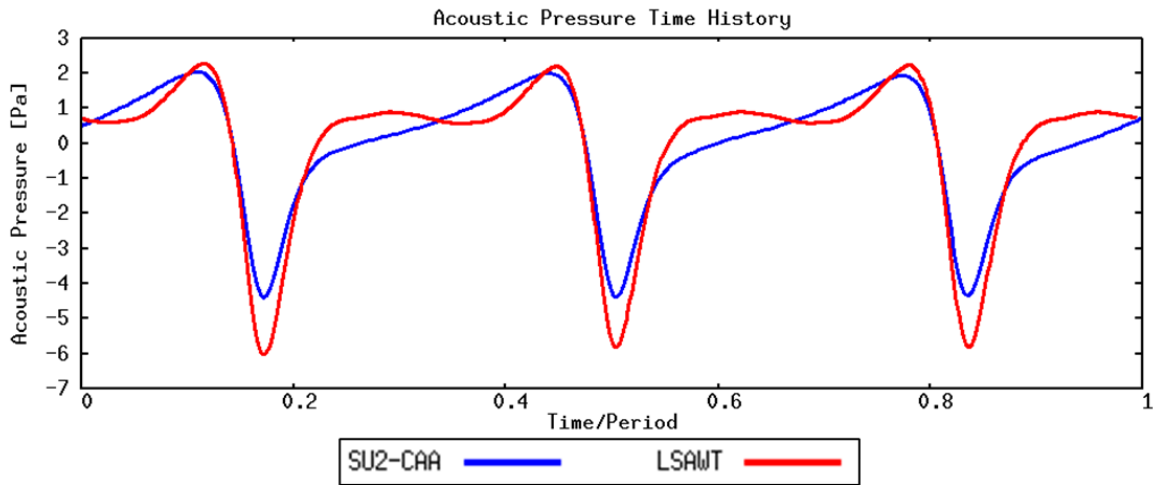


Figure 47: Time history of acoustic pressure for an observer, located at $R/D=9.5$, $\theta=94.6^\circ$, and $\phi=40^\circ$ (observer-10).

The present CAA tool can convert acoustic pressure data from the time domain to the frequency domain by utilizing a discrete Fourier transform. Thus, the sound pressure level (SPL) versus frequency data are obtained as described in Ref. [76]. For the SPL calculations, the reference pressure is taken as 2×10^{-5} Pa. The highest SPL value corresponds to the

fundamental blade passage frequency (BPF), which is 360 Hz. In addition to the time domain comparison, the spectral comparison is performed to show the fidelity of predictions, as seen in Figure 48. The data in both the time and the frequency domains confirm that the simulations are close to the experimental data, and it is reasonable to continue this work with SU2-CAA predictions.

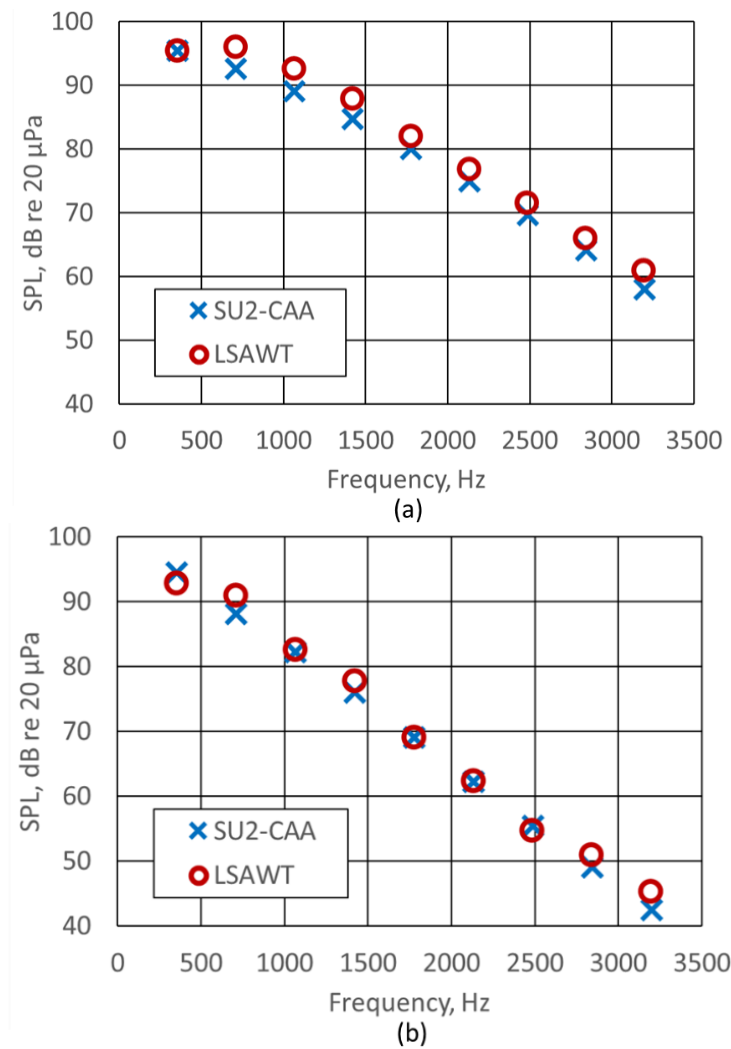


Figure 48: Spectral comparison of SU2-CAA predictions and LSAWT data for: (a) observer-10 and (b) observer-14.

The verification studies continue with investigating another comparison showing the sound pressure level (SPL) values perceived by a described microphone pattern. In this research, 27 microphones were positioned from upstream to the downstream region by keeping a constant distance in the y and z direction according to the propotor origin. Both in the CAA and wind tunnel tests, the same microphone patterns were utilized.

The design evaluation must involve a complete assessment of the aeroacoustic performance of the propeller and the rotor by using multiple observer points. Figure 49(a) and Figure 49(b) show SPL values for different θ angles for forward flight and hover conditions, respectively. In the plots, SPLs corresponding to 3 different blade passage frequencies (BPF) are compared. The marked curves represent wind tunnel results, and the straight lines come from the CAA analyses. The results are quite satisfactory for both forward flight and hover for fundamental frequency (1xBPF). However, the graphs indicate that the prediction-based data have lower SPLs for the harmonics (2x and 3x BPF), particularly for the microphone located near the in-plane direction, the angles between 75° and 105° . That discrepancy may be the result of limitations in geometric accuracy, numerical methods, and the identified flow conditions. Overall, the CAA tool is verified by the wind tunnel test, and it has a high confidence level to be utilized in the optimization process.

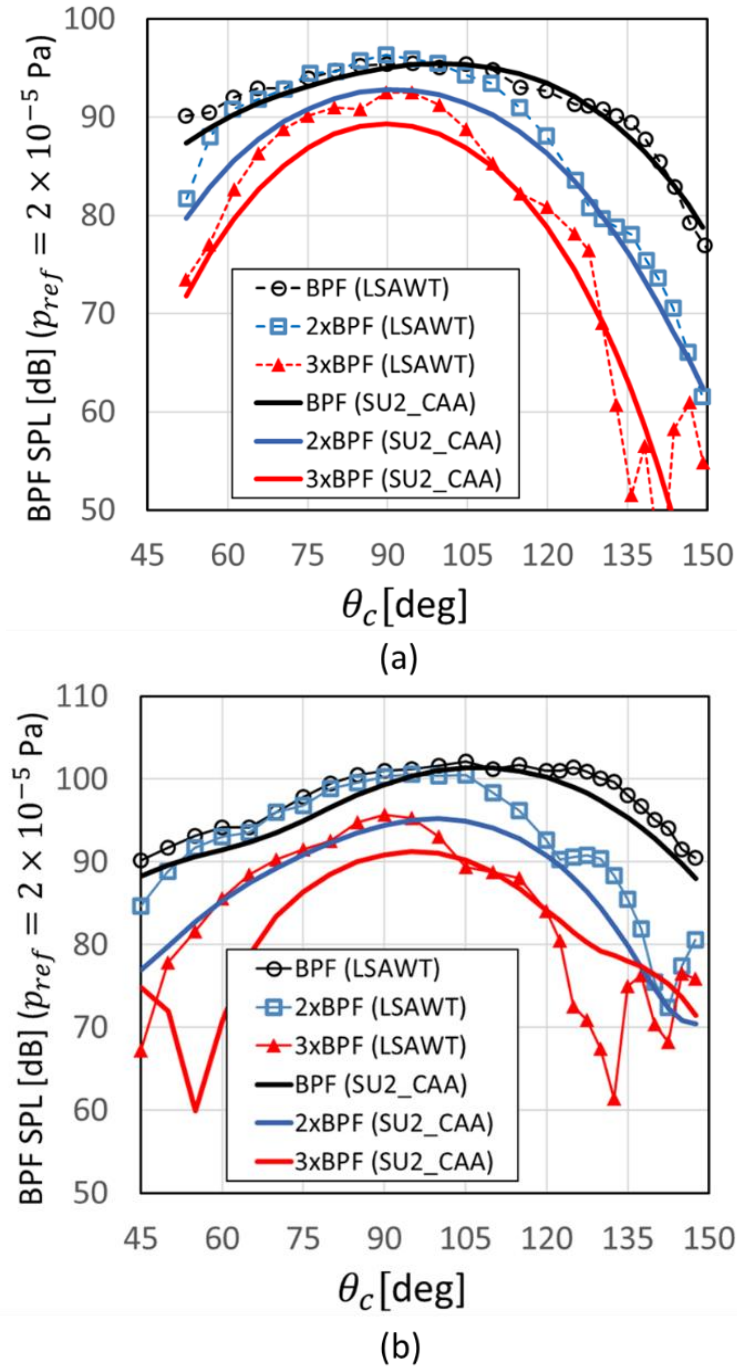


Figure 49: Sound pressure values corresponding to fundamental blade passage frequency versus observer locations at different θ angles (with constant $x/D_{prop} = 3.73$ and $y/D_{prop}=4.45$) for: (a) forward flight, and (b) hover conditions.

6.5 Workshop for Integrated Propeller Prediction (WIPP)

The Workshop for Integrated Propeller Prediction (WIPP) produced an aerodynamic reference study in 2019 [92] to provide more guidance to researchers and developers studying propeller geometries. Targets of the workshop were: (1) presenting publicly available experimental data for verification studies, (2) demonstrating a detailed wake profile for a propeller, and (3) producing data based on propeller-wing interactions. The experiments were held in the Lockheed Martin Low-Speed Wind Tunnel.

The WIPP assembly consists of a propeller, a nacelle, and a wing. The propeller is a 10% scale of C-130, and its diameter is 16.2 inches. The propeller and nacelle assembly are mounted to the wingtip. The wing is a 40.5%- scaled semi-span model of the X-57 experimental NASA aircraft. The aspect ratio and the taper ratio of the wing are 6.7 and 0.7, respectively. The WIPP model is mounted vertically to the wind tunnel floor, and it stands vertically, as seen in Figure 50(a). The distance between the tunnel floor and the wing tip is 67.065 inches (which is the wingspan). The propeller has four blades and a cone-shaped hub. The thickness and the pitch angle of the blade sections decrease from hub to tip leading to a significant sharp edge at the trailing edge.

By utilizing various flow conditions, the aerodynamic performance of the model is investigated. For different flow regimes, the rotational speed of the propeller is altered. Mach numbers are 0.04, 0.08, and 0.11, and the thrust coefficient varies between 0.0 and 0.4. The angle of attack is also a switchable parameter throughout the tests.

As the output, a number of surveys are provided in Ref. [92]. From the pressure surveys on the wing and in the wake of the propeller, a significant amount of data is available to compare computational models with the wind tunnel measurements.

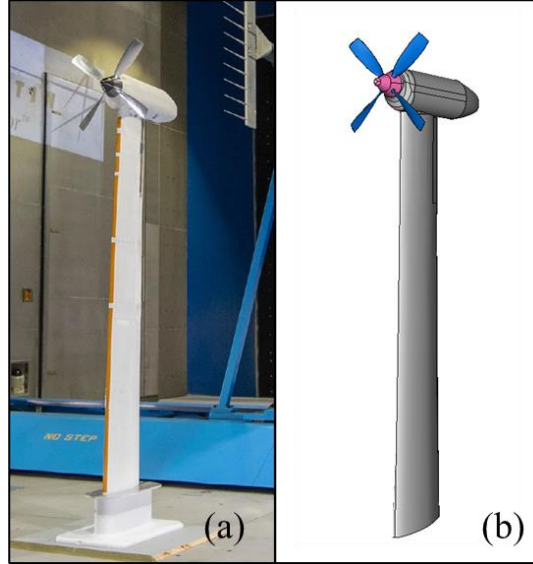


Figure 50: (a) Wind tunnel model from WIPP; (b) CAD/CFD model.

To develop a computational model, some assumptions have been made whenever geometrical information is not found in the Workshop documents. Also, some modifications are needed, such as to close the small gaps between the components. Finally, the pedestal that the wing sits on has been neglected for simplicity.

One of the challenges is to develop a computational mesh that accommodates the rotation of the propeller and the hub near the non-rotating surfaces of the wing and nacelle. This relative motion is represented by the developed multizonal domain decomposition (Figure 51). Zone-0 mesh rotates with the rotating parts, which are the blades and the hub. Zone-1 is the stationary domain which includes the nacelle and the wing. The information transfer across the zonal interfaces is made by a conservative sliding mesh algorithm [93]. The diameter of Zone-0 is 1.5 times the propeller diameter. The computational domain's length, width, and height are 20, 20, and 10 times the propeller diameter, respectively.

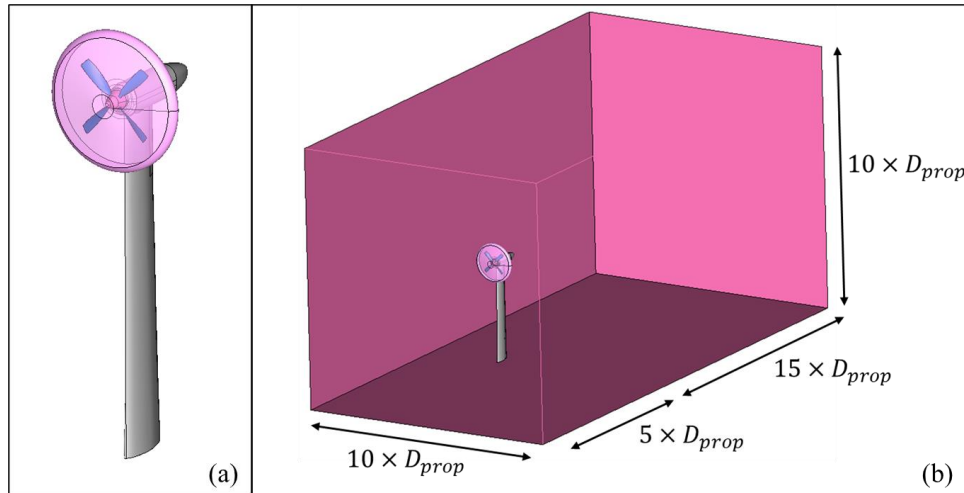


Figure 51: (a) Moving (relative to the stationary) mesh for the rotating hub and the propeller and (b) Computational domain; dimensions normalized by propeller diameter (D).

6.5.1 Aerodynamic Results

To verify the propeller aerodynamics results, they are compared with the experimental data from Ref. [92, 94, 95]. Basically, the WIPP model is a scaled C-130 propeller, and it has a 4-bladed propeller, each with its hub and nacelle mounted on a wingtip. The experiments conducted in a wind tunnel produced a significant amount of data. Reported in Ref. [92], the experimental data and the CFD results were submitted by a few of the workshop attendees. Different teams have used different CFD solvers to check their codes.

The configuration, which has a thrust coefficient of 0.4 at zero angle of attack when subjected to flow at Mach number 0.11, is chosen for the comparisons. Presented in Figure 52 is the entire assembly used in the WIPP testing. It shows pressure coefficient distributions (a) and the time history of the drag coefficient (b). It is noted that the simulations converged to the limit cycle.

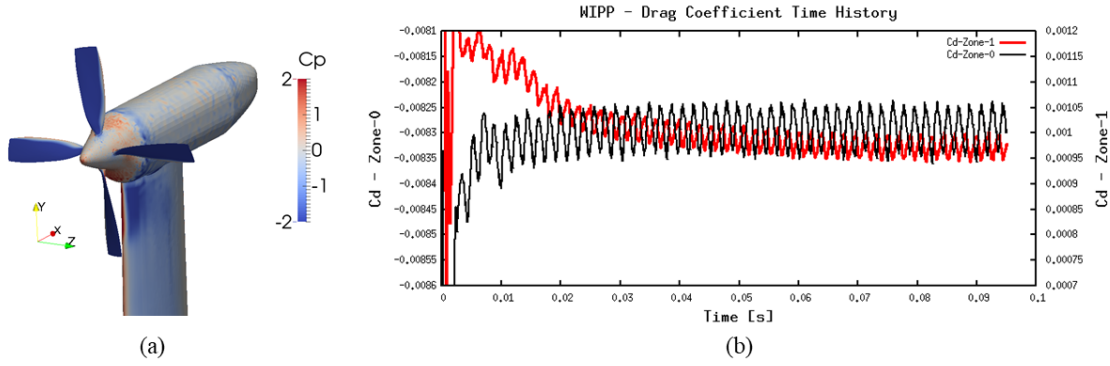


Figure 52: (a) Pressure coefficient distribution over wing mounted propeller, WIPP, and (b) drag coefficient time history of CFD analysis.

In CFD, the mesh density affects the accuracy of the result obtained from the simulations. Therefore, showing the effect of increasing the mesh nodes provides information about the solution's precision and accuracy. Presented in Table 3 are comparisons with three different mesh resolutions of the WIPP assembly and data, and a case of an isolated propeller. As expected, the highest density grid, G3, provides relatively the best results. Also, modeling the full assembly with all its components produces higher fidelity results in comparison to the isolated propeller case.

Table 3: Number of nodes and percentage of thrust error of the CFD simulations with different grid densities.

	Number of Nodes	%Error in Thrust
Isolated Propeller	4.52M	11.63
Full Assembly – Grid-1	4.97M	5.42
Full Assembly – Grid-2	5.51M	4.83
Full Assembly – Grid-3	6.37M	4.15

The present computational results capture the characteristics of the wake region. Deployed in the experiments are probes that measure the magnitude of the velocities at different stations along the wake. Some of the probe locations are shown in Figure 53. There are four different probe locations chosen in the wake region by varying the x coordinate (flow direction) and the z coordinate.

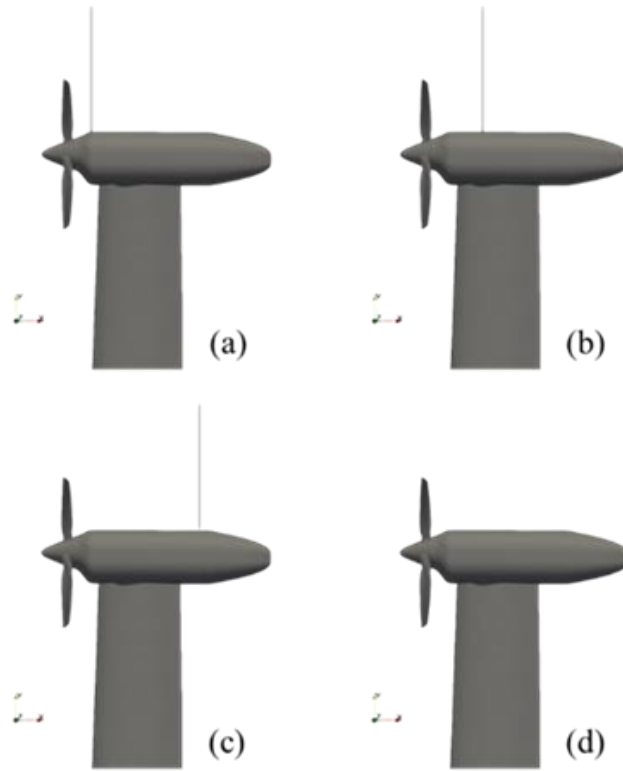


Figure 53: Probe line locations corresponding to WIPP geometry: (a) $x=1.5$ in; (b) $x=5$ in; (c) $x=13$ in; and (d) $x=21$ in.

The wake surveys measure the axial velocity distribution along the probe line for both the full assembly and the isolated propeller cases. In Figure 54, plots provide the comparison of the wind tunnel data and the present CFD simulation in terms of nondimensional axial velocity along

the radial direction. The simulation with full assembly on Grid-3 provides the best-predicted values.

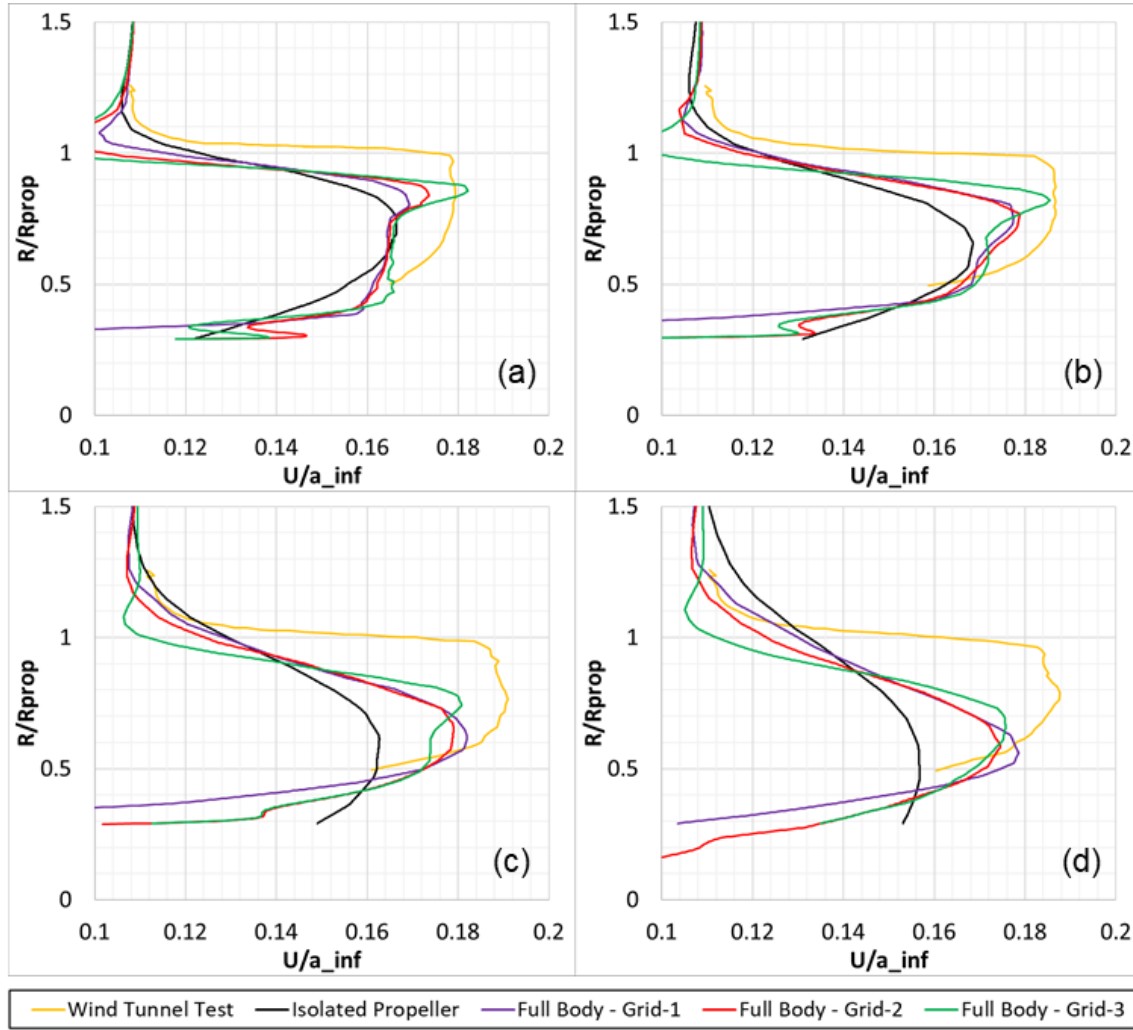


Figure 54: Nondimensional axial velocity, U/a_{∞} , distributions along the wake line on successively finer grids located at: (a) $x=1.5$ in., (b) $x=5$ in., (c) $x=13$ in., and (d) $x=21$ in.

Presented in Figure 55 are the swirl velocity distributions. The simulation on Grid-3 provides the best predictions. Therefore, aeroacoustic computations (shown later) use the CFD results from the simulation on Grid-3.

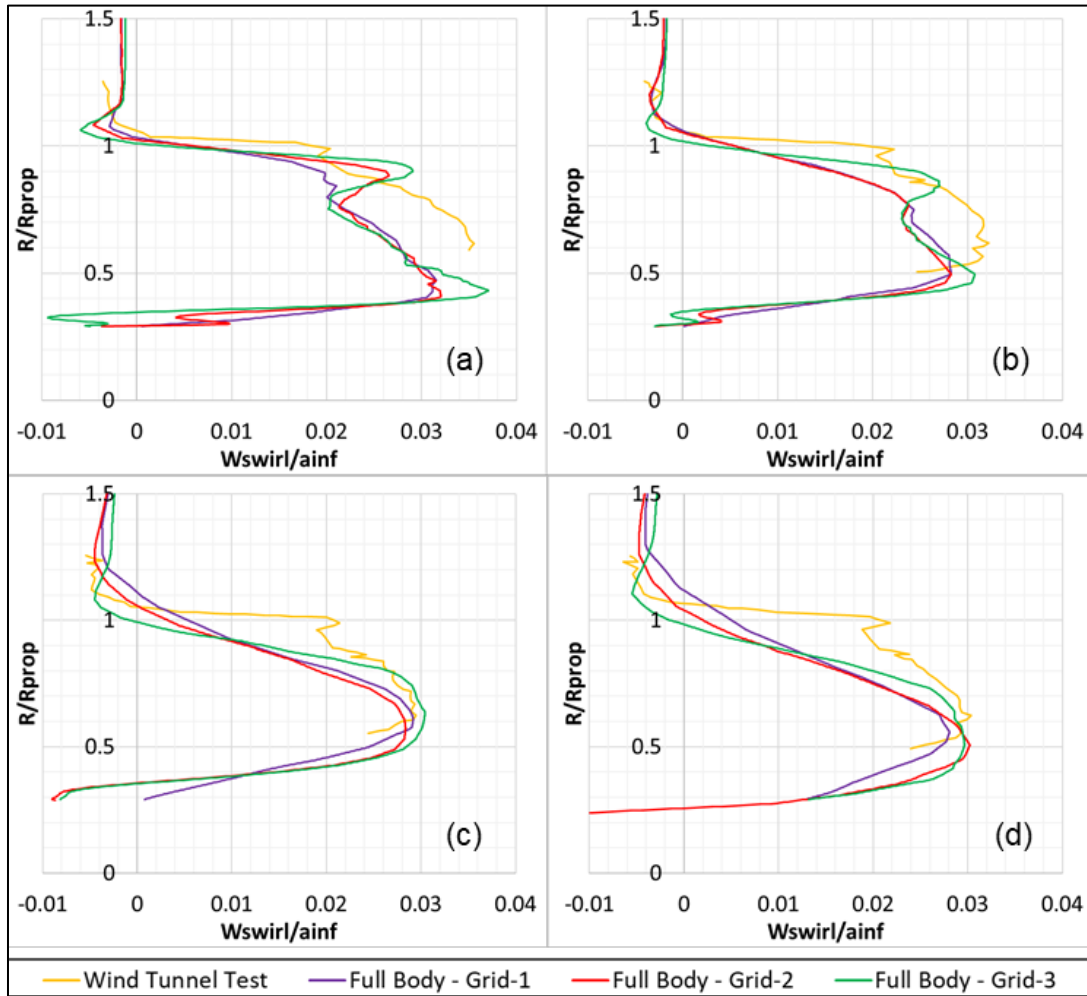


Figure 55: Nondimensional swirl velocity, W/a_{∞} , distributions along the wake located at (a) $x=1.5$ in., (b) $x=5$ in., (c) $x=13$ in., and (d) $x=21$ in., on successively finer grids.

6.5.2 Aeroacoustic Results

After receiving data for the flow analysis, the present CAA solver computes the acoustic propagation to the prescribed observer locations. In Figure 56, the coordinate system is shown based on the origin point of the propeller for the microphone position. R/D , θ and φ represent the coordinates of the observer in 3-D space.

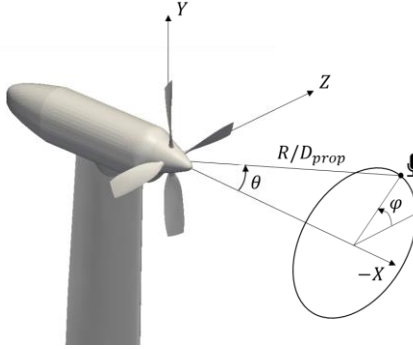


Figure 56: Coordinate system for microphone position.

First, acoustic simulations are conducted for the WIPP cases with a single observer placed at 100 diameters away in the in-plane direction, and the obtained time history is presented in Figure 57. Also superimposed are the isolated propeller case, the noise contribution from Grid Zone-0 (the propeller and the hub), and the noise contribution from Grid Zone-1 (the wing and the nacelle).

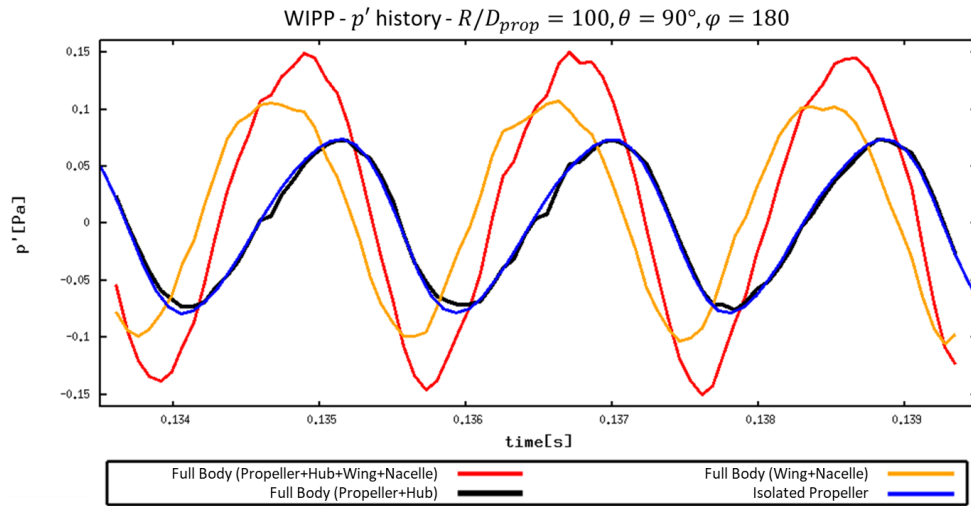


Figure 57: Time history of acoustic pressure for an observer, x: $R/D=100$, $\theta=90^\circ$ and $\phi=180^\circ$.

Observed in Figure 57, the acoustic pressure from the isolated propeller (blue) and the rotating parts, that is, the propeller and the hub (black), are close to each other. Thus, it can be discerned that for the specified observer point in this case the presence of the wing geometry does not significantly affect the noise emitted from the propeller.

The non-rotating parts, that is the wing and the nacelle (orange), generate more noise than the rotating parts (propeller and hub in black). The noise level of the full assembly configuration is higher in comparison with the isolated propeller.

However, when the observer moves to a different location (Figure 58), a different outcome is observed. Again, the isolated propeller propagated noise (blue) and the propeller and the hub case (black) show similar trends. In contrast, propeller and hub sourced propagation (black) obtained from a full assembly configuration has a higher acoustic pressure magnitude than the isolated propeller (blue). This outcome may be explained by the effects of wing and nacelle geometry on the propeller-based noise propagation.

A remarkable point is that the overall noise level obtained from the full assembly (red) is less than the isolated propeller-generated noise (blue). The reason for that occurrence may be the phase difference between the acoustic signals emitted from the wing and propeller. The time domain-based graphs support this distinctly.

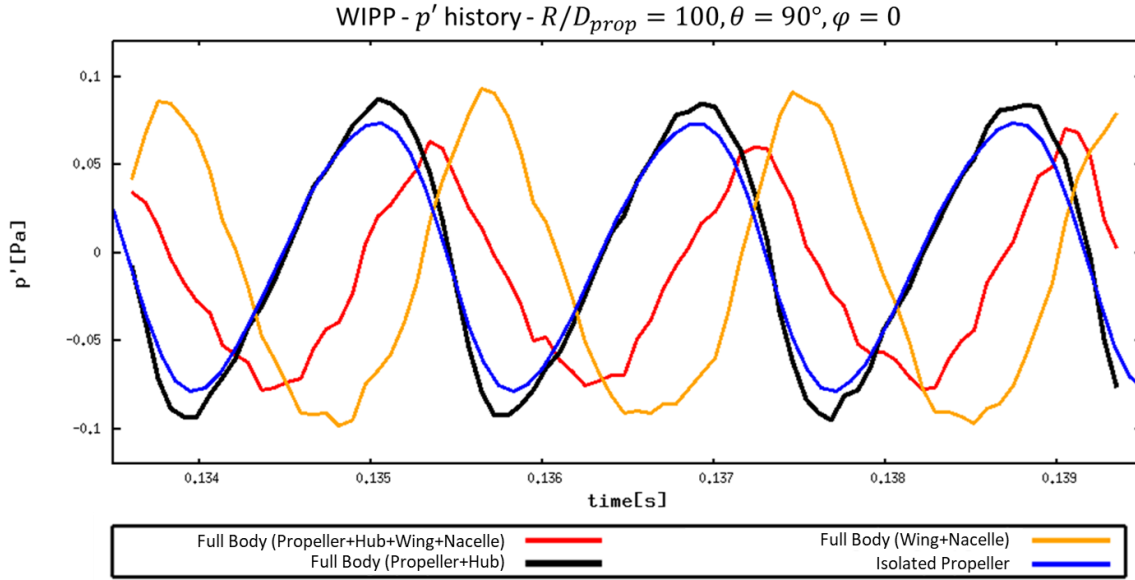


Figure 58 : Time history of acoustic pressure for an observer, x ($R/D=100$, $\theta=90^\circ$ and $\varphi=0^\circ$).

The developed SU2-CAA code can extract needed information from the SU2-CFD output which is readable by the postprocessor used here (ParaView). Both sigma surfaces and the actual surfaces can be utilized to show the acoustic pressure distribution. The propeller's wake creates pressure waves on these surfaces (Figure 59). It can be concluded that the wing tip region is impacted the most by the wake. That also affects the noise emitted from the wing itself.

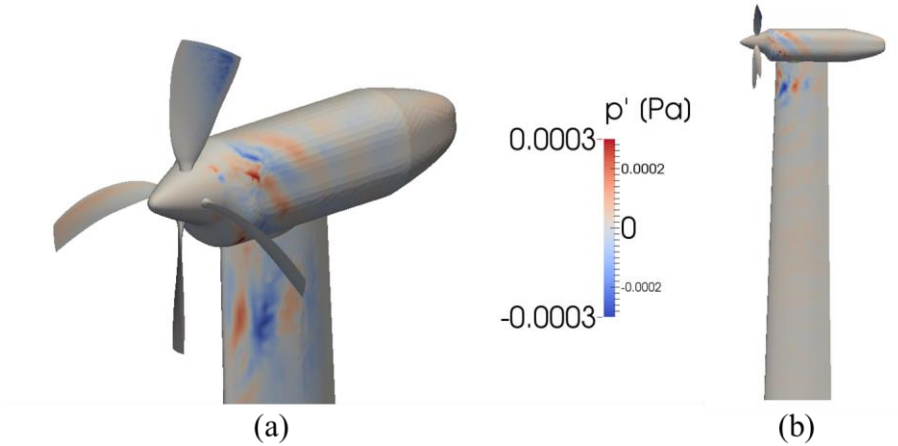


Figure 59: (a) p' distribution over sigma surface of propeller blades and nacelle, (b) Acoustic footprints on full-body WIPP geometry.

To show the interaction between the propeller and the wing, two different microphone array patterns are utilized. One of the patterns is located 100 diameters away from the bottom side of the assembly, and the other pattern is 100 diameters away from the top side. In total, 19 microphones (observers) are located between the theta angles of -45 deg and -135 deg (Figure 60(a)) and +45 to +135 deg (Figure 60(b)). There is a 5-degree gap between the microphones.

Shown in Figure 61 are the SPL values for the blade-passing frequency (BPF) at different θ angles. The θ angle varies between -45-deg and -135-deg with keeping the distance in the z-direction constant. That is, the sweeping occurs from upstream to downstream with the same θ increment. The noise emitted from the propeller and the hub (blue) is close to the SPL values from the isolated propeller (orange). Although the isolated propeller curve shows slightly different characteristics through the upstream region, almost the same SPL values are predicted after -80-deg.

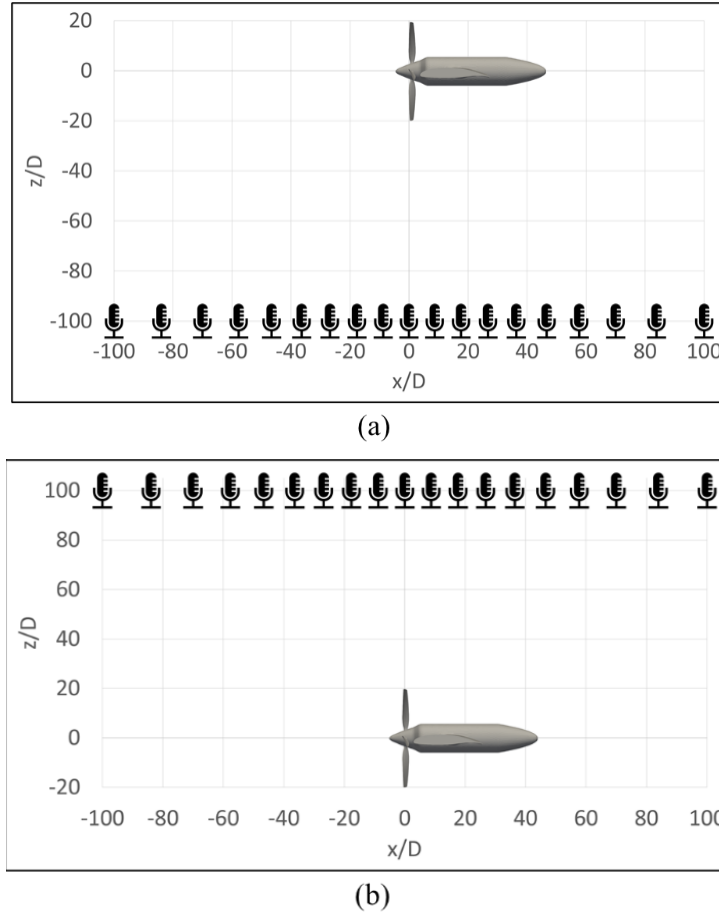


Figure 60: Demonstration of the microphone (observer) positions relative to center of the propeller at 100-diameter away in (a) negative and (b) positive z -direction with different x/D distances.

The computations for the full assembly, including all the components, have the highest SPL values along the in-plane direction (black). It is partially due to the contributions of the wing and the nacelle (red). After -120-deg and through downstream, the overall noise level is even lower than the propeller-only and wing-only emitted noise. This may suggest that the interaction between the parts may also reduce the overall noise.

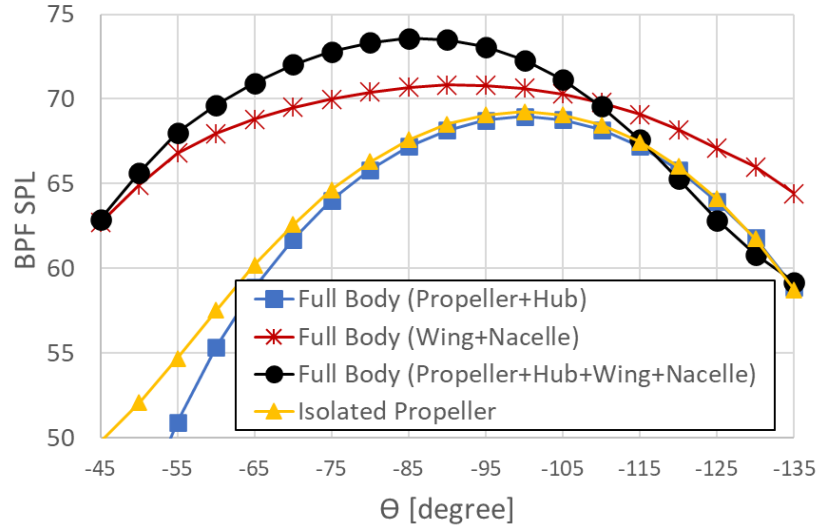


Figure 61: Theta vs. BPF SPL for full body and isolated propeller configurations for the observer points located between (-45)-(-135) degrees at the 100-diameter away in the negative z-direction.

The next set of results are from the computations for the microphones shown in Figure 60(b). As in the previous set of results, BPF SPL values obtained from different noise sources are presented in Figure 62. In this section, θ angle takes the value between 45-deg and 135-deg at 5 deg intervals. Unlike with the microphone array shown in Figure 60(a), the isolated propeller case (orange) has lower values than the assembly including only the rotating parts (blue). This may be explained by the inclusion of the non-rotating components.

A remarkable observation is that the full assembly, including every component (black), has the lowest noise level at 75-deg. While the rotating and non-rotating components emit noise levels larger than 65 dB, the overall noise level is 60.6 dB. Between 45-deg and 95-deg, the overall noise level is lower than partial contributions coming from the individual components. However, after 115 deg, the overall noise level increases in the downstream region.

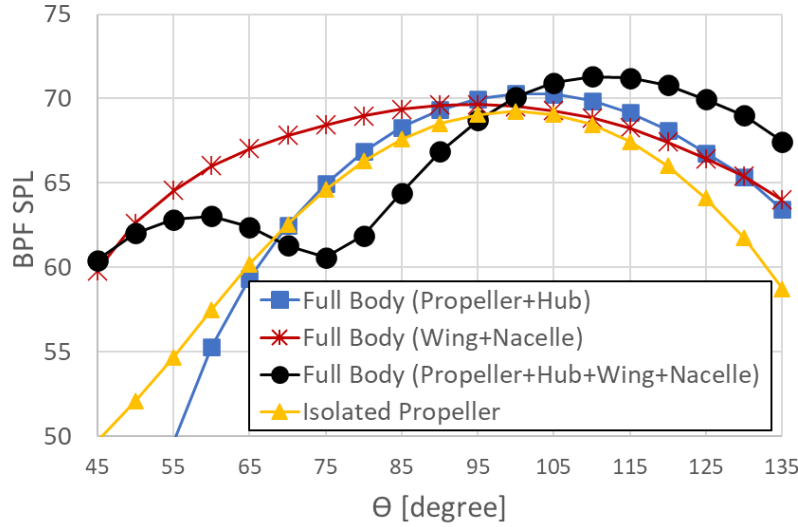


Figure 62: Theta vs BPF SPL for full body and isolated propeller configurations for the observer points located between 45-135 degrees at the 100-diameter away in positive z-direction.

6.6 Four-bladed Ideally Twisted Rotor/Propeller

In this section, the flow and the acoustic analyses are conducted for a four-bladed rotor geometry called “four-bladed ideally twisted rotor (4BITR),” which is described in Ref. [96]. Pettingill et al. [96] report on a wind tunnel setup for the aeroacoustic measurements of this four-bladed rotor (4BITR). The present computations are for the same geometry and the flow conditions to predict the tonal noise.

Zawodny et al. [97] demonstrate aeroacoustic measurements for the wing-stowed propeller. The performed wind tunnel measurements involve various positions of the wing relative to the propeller. Additionally, different angles of attack and their impacts are studied. The results (plots of theta angle versus blade-passing-frequency-based sound pressure levels) show the impact of the wing position on the overall sound pressure level. It is stated that the

distance between propeller and wing affects the sound pressure level drastically at some microphone positions.

The objective of conducting simulations for 4BITR is to report on the extension of the SU2 adjoint framework to compute on *multizonal* and *dynamic* meshes. This capability enables the analysis and sensitivity of the aeroacoustics associated with the installed rotors. The zone that is fixed on the rotor moves with the blades relative to a stationary global mesh, which is for the stationary components of the vehicle or tunnel test stand.

4BITR employs an exponential function of blade twist as a function of radius to achieve uniform inflow in hover. The 4BITR in this study is a small-sized rotor having four blades, a hub, and a sting. The blade has a constant NACA 0012 airfoil from hub to tip, and it is twisted by utilizing the same chord length at each station. The chord length and the diameter of the rotor are 1.25 in. and 12.5 in., respectively.

In this dissertation, the rotor is in hover; therefore, the freestream velocity equals zero. The rotational speed of the rotor is 5,500 RPM, the tip Mach number is 0.27. Figure 63 shows (a) the instantaneous pressure distribution over the wing-rotor and (b) the time history of the drag coefficient. It should be noted that the simulations are converged to the limit cycle for the given geometry and the flow conditions.

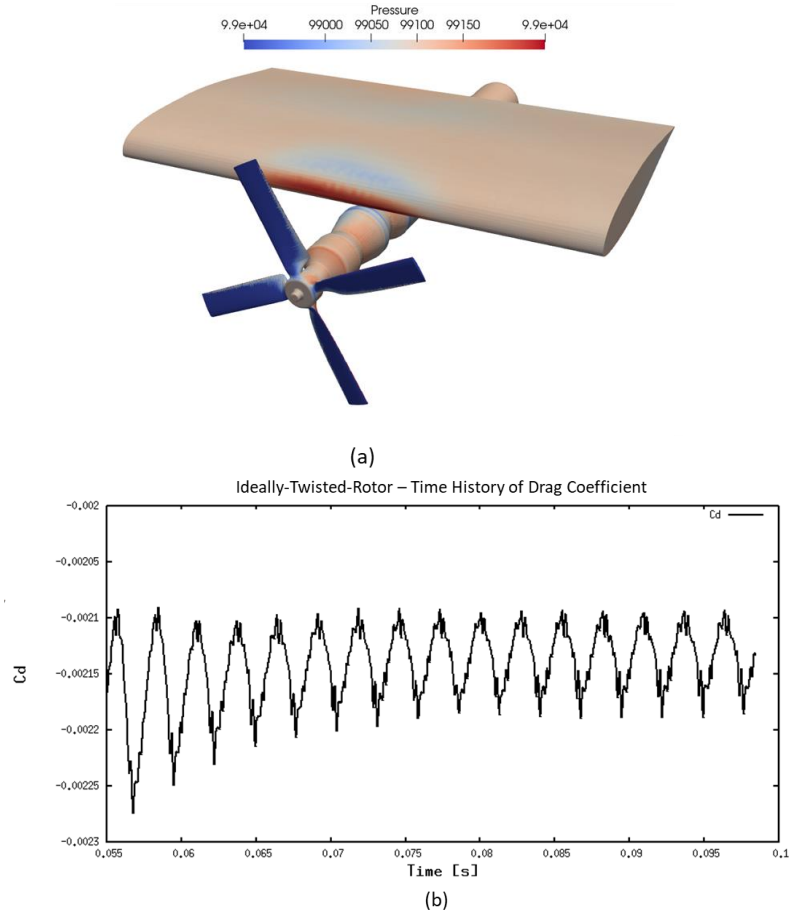


Figure 63: (a) Instantaneous pressure distribution over wing and ideally-twisted-rotor, 4BITR, and (b) drag coefficient time history of CFD analysis.

6.6.1 Aeroacoustic Results

After receiving data from the flow analysis, the CAA solver computes the acoustic propagation at prescribed observer locations. Shown in Figure 64 are the Cartesian coordinates for the microphone, which has its origin at the rotor center. The observer location in 3-D space is defined by the spherical coordinates R/D , θ , and φ .

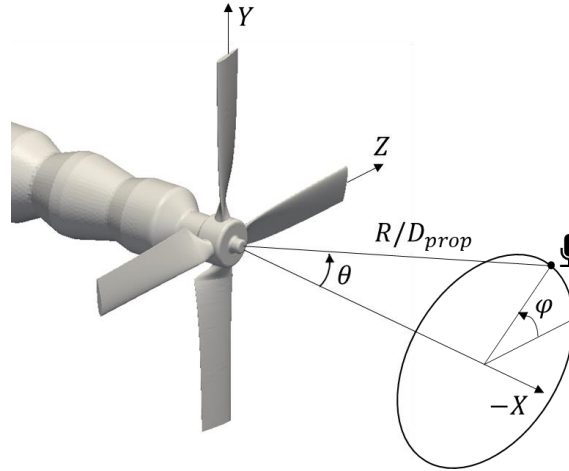


Figure 64: Coordinate system for microphone position.

As the first demonstration, an acoustic simulation is conducted for an isolated rotor case. In Figure 65, the time history of acoustic pressure is shown. Here, the observer is placed at 10 diameters away in the plane of the rotor. The data obtained show the noise propagation generated only by the rotor blades.

A complete assessment of the aeroacoustic performance of the rotor must be evaluated by using multiple observer points. Figure 66 shows SPL values for different θ angles but keeping the distance in z-direction constant. For the SPL calculations, reference pressure is taken as 2×10^{-5} Pa. The highest SPL value corresponds to the fundamental blade passage frequency (BPF) and equals 367 Hz. BPF-SPL values differ from 40 dB to 53 dB, from upstream to downstream. results in the figure are for the isolated propeller only.

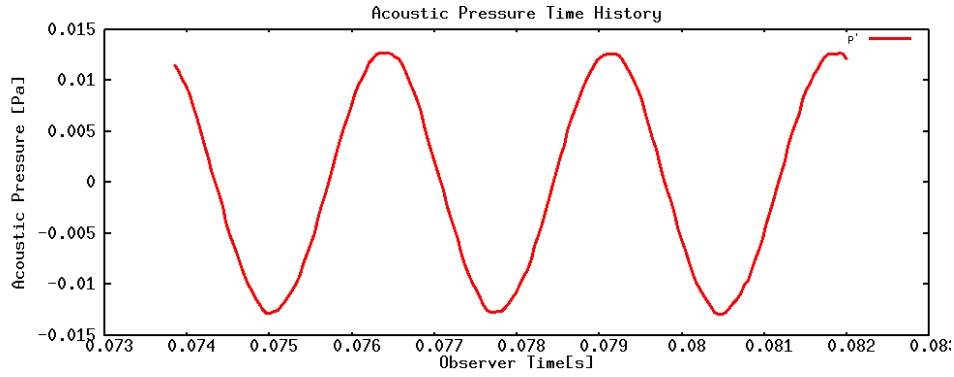


Figure 65: Time history of acoustic pressure for an observer, x ($R/D=10$, $\theta=90^\circ$ and $\phi=90^\circ$).

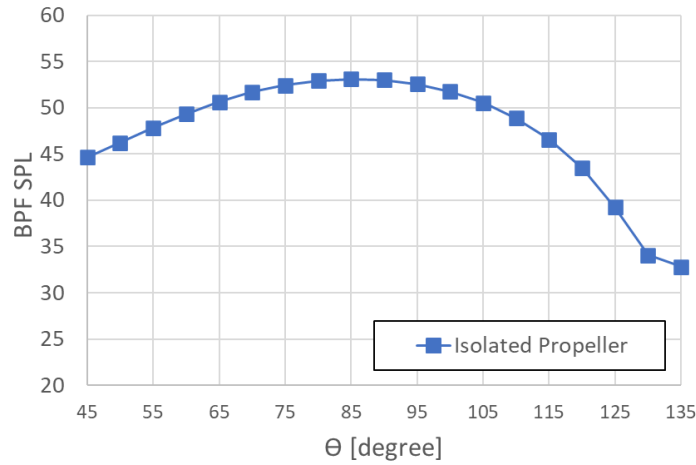


Figure 66: Sound pressure values corresponding to fundamental blade passage frequency vs. observer locations at different θ angles (with constant $y/D_{prop} = 10$ and $\phi = 90^\circ$).

In addition to the isolated propeller, the simulations are conducted for the configuration, including wing, sting, and propeller. The wing is located above and behind the propeller, relatively. Due to the wake flow of the propeller, the wing is exposed to an excitation. In parallel with the conventional flow interactions, propeller and wing affect each other actively. Figure 67 demonstrates how propeller wake impacts the acoustic pressure distribution over the wing surface.

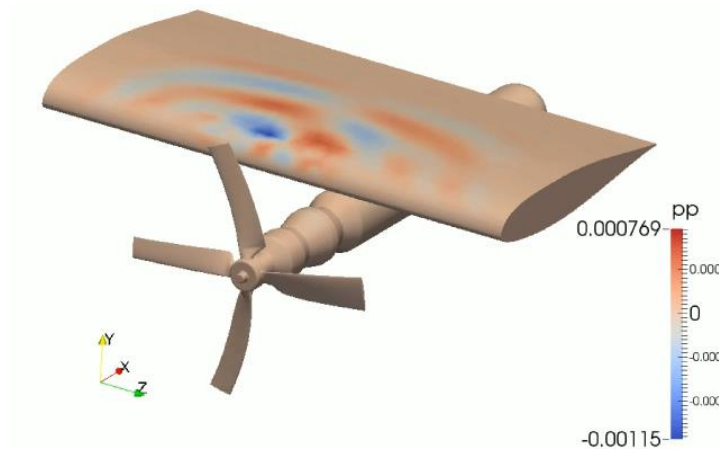


Figure 67: Instantaneous pressure fluctuation on the wing surface due to the excitation by propeller wake flow.

Quantitative demonstrations can enlighten the interactions between the components. The effects of the relative locations of wing-propeller on noise propagation are evaluated at this point by changing the wing position. Figure 68 shows three different geometric configurations representing the different wing positions in the x-axis relative to the propeller. The illustrated wings are at the same relative height, dz/R , and it is equal to 0.5.

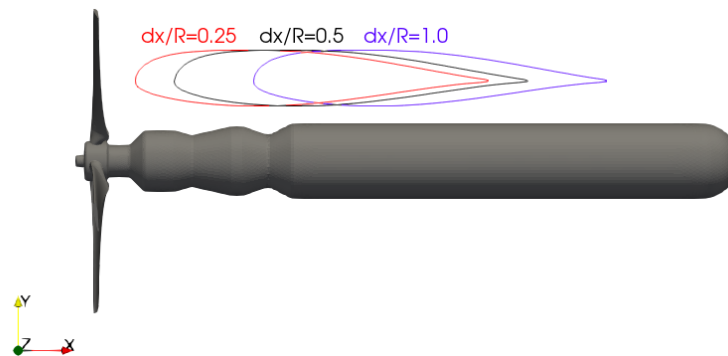


Figure 68: Different positions of the wing relative to the propeller with constant height ($dy/R=0.5$).

The noise propagations emitted by the propeller in the configurations considering different wing positions are evaluated and demonstrated in Figure 69. Again, sound pressure levels corresponding to fundamental blade passage frequency are computed for different microphone locations where the spectrum of θ angle is between 45-deg and 135-deg. The isolated propeller (orange) and the full-body configuration, when dx/R is 0.5 (black), show similar characteristics. However, when the wing moves forward and backward, it is observed that noise reduction occurs at some microphones. The observer point at 115-deg perceives the noise signal low, even less than 25dB, for the configuration corresponding to $dx/R=0.25$. Besides, the wing position, placed at $dx/R=1.0$, causes noise reduction as well.

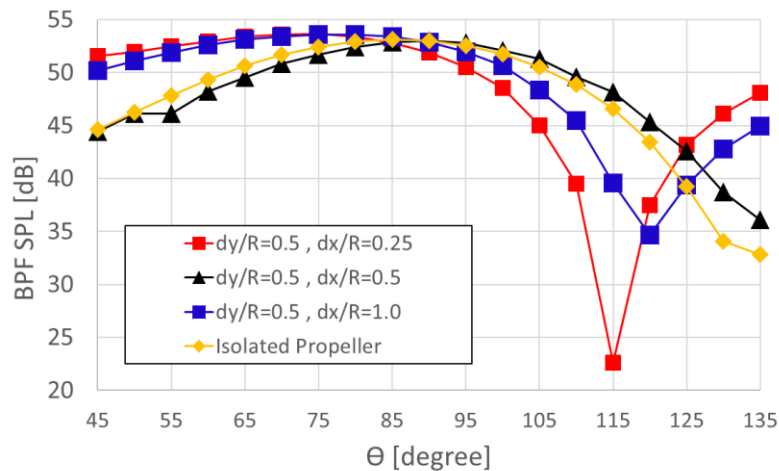


Figure 69: Noise emitted from the propeller for different wing-propeller configurations at different microphone locations.

In conclusion, the relative position of the wing or propeller has a high impact factor for aeroacoustic performance wing-propeller assembly. It is not in the content of this dissertation, but the optimum wing placement might be an excellent topic to be investigated in further studies.

CHAPTER 7

APPLICATIONS OF DESIGN OPTIMIZATION

This chapter addresses the applications of the developed optimization framework for a proprotor, 3BHTP. To deliver an optimized design, some crucial steps must be evaluated. The first step, sensitivities, constitutes the foundation of the optimization cycle. The utilized method, algorithmic differentiation, derives adjoints, and the adjoint-based optimization finds optimum design much faster, as mentioned in the previous sections. The sensitivities section involves verification studies for acoustic adjoints and sensitivities for design variables. The second step is parameterization that demonstrates how shape deformation variables are parameterized. Also, objective function, constraint(s), and side constraints (a.k.a. upper and lower bounds) are described in that section. Finally, the results obtained from optimization runs are demonstrated by including aerodynamic and aeroacoustic performances and shape changes.

7.1 Sensitivities

The implemented method includes computation for only one node on the blade surface. By the applied perturbation on the node, it is possible to find partial derivatives. The location of the node should be around the tip region that is more sensitive to noise propagation. For an illustrative purpose, let the function of the acoustic objective be shown as J that equals sound pressure level. The calculations, AD and CD, derive partial derivatives with respect to the conservative variables, as shown in Table 4. The results in Table 4 indicate relative errors in the order of 10^{-12} or smaller; hence, a successful verification has been achieved. (In the table below, the first nonmatching digits are printed in red.)

Table 4: Sensitivity verification of 3BHTP.

	Sensitivities with respect to grid coordinates		
	$\frac{\partial J}{\partial x}$	$\frac{\partial J}{\partial y}$	$\frac{\partial J}{\partial z}$
Complex	3.08076498355256E-06	4.34231946052742E-06	-4.69514172868562E-06
Algorithmic	3.08076498355797E-06	4.34231946052224E-06	-4.69514172868941E-06
Relative Error	1.76E-12	1.19E-12	8.07E-13
	Sensitivities with respect to conserved state variables		
	$\frac{\partial J}{\partial \rho}$	$\frac{\partial J}{\partial(\rho u_x)}$	$\frac{\partial J}{\partial(\rho u_y)}$
Complex	5.56754302938544E-05	8.14390936251084E-07	-1.57902880043867E-07
Algorithmic	5.56754302938265E-05	8.14390936251096E-07	-1.57902880043919E-07
Relative Error	5.01E-13	1.47E-14	3.29E-13
	$\frac{\partial J}{\partial(\rho u_z)}$	$\frac{\partial J}{\partial(\rho E)}$	
Complex	-1.44517576643667E-07	-3.24143151177512E-10	
Algorithmic	-1.44517576643658E-07	-3.24143151177473E-10	
Relative Error	6.23E-14	1.20E-13	

Additionally, sensitivities with respect to the grid coordinates are demonstrated in Figure 70. On a single blade surface, the distribution of the instantaneous partial derivatives gives an idea about sensitivities. As seen in that figure, the most sensitive nodes are in the near-tip region. That situation gives an idea of how to set up the design variables in an optimization process. Briefly, the effective way to improve aeroacoustic performance is to modify the tip region.

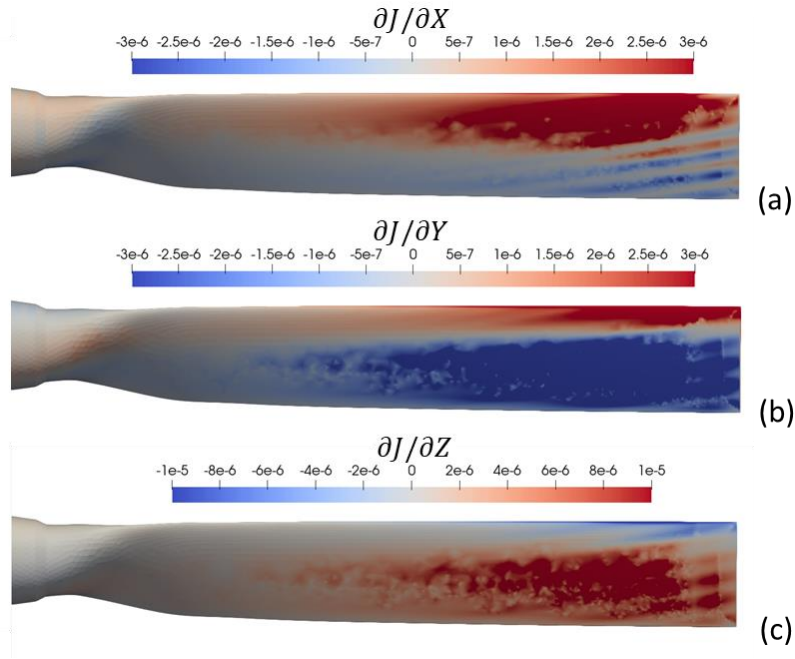


Figure 70: Sensivities with respect to the grid coordinates; (a) $\partial J/\partial x$; (b) $\partial J/\partial y$; and (c) $\partial J/\partial z$ on the blade surface framed with red dashed line.

Table 5: Finite difference validation of the sensitivity for a design variable (movement of the tip inward direction).

	Forward Flight	
	Sound Pressure Level	Thrust
Finite Difference	1.2294903020E-02	-8.4799762120E-06
Adjoint	1.2883194023E-02	-8.4798234176E-06
Error	4.57E-02	1.80E-05
	Hover	
Finite Difference	3.6245346334E-02	-6.3438192941E-06
Adjoint	3.6441611124E-02	-6.3358191756E-06
Error	5.39E-03	1.26E-03

Another verification study is conducted for the adjoints obtained for a particular variable. The variable controlling the blade tip deformation in the inward direction is preferred for that study. Gradients obtained from the adjoint operation are mainly compared with the gradients attained from the finite difference method, as seen in Table 5. According to the error values, it can be stated that the gradients are similar. On the other hand, the adjoint has superior advantages in computational cost. Therefore, utilizing adjoint for the optimization is preferable to the finite difference method.

7.2 Parameterization

The scope of the present optimization study is the shape optimization of propeller blades. In the optimization loop, the blade shape needs to be updated before the next set of computations. SU2 has its own grid deformation tool, SU2-DEF, that moves grid points while keeping the same connectivity. That enables the user to morph the grid but within a limited range to avoid negative volume structure. The grid deformation process employs the free form deformation (FFD) boxes. The control points at the box's corners manage the movement of the surface grid that the FFD box encloses.

The reconstruction of the FFD boxes for the 3BHTP is performed (Figure 71). Roughly, FFD boxes wrap 80% of the span of each blade. The individual FFD box defined for each blade moves simultaneously. As depicted in Figure 72, the control points move and rotate in the direction shown with colored arrows. To prevent sharp changes on the surface, the control points at the near-hub station are set to be fixed.

The control points near trailing and leading edges move in the direction of red arrows to parameterize chord length. Moreover, middle control points move in the direction of the blue arrow to assess the cambered airfoil effects on the performance. Additionally, the tip region

inward movement is controlled as shown with green arrows. That deformation changes the blade span and tip speed. Lastly, planes at each radial station manage the twist angle of airfoils by the given rotation inputs. Overall, optimization studies consist of 55 design variables using the Bezier-Bernstein polynomials for the deformations.

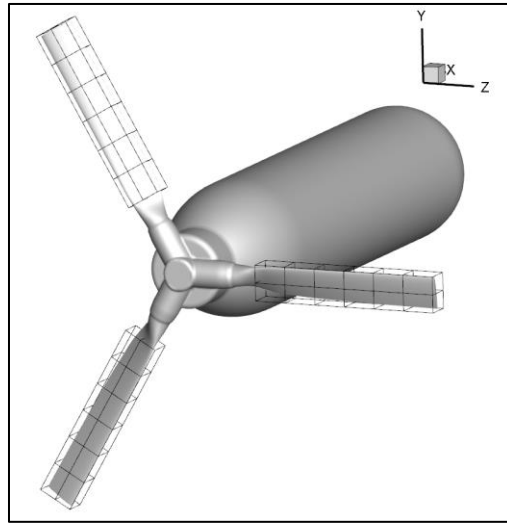


Figure 71: FFD boxes wrapping three blades of the prop rotor.

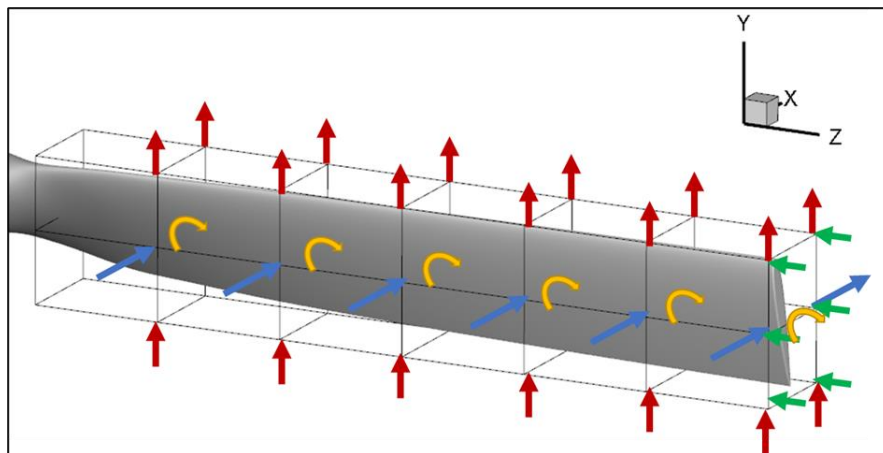


Figure 72: FFD boxes wrapping the blade and parameterization of control points.

A multipoint optimization combines disparate flow regimes in one platform. To accomplish that, one objective function that rules all flow regions needs to be defined. an objective function corresponding to multiple observers and the multipoint-based optimization problem is described as follows:

$$F = 10 \log_{10} \left(\int_{\theta_{min,ff}}^{\theta_{max,ff}} \frac{\langle p^2 \rangle_{A,ff}}{\sin \theta} d\theta \right) + 10 \log_{10} \left(\int_{\theta_{min,h}}^{\theta_{max,h}} \frac{\langle p^2 \rangle_{A,h}}{\sin \theta} d\theta \right) - 20 \log_{10} \left(\frac{p_{ref}^2}{2\pi h^2} \right), \quad (7.1)$$

where F is the objective function and θ is the angle between the observer/microphone and the longitudinal axis of the proprotor according to the center of the rotor. $\langle p^2 \rangle_{A,ff}$ and $\langle p^2 \rangle_{A,h}$ are A-weighted summations of all frequency data for the forward flight and hover conditions, respectively.

Furthermore, the constraint function also needs to be defined to include multipoint optimization. According to the scope of the optimization, various constraint functions can be utilized. An improvement in the noise propagation likely worsens the aerodynamic performance of the proprotor. The first and essential aerodynamic performance parameter is thrust value. The thrust output is preferred as a constraint in every optimization study presented in the dissertation. Moreover, the power consumption is a crucial parameter for the optimization, including omega as a design variable. Therefore, it is assigned as a constraint function for some optimization runs. The multipoint constraint functions for the thrust and power are the summation of the output derived from the CFD analysis for the hover and forward flight cases.

7.3 Results

7.3.1 Optimization-I

The results obtained from the optimization are discussed in this section. First, a comparison of the optimum and baseline blade shapes is shown in Figure 73. The dashed black line and solid red line represent optimized and baseline surfaces, respectively. The optimized surface improves the aeroacoustic performance of the proprotor in both forward flight and hovering while maintaining the thrust value. According to the comparison of airfoils at the different radial stations, chord length becomes shorter at the blade tip with a cambered profile. While the twist angle increases around the tip region, the middle sections have reduced twist angles.

In addition, deformations at the tip include morphing in the radial direction. The optimization results indicate that the leading edge of the tip section moves inward, as seen in Figure 74. On the other hand, the trailing edge moves outward. That situation is due to the multidisciplinary objective where decreasing the blade radius increases the thickness noise; however, it reduces the thrust value. Therefore, the overall blade radius could not change.

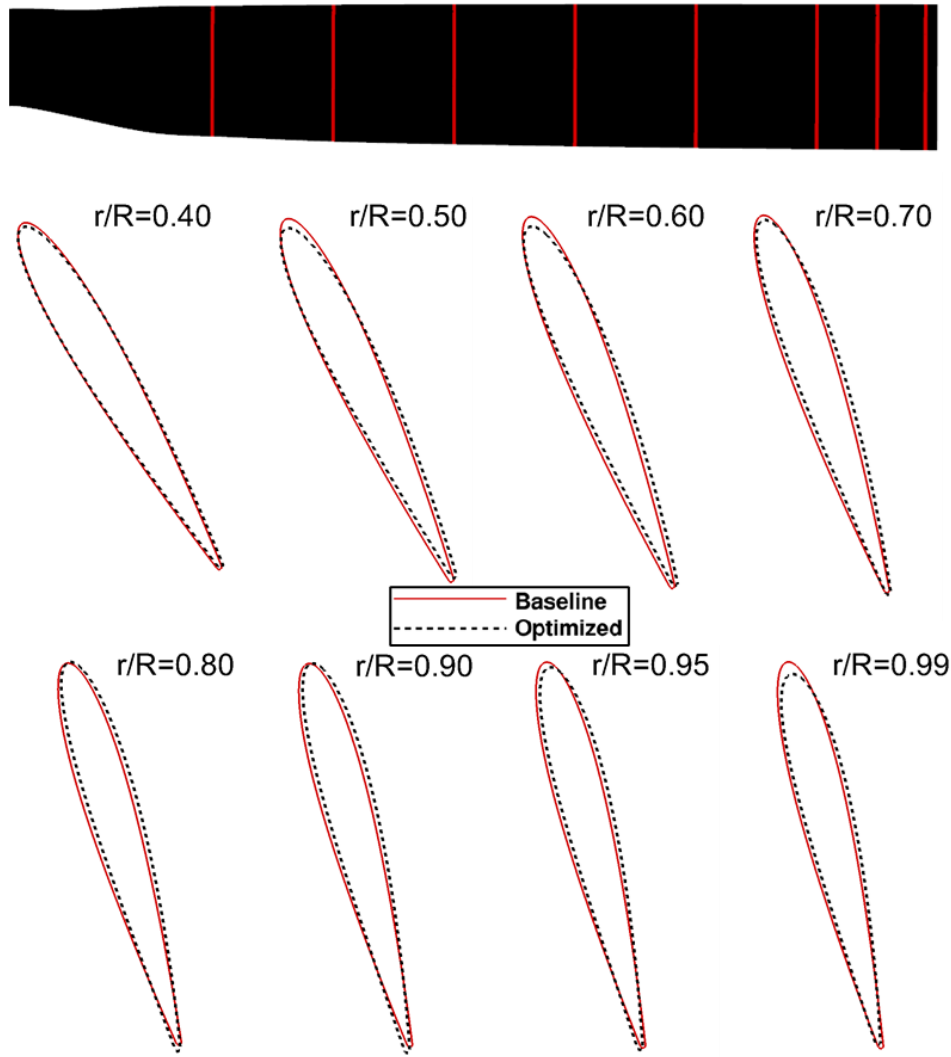


Figure 73: Radial sections of baseline and optimized blade geometries.

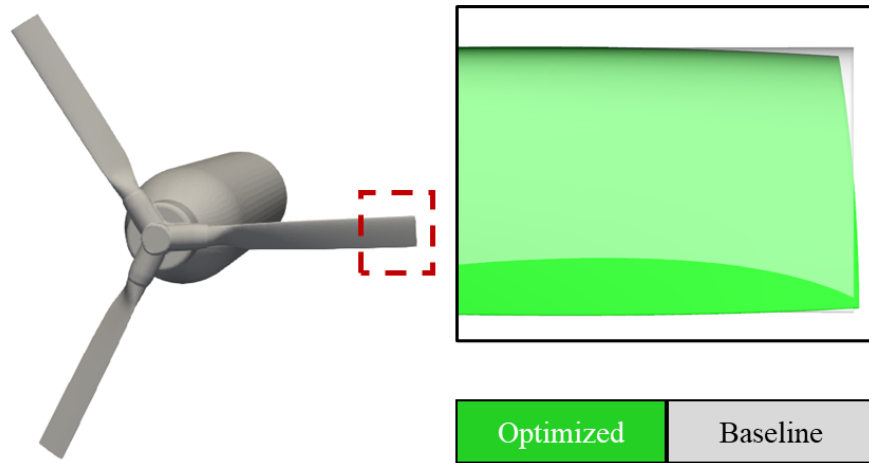


Figure 74: Blade deformation at the tip region.

The performance comparison of the blade shapes is evaluated from the aeroacoustic point of view. In Figure 75, SPL data corresponding to the blade passing frequency demonstrate the improvements in the noise levels for all observer points. The green lines represent the acoustic computation obtained from the optimized surface, and black lines are derived from the baseline surface. It is observed that the enhancements increase in the downstream region in comparison with the upstream region. As a result, the optimized surface offers quite satisfactory aeroacoustic performance for both hover and forward flight scenarios for all microphone positions.

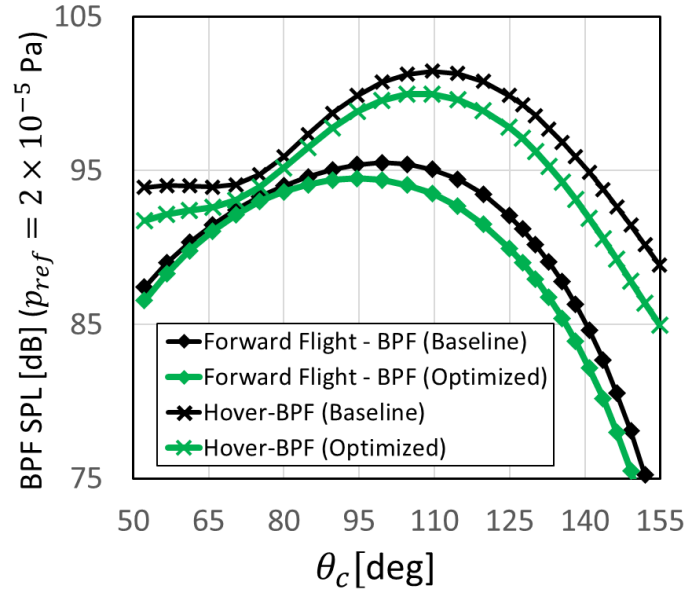


Figure 75: Comparison for SPL of baseline and optimized proprotor for the forward flight and hover cases.

Figure 76 demonstrates the comparison of baseline and optimized surfaces for the second and third harmonics. The results for the forward flight configuration (Figure 76(a)) are slightly different for all microphone positions. However, optimized design impacts the second and third harmonics considerably in hover configuration (Figure 76(b)).

The aeroacoustic performance comparisons are also made for individual observer points. Figure 77 and Figure 78 show comparisons of the optimized and baseline results for θ angle equal to 94.6° and 114.6° , respectively. The time histories of acoustic pressure in Figs. Figure 77(a) and Figure 78(a) clearly demonstrate the improvements in the results derived by optimized surfaces. Improvement also can be seen on spectral data shown in Figs. Figure 77(b) and Figure 78(b). The performance difference between the two proprotors primarily appear in the blade passing frequency, which is 360 Hz.

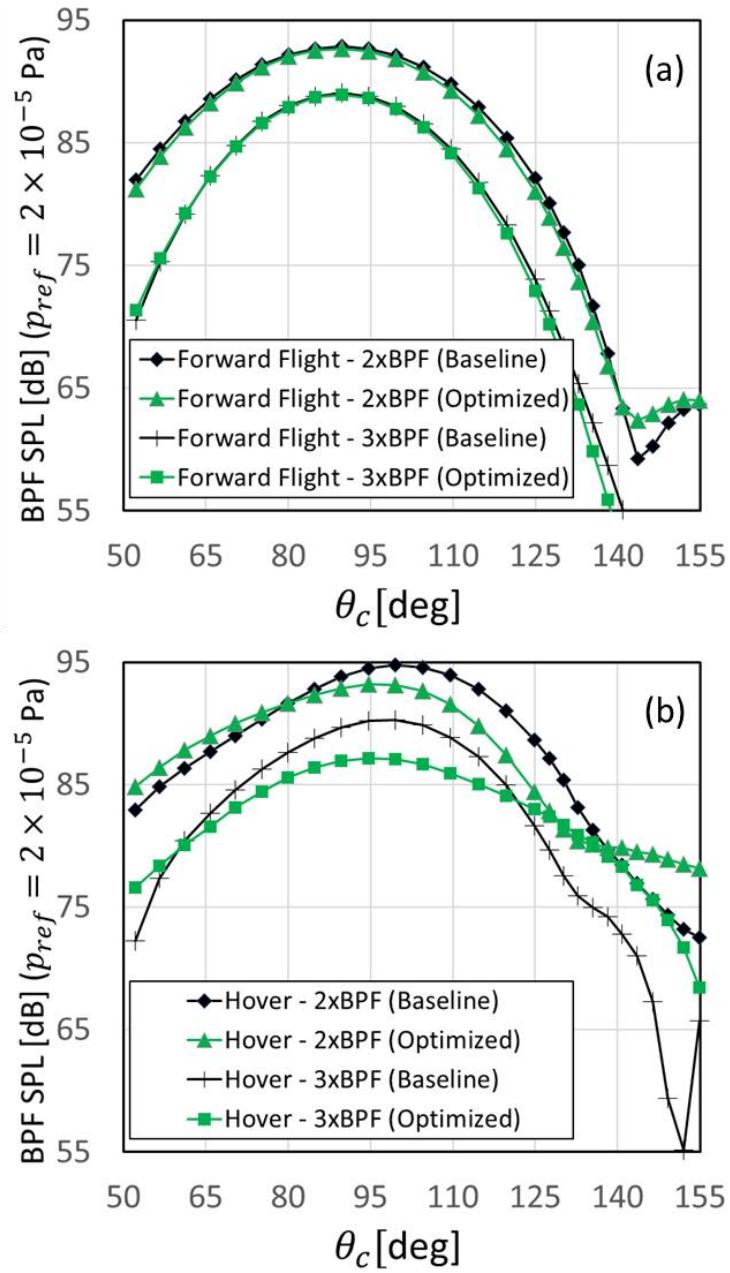


Figure 76: Comparison for SPL corresponding to the second and third harmonics of baseline and optimized proprotor for: (a) the forward flight, (b) hover configurations.

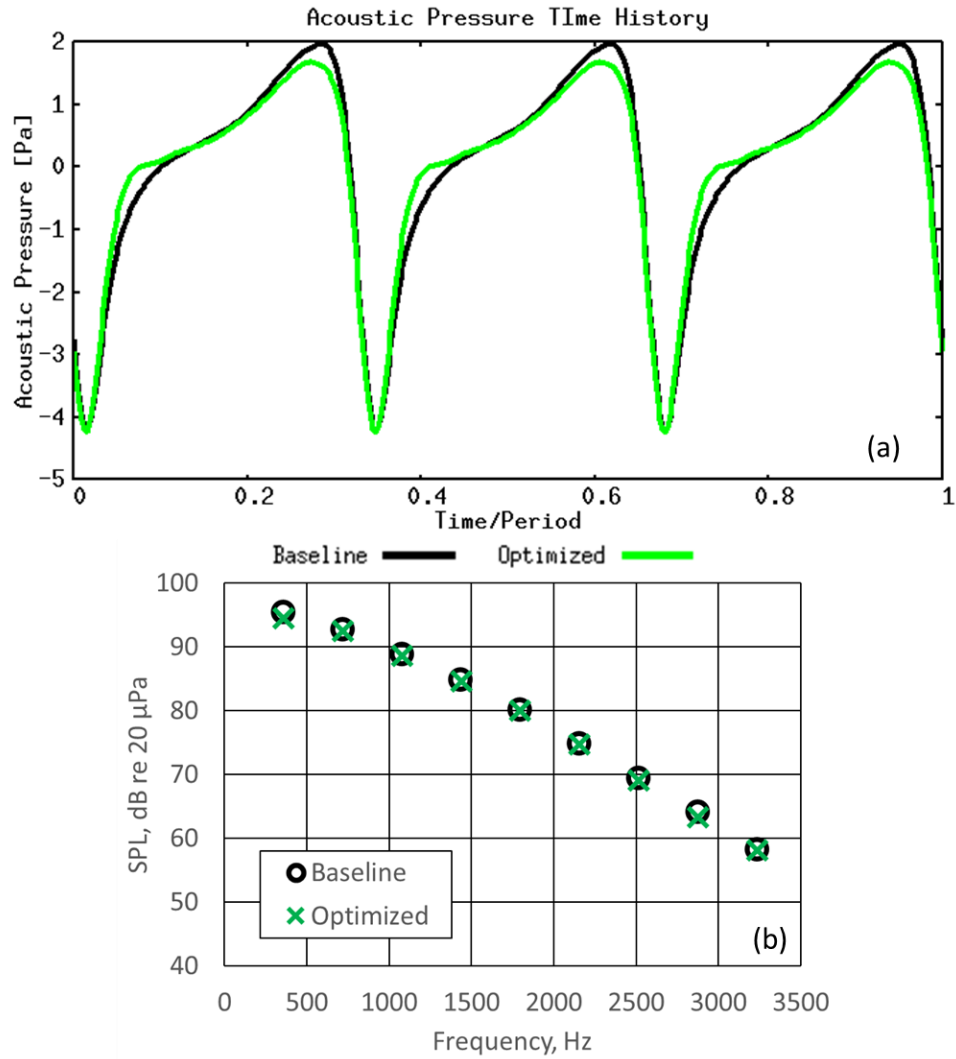


Figure 77: Comparison of the baseline and optimized surface for observer-10 ($\theta = 94.6^\circ$) in (a) time domain and (b) frequency domain.

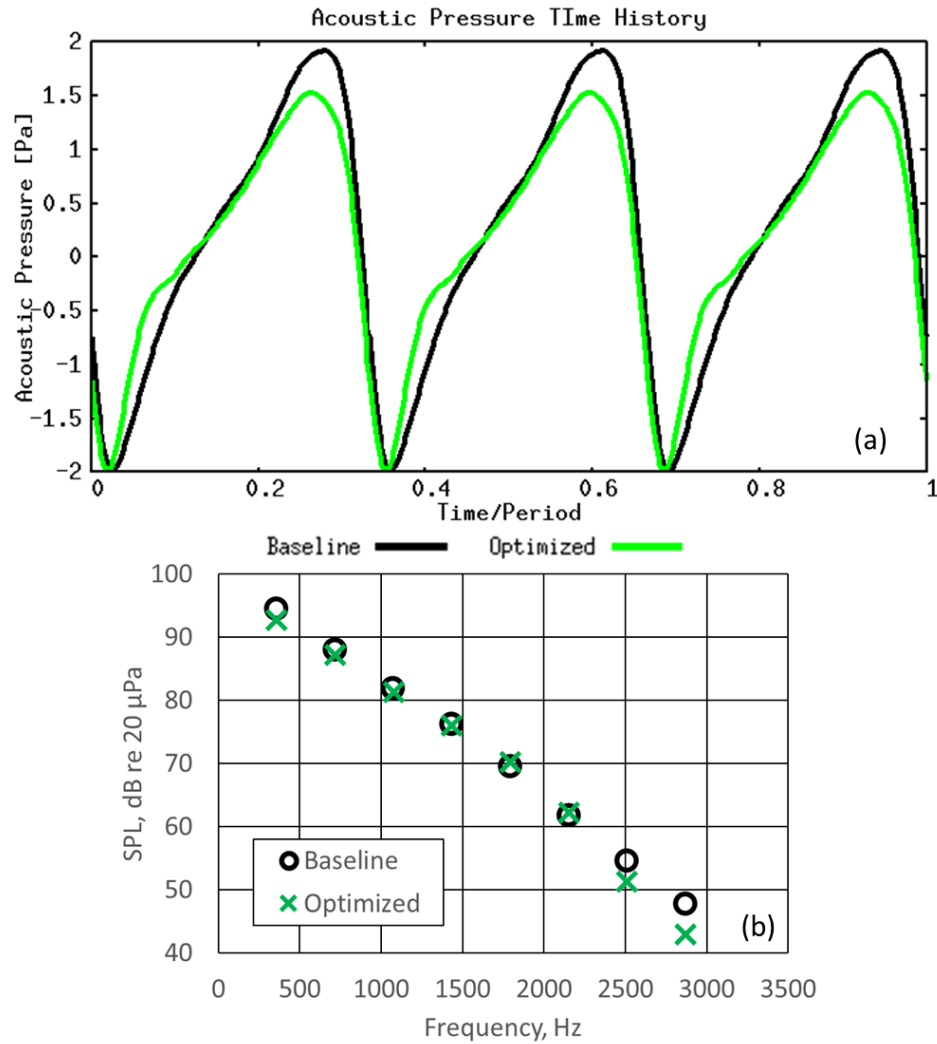


Figure 78: Comparison of the baseline and optimized surface for observer-14 ($\theta = 114.6^\circ$) in (a) time domain and (b) frequency domain.

Displaying the components of the acoustic pressure, which are thickness noise and loading noise, demonstrates which noise source is dominant or improved (Figure 79). Comparing the optimized and the baseline surfaces helps us understand the improvements. Figure 79(a) and Figure 79(b) indicate that the improvements originate from loading. On the other hand, thickness noise components are almost the same for both surfaces. Thickness noise

is proportional to the tip speed. Therefore, the thickness noise is not expected to change much since the optimized blade is about the same span length as the baseline surface.

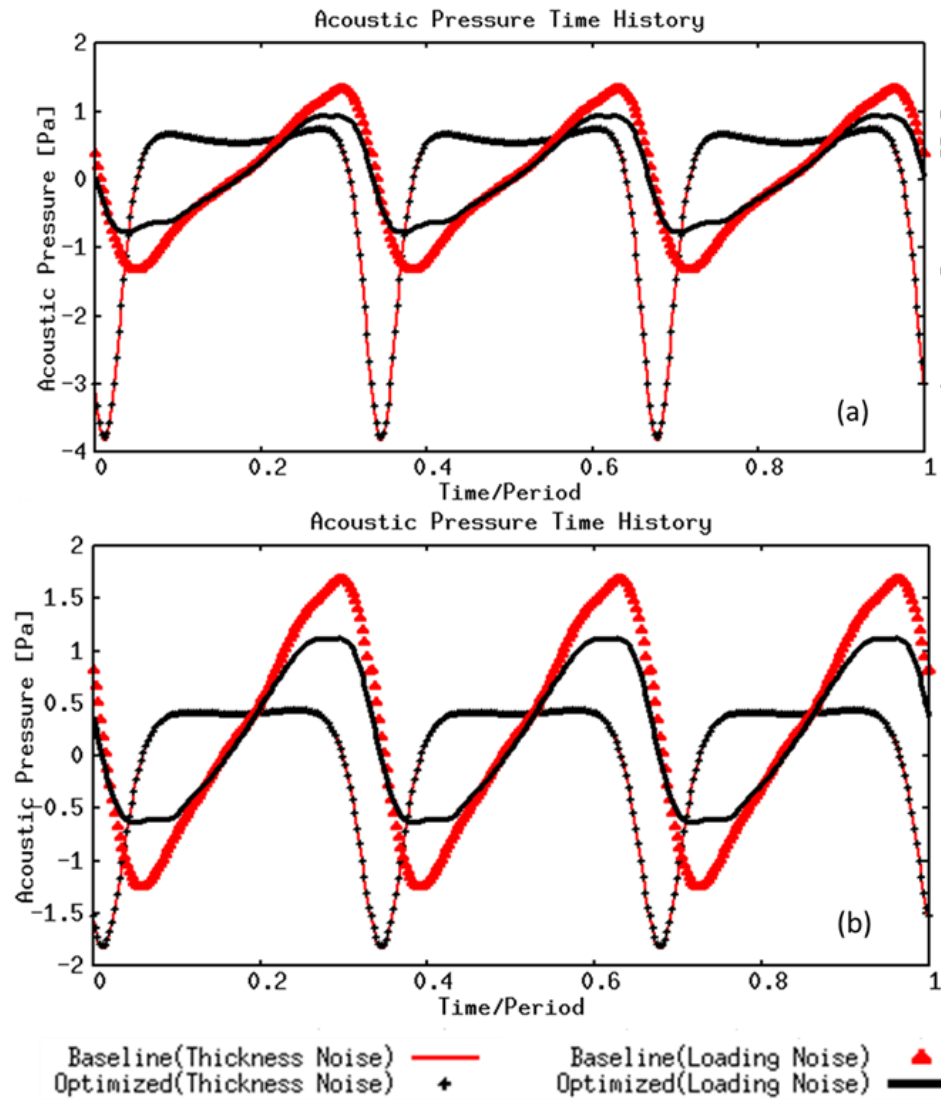


Figure 79: Thickness noise and loading noise components of the acoustic pressure emitted from baseline and optimized surfaces for: (a) observer-10, (b) observer-14.

7.3.2 Optimization-II

Another optimization study is conducted with revised FFD boxes and fewer design variables, as depicted in Figure 80. The new boxes are oriented according to individual airfoils at the radial stations. Also, camber airfoil is not assigned as a design variable. That combinations enable to keep airfoil profile the same. In addition to the previous optimization, the bounds are extended to be able to do large deformation. The preferred design variables are chord length (red arrows), blade radius (green arrows), and twist angles (yellow arrows). Chord length is not considered for the tip section to avoid negative volume and mesh intersections due to the limitations of the mesh deformation tool at the sharp edges.

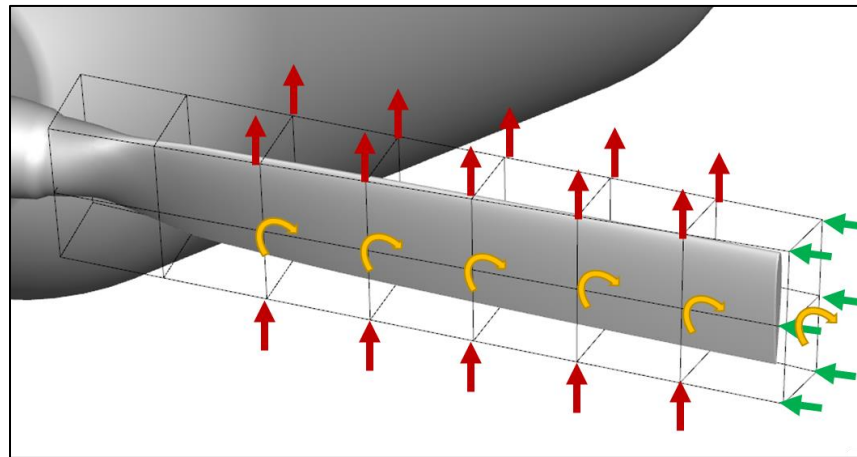


Figure 80: Revised FFD boxes and parameterization of control points.

The objective function for the noise propagation is the same as the previous optimization. Similarly, it is a multipoint optimization that includes forward flight and hover configurations. The constraint function consists of the thrust value obtained from multipoint CFD simulations.

The acquired optimized (green) and baseline (gray) surfaces are shown in Figure 81. The view of the pressure side (Figure 81(a)) of the blade shows that the optimized shape has reduced

blade radius. It can be anticipated from Figs. Figure 81(a) and Figure 81(b) that the tip section has negative twist angles, and the middle sections of the blade are twisted in the positive direction. Also, for the optimized surface, the chord lengths around the middle sections seem larger than the baseline surface.

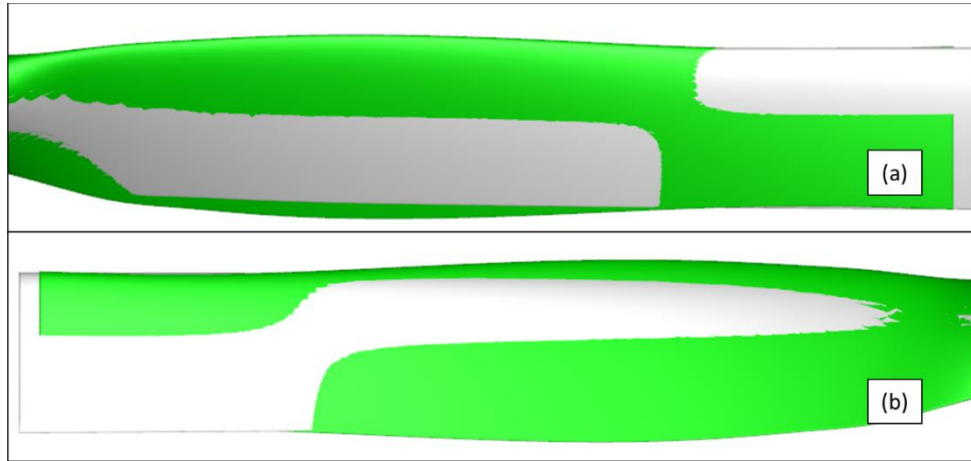


Figure 81: (a) Pressure and (b) suction side of optimized (green) and baseline (gray) surfaces.

The detailed comparison is performed by visualizing some of the radial stations along the blade surface (Figure 82). The airfoil profiles are demonstrated in green lines for the optimized surfaces and red lines for baseline surfaces. From hub to the section at r/R equal to 0.80 of the optimized surfaces, chord length of the airfoils is larger than baseline surface. Also, for the same region, the optimized surface is twisted in the positive direction. On the other hand, twist angles increase at the tip region with decreasing chord length. As a reminder, chord length does not change at the tip station due to the definitions for FFD boxes.

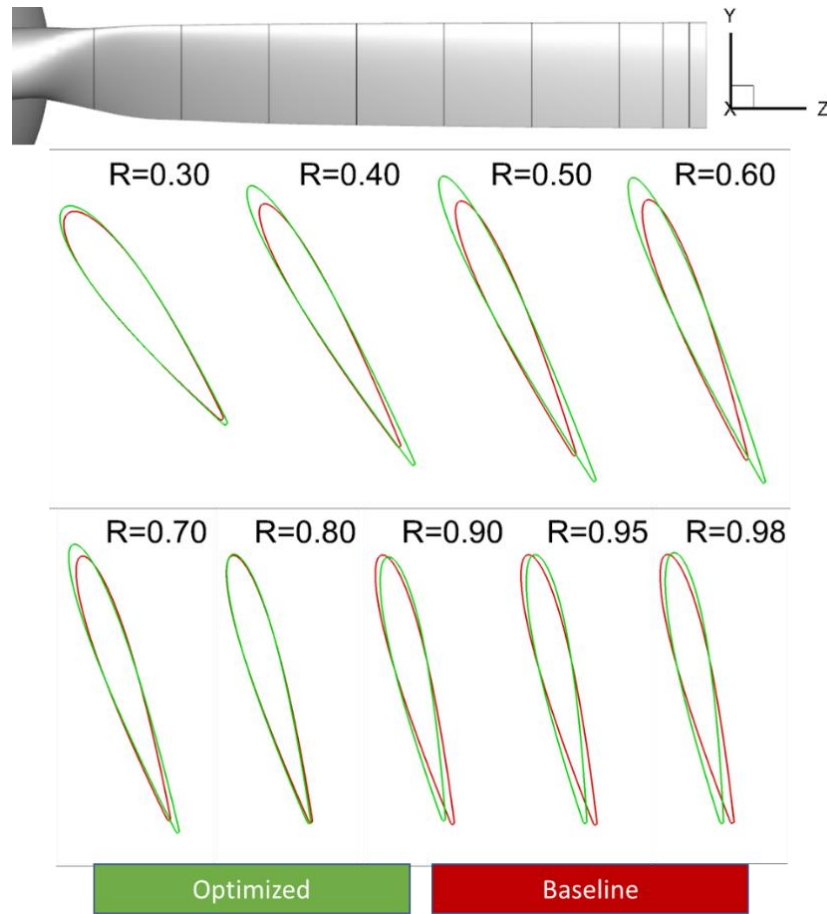


Figure 82: Radial sections of baseline and optimized blade geometries.

The aeroacoustic results based on the second optimization study are presented by showing SPL values corresponding to the fundamental frequency (Figure 83) and second and third harmonics (Figs. Figure 84 and Figure 85). The optimized surface minimizes the radiated noise for both hover and forward flight configurations in fundamental frequency. Especially for the downstream region after 110-deg, noise reduction soars for hover configuration (Figure 83). While SPLs in fundamental frequencies decline not as much as the first optimized surface outputs, the second and third harmonics improvements become more evident for the second optimized surface (Figs. Figure 84 and Figure 85). Overall, the optimized surface demonstrates much better performance for hover configuration.

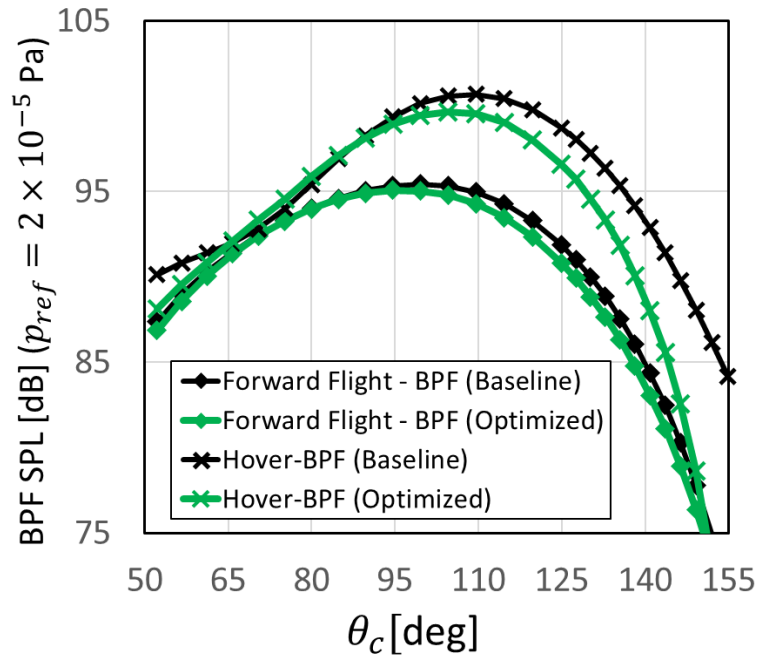


Figure 83: BPF SPL of the second optimized propotor in hover and forward flight configurations.

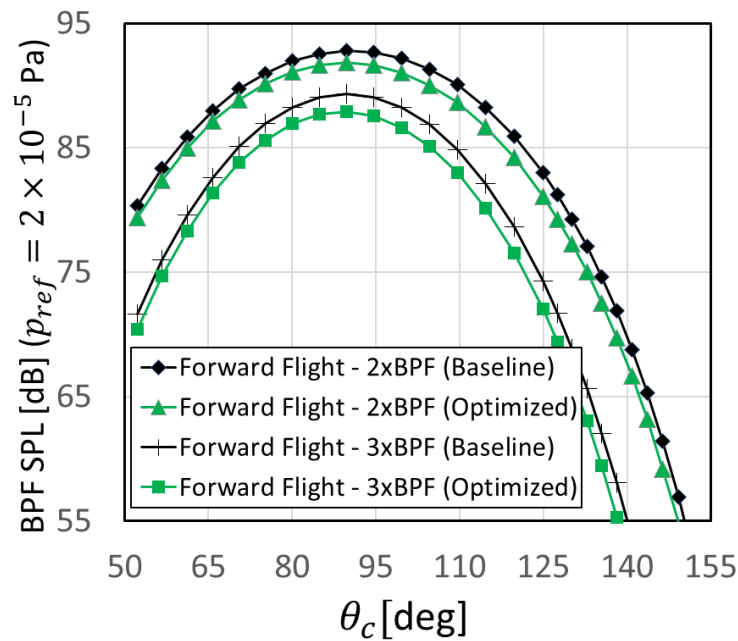


Figure 84: Second and third harmonics SPLs of the second optimized propotor in forward flight configuration.

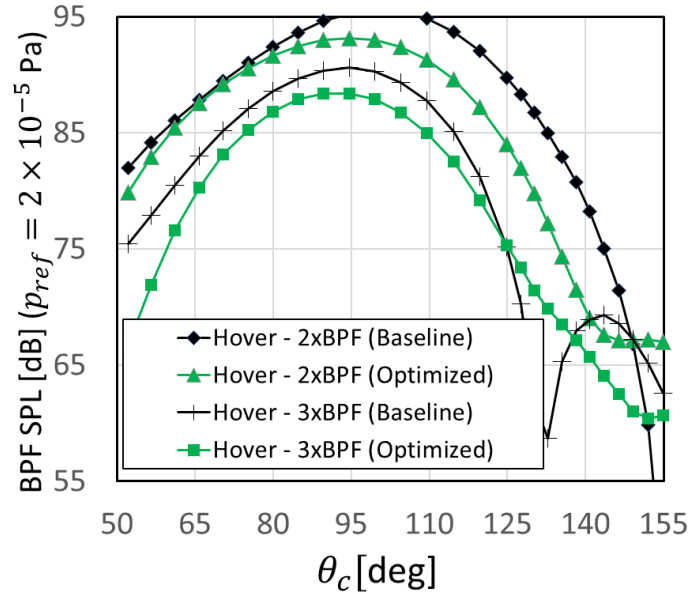


Figure 85: Second and third harmonics SPLs of the second optimized proprotor in hover configuration.

In addition to aeroacoustic assessments, comparisons of optimized and baseline surfaces are performed from an aerodynamic evaluation perspective. The reduced blade radius affects thrust value in a worsening way. However, the increasing twist angles and chord lengths at the midsection of the blade compensate for that impact. The thrust value is set as a constraint function. Besides, the power of the proprotor remains the same for optimized surface together with thrust value. The assessments also involve skin friction coefficient distribution over blade surfaces. Figure 86 compares the optimized and baseline surfaces in terms of skin friction coefficient for forward flight. Qualitatively, the distribution of the coefficient on the optimized surface has smoother gradients. Besides, it seems that the tip region of the optimized blade has lower skin friction. In Figure 87, similar comparisons are made for hover configuration. Again, sharp gradients and the area of skin friction becomes minimized on the optimized surface.

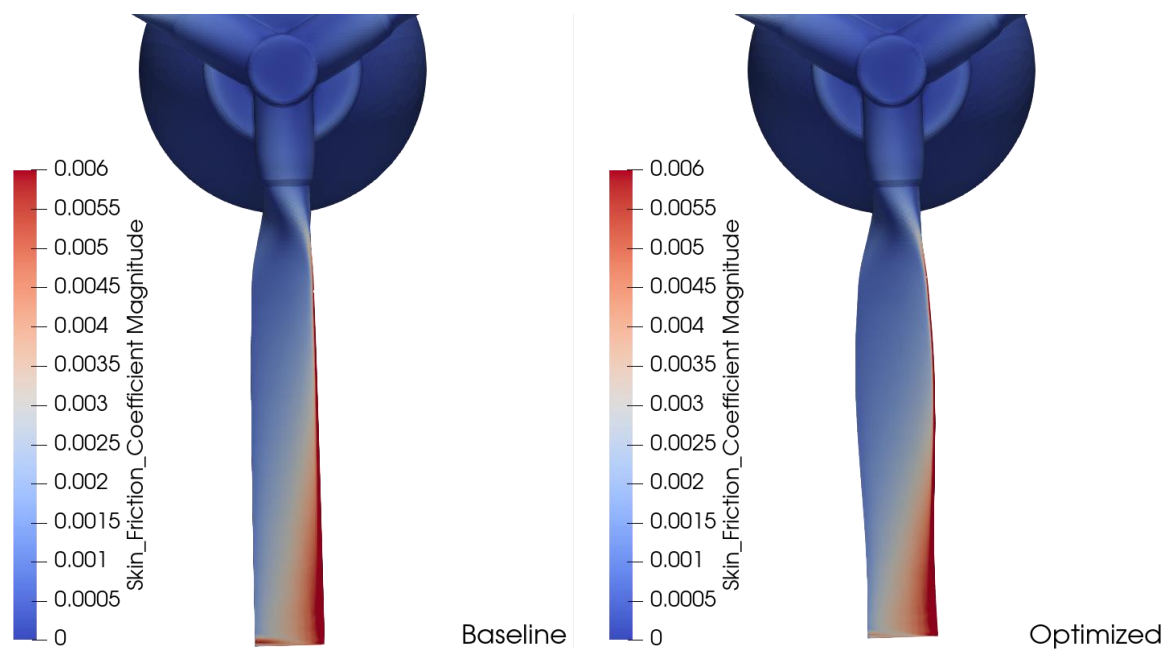


Figure 86: Skin friction coefficient distribution over Baseline and Optimized surfaces in forward flight configuration.

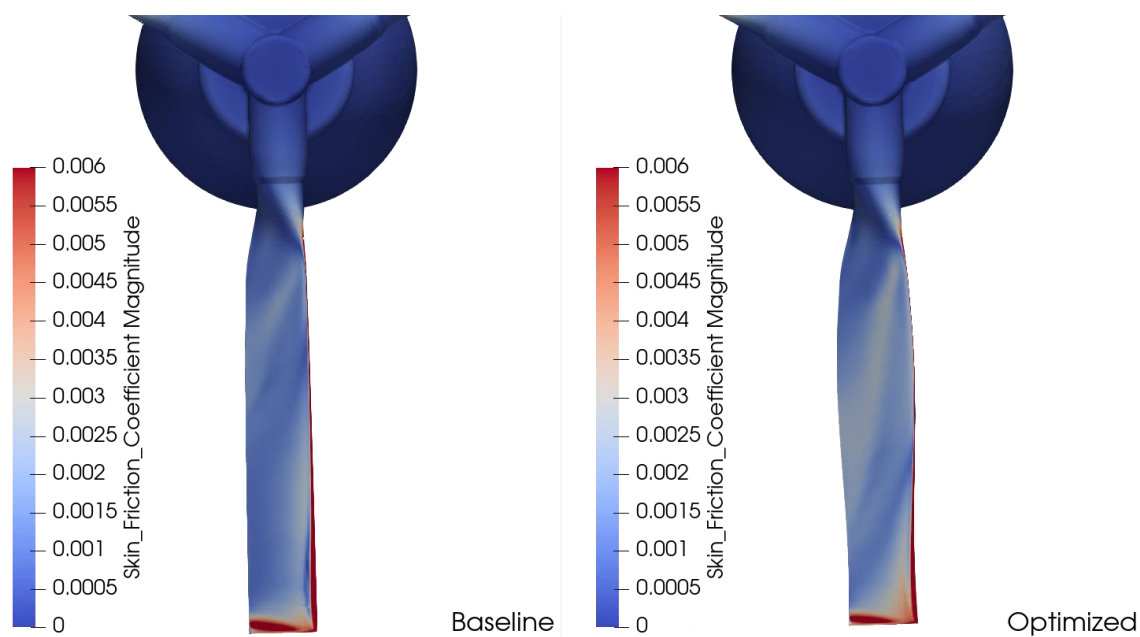


Figure 87: Skin friction coefficient distribution over Baseline and Optimized surfaces in hover configuration.

7.3.3 Optimization-III

The last optimization study is conducted to involve the rotation rate of the propotor as a design variable. That extension allows optimization to reduce the tip speed of blades. Thus, lower tip speed directly reduces the noise propagations significantly. In addition to thrust constraint, the power of the propotor is assigned as a constraint. In this result section, three developed FFD functions, FFD_Scale, FFD_Translate, and FFD_Twist, perform surface deformations. The deformations cover sectional chord lengths, blade radius, and sectional twist angles of the blade. Figure 88 shows the FFD boxes and the identification of planar sections. Instead of using independent control points, FFD functions move a control point together with other points on its sectional plane in this optimization study. FFD_Translate moves Plane 0 inward or outward according to input. Chord lengths at the radial stations, Planes 1-5, are assigned as design variables by employing the FFD_Scale. Moreover, design variables include twist angles at Planes 0-6. In summary, the objective function is noise propagation; constraints are aerodynamic thrust and power values; and design variables are blade radius, twist angles, chord lengths, and rotation rate.

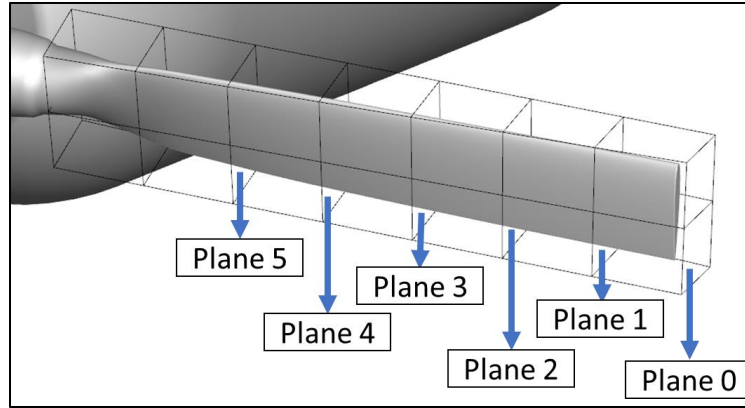


Figure 88: Revised parameterization and identification of the radial planar sections of FFD boxes.

As a result of the optimization process, the new optimized design provides the aerodynamic performance output depicted in Table 6. Even though the rotation speed of the propeller decreases, the thrust value slightly increases, and aerodynamic power decreases for both flight configurations. Before aeroacoustic assessments, it can be indicated that the new design provides slightly high thrust values with less power consumption.

Table 6: Comparisons for Aerodynamic performance outputs of baseline and optimized design for two flight configurations

	Forward Flight		Hover	
	Baseline	Optimized	Baseline	Optimized
Rotation Rate [RPM]	7200	6703	7200	6703
Thrust [N]	111.48	111.51	258.00	258.90
Power [kW]	6.10	6.01	9.97	9.67

Like the previous optimization, the optimized blade has a reduced radius compared to the baseline surface, as seen in Figure 89. The radius of the new blade shape is 0.30008 m, while the baseline radius is 0.30580 m. The changes for twist angles also can be observed from the figure. The optimized surface has lower twist angles around the tip region and higher twist angles between the hub and mid-blade section.

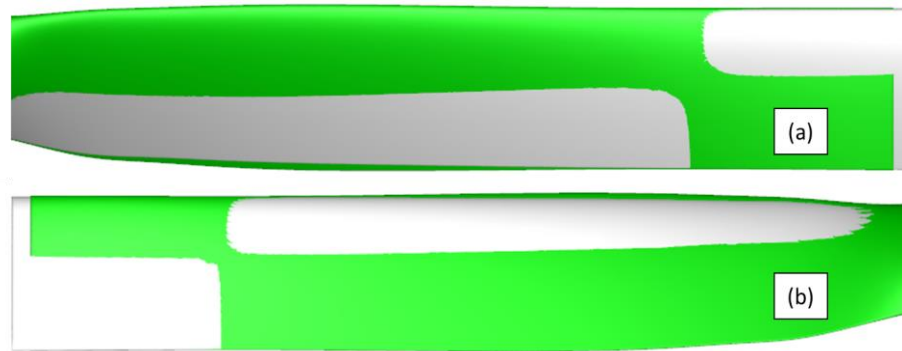


Figure 89: (a) Pressure and (b) suction side of optimized (green) and baseline (gray) surfaces.

Figure 90 demonstrates the radial stations along the propeller blade. From hub to tip, optimized and baseline airfoils are shown in green and red lines. Between the station, $r/R=0.8$, and the blade tip, twist angles decrease. On the other hand, from the hub to the section, r/R is equal to 0.7, larger twist angles are utilized together with larger chord lengths. In that way, the optimized surface could gain aerodynamic thrust from the section from hub to mid-blade while losing due to lower rotation rate, blade radius, and deformations at the blade tips. Again, to avoid the poor mesh structure and negative volume mesh that turns out divergence problems in CFD simulation, chord length at the tip section is not assigned as a design variable, as mentioned before.

Aeroacoustic performance of the new optimized design is evaluated first by SPL values at the different observer locations for BPF, as seen in Figure 91. Like the previous assessments, the optimized and baseline designs are compared for two flight conditions. The optimized design reduces the SPL value all around the observer points by 2-3 dB for forward flight configuration. In hover configuration, the improvements exceed 10 dB at some θ angles. The new optimized design delivers the best aeroacoustic results in comparison with the previous two optimization studies. Covering the rotation speed of the prop rotor in design parameters swells reductions in noise propagation.

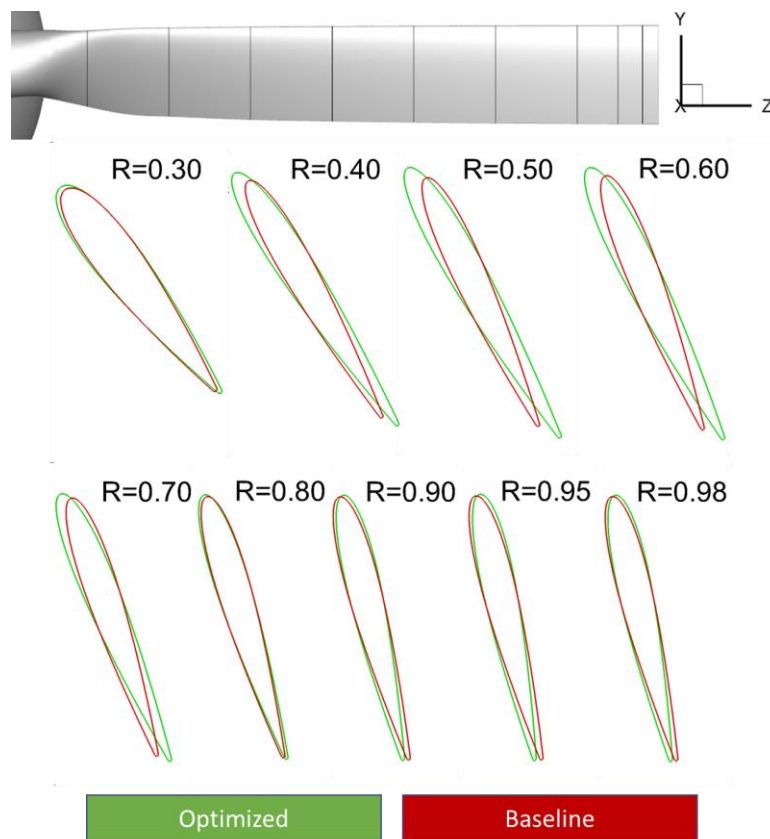


Figure 90: Radial sections of baseline and optimized blade geometries obtained from the optimization when power and omega are included.

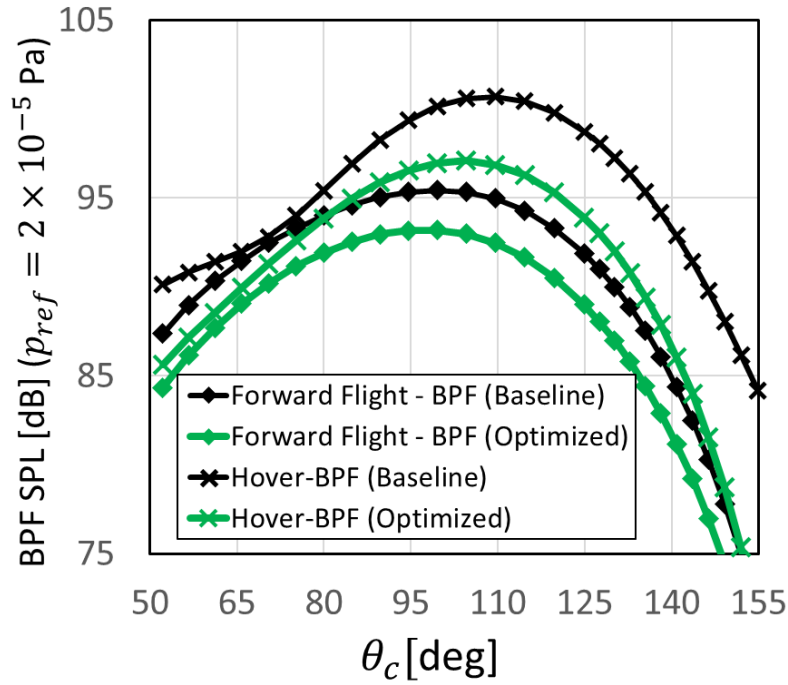


Figure 91: BPF SPL of the third optimized design in hover and forward flight configurations.

The aeroacoustic improvements also can be observed on the second and third harmonics (Figure 92 and Figure 93). In comparison with the previous optimization, the new optimized design propagates quite lower noise at the second and third harmonics. For forward flight configuration (Figure 92), 5 dB and more improvements are obtained for each observer point. Regarding the hover configuration, again optimized design has better aeroacoustic performance except for the observers between 150-155 degrees (second harmonics) and between 125-140 degrees (third harmonics). In summary, the optimized design provides lower noise for the first, second, and third harmonics. Besides, there is no deviation for thrust performance while power consumption of the proprotor decreases for both flight configurations.

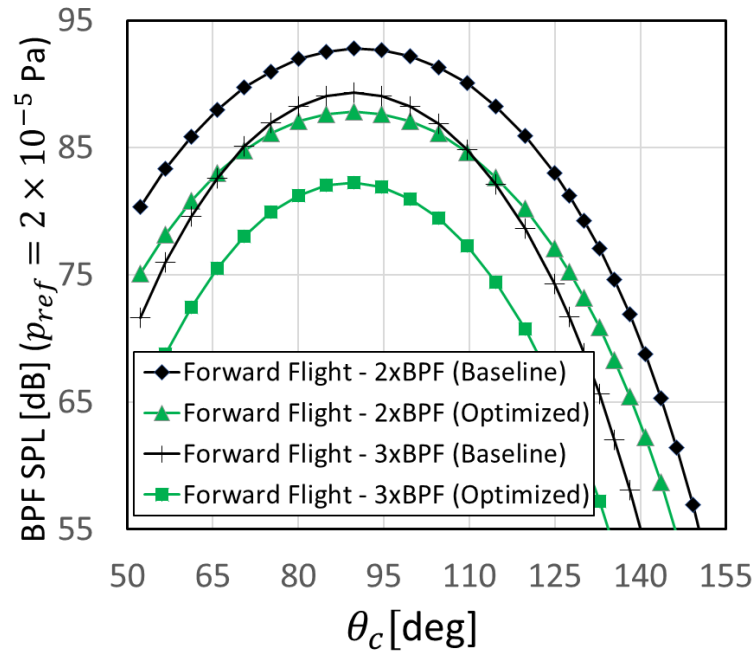


Figure 92: Second and third harmonics SPLs of the third optimized design in forward flight configuration.

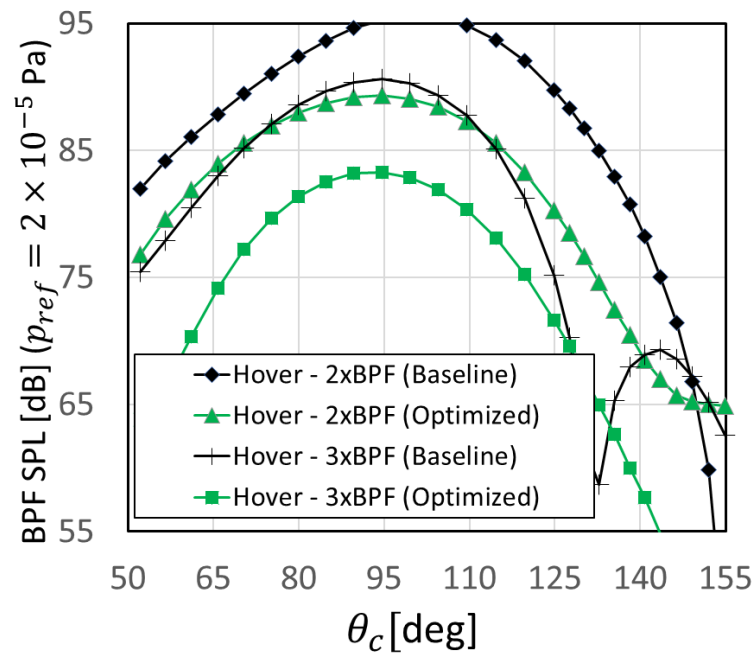


Figure 93: Second and third harmonics SPLs of the third optimized design in hover configuration.

The optimization process takes a long time to find the optimized surface. To show the time that is spent through optimization study, each of the computational steps must be examined. Breakdowns of the processing time at each analysis step are demonstrated in Table 7. The wall clock time data for the analyses for the multiple flight configurations are almost the same. Therefore, the analysis times for both flight configurations are assumed the same in the table. The adjoint solution for the acoustics takes slightly more time than flow adjoint solvers. The overall process time is more than 12 days. That computation performance is good enough for an optimization process consisting of gradient-based optimization, unsteady simulations, multiple flight configurations, multiple observers, and multiple constraints. Some modifications may improve that computation time in the code, such as combining two flow constraints in the same computation or modifying the optimizer module in the python library in future work.

Table 7: Wall clock time breakdowns for the optimization process.

	Wall Clock Time
CFD analysis	4.1 hours
CAA analysis	17 mins
CAA adjoint analysis	4.4 hours
CFD adjoint analysis for Thrust Constraint	4.3 hours
CFD adjoint analysis for Power Constraint	4.3 hours
One optimization iteration w/ adjoint computations	8.7 hours
One optimization iteration w/o adjoint computations	34.8 hours
Total optimization process (17 iterations)	12.7 days

CHAPTER 8

CONCLUSIONS AND FUTURE DIRECTIONS

The present dissertation provides many aspects of aeroacoustic, aerodynamic, and optimization assessments for various rotorcraft applications. A computer code is developed to predict noise propagation for multiple observer positions and to conduct multidisciplinary (aerodynamic and aeroacoustic) design optimization for rotorcraft.

The code development is performed on the open-source software, SU2 suite, utilizing C++ and Python programming languages. The SU2-CAA library is embedded in public version SU2 v7.1.1 and is fully functional with other solvers. The code was verified with benchmark and wind tunnel tests by comparing the computed radiated noises. For the nonce, it uses the Farassat 1A formulation to predict thickness and loading noise.

Secondly, considering multiple flight conditions, the developed multipoint optimization framework reduces the radiated noise while attaining the aerodynamic performance parameters assigned as constraints. Coupled aerodynamic and aeroacoustic adjoint solvers compute sensitivities and reached the optimum solution rapidly. When the developed framework is applied for a proprotor, it successfully obtains a new blade design that improves the aeroacoustic performance of the proprotor and does not sacrifice the thrust. The same geometry is utilized by another research group in NASA Glenn Research Center to design a low-noise propeller, as shown in [98]. The presented results and design parameters in the reference study show similar features.

The main contributions of the dissertation are the detailed derivation, implementation, and application of a new unsteady discrete adjoint solver for aeroacoustic and aerodynamic coupled design optimization of rotorcraft. The developed solver accepts a multidisciplinary

objective, multiple flight conditions, and multiple observers. Besides, enriching the public domain by the open-source code constitutes a valuable contribution to further assessments performed by other researchers. In conclusion,

1. CFD simulations acquire satisfactory results for various rotorcraft applications.
2. The developed CAA code evaluates noise propagation emitted from propellers, rotors, and proprotors accurately and precisely.
3. Aeroacoustic assessments for the wing installed propeller give detailed information about acoustic interactions.
4. The multidisciplinary optimization framework successively reduces noise levels emitted by a proprotor in multiple flight configurations.
5. The optimized design improves emitted noise radiation while satisfying the given aerodynamic constraints.

limitations that can be addressed in future work are classified into three groups: extensive grid deformation, acoustic formulations, and a multizonal approach. Figure 94 demonstrates a sample deformation performed by SU2-DEF resulting negative volume mesh structure at the trailing edge of the blade tip. A possible solution is presented in Ref. [99]. Implementing a third-party grid generator into the optimization cycle may help deform the grid freely while keeping the same grid quality. That enables the user to open the side constraints, resulting in a larger design space. Thus, the optimization tool will be able to achieve more aggressive shape reformations and more enhancements.

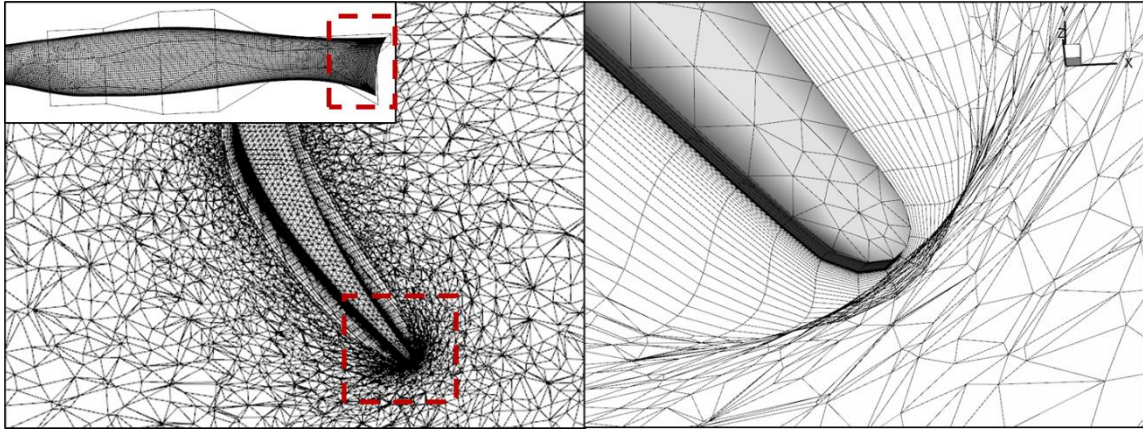


Figure 94: A sample demonstration of an unsuccessful mesh deformation when an extensive deformation is requested.

In addition, the utilized acoustic formulation and implementation do not provide noise prediction for broadband noise (BBN) and quadrupole acoustic terms. Extending the acoustic module with proper formulations can help to resolve those missing parts. Together with the new acoustic implementation, the CFD parts also play an essential role. The fluid domain needs to be resolved with the solver such as LES, DDES, or DES. Additionally, by utilizing machine learning methods, turbulence models in URANS solvers can be improved to resolve fluid domain in terms of turbulence, as shown in Ref. [100]. Also, if applied for the flow field, Farassat Q1A and 2B formulations may gain the code to compute quadrupole terms in compact form.

Finally, although the present optimization results are obtained on single-zone grids that rotate together with the whole domain, it will be valuable to conduct an optimization study including a multizonal grid. By that implementation, wing-propeller or propeller-propeller combination and interaction can be evaluated and improved in noise emission via placement optimization studies.

APPENDIX

Spalart Allmaras Turbulence Model [68]

The turbulent viscosity is derived by

$$\mu_{tur} = \rho \tilde{\nu} f_{v1}, \quad f_{v1} = \frac{\chi^3}{\chi^3 + c_{v1}^3}, \quad \chi = \frac{\tilde{\nu}}{\nu}, \quad (\text{A.1})$$

where the variable $\tilde{\nu}$ is computed by the transport equation below.

$$\frac{D\tilde{\nu}}{Dt} = c_{b1}\tilde{S}\tilde{\nu} + \frac{1}{\sigma}[\nabla \cdot ((\nu + \tilde{\nu})\nabla\tilde{\nu}) + c_{b2}(\nabla\tilde{\nu})^2] - c_{w1}f_w \left[\frac{\tilde{\nu}}{d}\right]^2. \quad (\text{A.2})$$

The production term, \tilde{S} , is equal to

$$\tilde{S} = |\vec{\omega}| + \frac{\tilde{\nu}}{\kappa^2 d} f_{v2}, \quad \vec{\omega} = \nabla \times \vec{v}, \quad (\text{A.3})$$

where $\vec{\omega}$ is the fluid vorticity, d is the distance to nearest wall and f_{v2} is defined as $f_{v2} = 1 - \frac{\chi}{1 + \chi f_{v1}}$. As indicated in Ref. [68], a satisfactory condition is provided by using the following equilibrium for f_w .

$$f_w(r) = g \left[\frac{1 + c_{w3}^6}{g^6 + c_{w3}^6} \right]^{1/6}, \quad g = r + c_{w2}(r^6 - r), \quad r = \frac{\tilde{\nu}}{\tilde{S}\kappa^2 d^2}. \quad (\text{A.4})$$

Lastly, to make it closure problem, we have a couple of constants as below.

$$\sigma = \frac{2}{3}, c_{b1} = 0.1355, c_{b2} = 0.622, \kappa = 0.41, c_{w1} = \frac{c_{b1}}{\kappa^2} + \frac{1 + c_{b2}}{\sigma}, \quad (\text{A.5})$$

$$c_{w2} = 0.3, c_{w3} = 2, c_{v1} = 7.1.$$

REFERENCES

1. Economon, T. D., Palacios, F., Copeland, S. R., Lukaczyk, T. W., and Alonso, J. J. "SU2: An Open-Source Suite for Multiphysics Simulation and Design," *AIAA Journal* Vol. 54, No. 3, 2015, pp. 828-846. doi: 10.2514/1.J053813
2. Berton, J. J., and Nark, D. M. "Low-Noise Operating Mode for Propeller-Driven Electric Airplanes," *Journal of Aircraft* Vol. 56, No. 4, 2019, pp. 1708-1714. doi: 10.2514/1.C035242
3. Chin, J., Aretskin-Hariton, E., Ingraham, D., Hall, D., Schnulo, S. L., Gray, J., and Hendricks, E. S. "Battery Evaluation Profiles for X-57 and Future Urban Electric Aircraft," *AIAA Propulsion and Energy 2020 Forum*. American Institute of Aeronautics and Astronautics, 2020.
4. Viken, J. K., Viken, S., Deere, K. A., and Carter, M. "Design of the Cruise and Flap Airfoil for the X-57 Maxwell Distributed Electric Propulsion Aircraft," *35th AIAA Applied Aerodynamics Conference*. American Institute of Aeronautics and Astronautics, 2017.
5. Hoover, C. B., and Shen, J. "Parametric Study of Propeller Whirl Flutter Stability with Full-Span Model of X-57 Maxwell Aircraft," *Journal of Aircraft* Vol. 55, No. 6, 2018, pp. 2530-2537. doi: 10.2514/1.C035081
6. North, D. D., Busan, R. C., and Howland, G. "Design and Fabrication of the LA-8 Distributed Electric Propulsion VTOL Testbed," *AIAA Scitech 2021 Forum*. American Institute of Aeronautics and Astronautics, 2021.
7. Busan, R. C., Murphy, P. C., Hatke, D. B., and Simmons, B. M. "Wind Tunnel Testing Techniques for a Tandem Tilt-Wing, Distributed Electric Propulsion VTOL Aircraft," *AIAA Scitech 2021 Forum*. American Institute of Aeronautics and Astronautics, 2021.
8. Hasan, S. "Urban air mobility (UAM) market study," *NASA Urban Air Mobility, HQ-E-DAA-TN63497*. 2018.
9. Stoll, A. M., Stilson, E. V., Bevirt, J., and Pei, P. P. "Conceptual Design of the Joby S2 Electric VTOL PAV," *14th AIAA Aviation Technology, Integration, and Operations Conference*. American Institute of Aeronautics and Astronautics, 2014.
10. Lim, T., Sankar, L., Hariharan, N., and Reddy, N. "A technique for the prediction of propeller induced acoustic loads on aircraft surfaces," *15th Aeroacoustics Conference*. American Institute of Aeronautics and Astronautics, 1993.
11. Lyrantzis, A. S. "Surface Integral Methods in Computational Aeroacoustics—From the (CFD) Near-Field to the (Acoustic) Far-Field," *International Journal of Aeroacoustics* Vol. 2, No. 2, 2003, pp. 95-128. doi: 10.1260/147547203322775498
12. Lighthill, M. J. "On Sound Generated Aerodynamically. I. General Theory," *Proceedings of the Royal Society of London. Series A, Mathematical and Physical Sciences* Vol. 211, No. 1107, 1952, pp. 564-587.
13. Curle, N., and Lighthill, M. J. "The influence of solid boundaries upon aerodynamic sound," *Proceedings of the Royal Society of London. Series A. Mathematical and Physical Sciences* Vol. 231, No. 1187, 1955, pp. 505-514. doi: 10.1098/rspa.1955.0191

14. Williams, J. E. F., Hawkings, D. L., and Lighthill, M. J. "Sound generation by turbulence and surfaces in arbitrary motion," Vol. 264, No. 1151, 1969, pp. 321-342. doi: doi:10.1098/rsta.1969.0031
15. George, A., and Lyrintzis, A. "Mid-field and far-field calculations of Blade-Vortex Interactions," *10th Aeroacoustics Conference*. American Institute of Aeronautics and Astronautics, 1986.
16. Lyrintzis, A. S. "Review: The Use of Kirchhoff's Method in Computational Aeroacoustics," *Journal of Fluids Engineering* Vol. 116, No. 4, 1994, pp. 665-676. doi: 10.1115/1.2911834
17. Farassat, F., and Succi, G. P. "A review of propeller discrete frequency noise prediction technology with emphasis on two current methods for time domain calculations," *Journal of Sound and Vibration* Vol. 71, No. 3, 1980, pp. 399-419. doi: [https://doi.org/10.1016/0022-460X\(80\)90422-8](https://doi.org/10.1016/0022-460X(80)90422-8)
18. Brentner, K. S. "Prediction of helicopter rotor discrete frequency noise: A computer program incorporating realistic blade motions and advanced acoustic formulation," *NASA TM 87721*. 1986.
19. Kuntz, M. "Rotor noise predictions in hover and forward flight using different aeroacoustic methods," *Aeroacoustics Conference*. American Institute of Aeronautics and Astronautics, 1996.
20. Brentner, K. "An efficient and robust method for predicting helicopter rotor high-speed impulsive noise," *34th Aerospace Sciences Meeting and Exhibit*. American Institute of Aeronautics and Astronautics, 1996.
21. Farassat, F., and Casper, J. "Broadband noise prediction when turbulence simulation is available—Derivation of Formulation 2B and its statistical analysis," *Journal of Sound and Vibration* Vol. 331, No. 10, 2012, pp. 2203-2208. doi: <https://doi.org/10.1016/j.jsv.2011.07.044>
22. Najafi-Yazdi, A., Mongeau, L., and Bres, G. "An Acoustic Analogy Formulation for Uniformly Moving Media: Formulation 1C," *16th AIAA/CEAS Aeroacoustics Conference*. American Institute of Aeronautics and Astronautics, 2010.
23. Yin, J., Stuermer, A., and Aversano, M. "Aerodynamic and Aeroacoustic Analysis of Installed Pusher-Propeller Aircraft Configurations," *Journal of Aircraft* Vol. 49, No. 5, 2012, pp. 1423-1433. doi: 10.2514/1.C031704
24. Jameson, A. "Aerodynamic design via control theory," *Journal of Scientific Computing* Vol. 3, No. 3, 1988, pp. 233-260. doi: 10.1007/bf01061285
25. Pironneau, O. "On optimum design in fluid mechanics," *Journal of Fluid Mechanics* Vol. 64, No. 1, 1974, pp. 97-110. doi: 10.1017/S0022112074002023
26. Baysal, O., and Ghayour, K. "Continuous Adjoint Sensitivities for Optimization with General Cost Functionals on Unstructured Meshes," *AIAA Journal* Vol. 39, No. 1, 2001, pp. 48-55. doi: 10.2514/2.1269
27. Nielsen, E. J., Lee-Rausch, E. M., and Jones, W. T. "Adjoint-Based Design of Rotors in a Noninertial Reference Frame," *Journal of Aircraft* Vol. 47, No. 2, 2010, pp. 638-646. doi: 10.2514/1.46044
28. Nielsen, E. J., and Diskin, B. "Discrete Adjoint-Based Design for Unsteady Turbulent Flows on Dynamic Overset Unstructured Grids," *AIAA Journal* Vol. 51, No. 6, 2013, pp. 1355-1373. doi: 10.2514/1.J051859

29. Rumpfkeil, M., and Zingg, D. "Unsteady Optimization Using a Discrete Adjoint Approach Applied to Aeroacoustic Shape Design," *46th AIAA Aerospace Sciences Meeting and Exhibit, AIAA 2018-18*. American Institute of Aeronautics and Astronautics, 2008.
30. Economon, T., Palacios, F., and Alonso, J. "A Coupled-Adjoint Method for Aerodynamic and Aeroacoustic Optimization," *12th AIAA Aviation Technology, Integration, and Operations (ATIO) Conference and 14th AIAA/ISSMO Multidisciplinary Analysis and Optimization Conference*. 2012.
31. Gomes, P., Economon, T. D., and Palacios, R. "Sustainable High-Performance Optimizations in SU2," *AIAA Scitech 2021 Forum, AIAA 2021-0855*. American Institute of Aeronautics and Astronautics, 2021.
32. Baysal, O., and Eleshaky, M. E. "Aerodynamic design optimization using sensitivity analysis and computational fluid dynamics," *AIAA Journal* Vol. 30, No. 3, 1992, pp. 718-725. doi: 10.2514/3.10977
33. Eleshaky, M. E., and Baysal, O. "Shape Optimizing Nacelle near Flat-Plate Wing Using Multiblock Sensitivity Analysis," *Journal of Aircraft* Vol. 35, No. 1, 1998, pp. 33-38. doi: 10.2514/2.2286
34. Jameson, A., Martinelli, L., and Pierce, N. A. "Optimum Aerodynamic Design Using the Navier–Stokes Equations," *Theoretical and Computational Fluid Dynamics* Vol. 10, No. 1, 1998, pp. 213-237. doi: 10.1007/s001620050060
35. Reuther, J. "Aerodynamic Shape Optimization for Supersonic Aircraft," *32nd AIAA Fluid Dynamics Conference and Exhibit*. American Institute of Aeronautics and Astronautics, 2002.
36. Baysal, O., Ghayour, K., and Idres, M. M. "Aeroacoustic Sensitivity Analysis and Its Application for Noise Barrier Design." 2002, pp. 7-16.
37. Economon, T. D., Palacios, F., and Alonso, J. J. "An Unsteady Continuous Adjoint Approach for Aerodynamic Design on Dynamic Meshes," *15th AIAA/ISSMO Multidisciplinary Analysis and Optimization Conference, AIAA 2014-2300*. American Institute of Aeronautics and Astronautics, 2014.
38. Elliott, J., and Peraire, J. "Practical Three-Dimensional Aerodynamic Design and Optimization Using Unstructured Meshes," *AIAA Journal* Vol. 35, No. 9, 1997, pp. 1479-1485. doi: 10.2514/2.271
39. Anderson, W. K., and Bonhaus, D. L. "Airfoil Design on Unstructured Grids for Turbulent Flows," *AIAA Journal* Vol. 37, No. 2, 1999, pp. 185-191. doi: 10.2514/2.712
40. Mavriplis, D. J. "Discrete Adjoint-Based Approach for Optimization Problems on Three-Dimensional Unstructured Meshes," *AIAA Journal* Vol. 45, No. 4, 2007, pp. 741-750. doi: 10.2514/1.22743
41. Marta, A., and Alonso, J. "Discrete Adjoint Formulation for the Ideal MHD Equations," *3rd AIAA Flow Control Conference*. American Institute of Aeronautics and Astronautics, 2006.
42. Duraisamy, K., and Alonso, J. "Adjoint Based Techniques for Uncertainty Quantification in Turbulent Flows with Combustion," *42nd AIAA Fluid Dynamics Conference and Exhibit*. American Institute of Aeronautics and Astronautics, 2012.
43. Wang, L., Diskin, B., Biedron, R. T., Nielsen, E. J., and Bauchau, O. A. "High-Fidelity Multidisciplinary Sensitivity Analysis and Design Optimization for Rotorcraft

- Applications," *AIAA Journal* Vol. 57, No. 8, 2019, pp. 3117-3131. doi: 10.2514/1.J056587
44. Albring, T. A., Sagebaum, M., and Gauger, N. R. "Efficient Aerodynamic Design using the Discrete Adjoint Method in SU2," *17th AIAA/ISSMO Multidisciplinary Analysis and Optimization Conference, AIAA 2016-3518*. American Institute of Aeronautics and Astronautics, 2016.
 45. Giles, M. B., and Pierce, N. A. "An Introduction to the Adjoint Approach to Design," *Flow, Turbulence and Combustion* Vol. 65, No. 3, 2000, pp. 393-415. doi: 10.1023/A:1011430410075
 46. Biava, M., Woodgate, M., and Barakos, G. N. "Fully Implicit Discrete-Adjoint Methods for Rotorcraft Applications," *AIAA Journal* Vol. 54, No. 2, 2015, pp. 735-749. doi: 10.2514/1.J054006
 47. Baysal, O., Eleshaky, M. E., and Burgreen, G. W. "Aerodynamic shape optimization using sensitivity analysis on third-order Euler equations," *Journal of Aircraft* Vol. 30, No. 6, 1993, pp. 953-961. doi: 10.2514/3.46439
 48. Bischof, C., Corliss, G., Green, L., Griewank, A., Haigler, K., and Newman, P. "Automatic differentiation of advanced CFD codes for multidisciplinary design," *Computing Systems in Engineering* Vol. 3, No. 6, 1992, pp. 625-637. doi: [https://doi.org/10.1016/0956-0521\(92\)90014-A](https://doi.org/10.1016/0956-0521(92)90014-A)
 49. Sherman, L. L., Taylor Iii, A. C., Green, L. L., Newman, P. A., Hou, G. W., and Korivi, V. M. "First- and Second-Order Aerodynamic Sensitivity Derivatives via Automatic Differentiation with Incremental Iterative Methods," *Journal of Computational Physics* Vol. 129, No. 2, 1996, pp. 307-331. doi: <https://doi.org/10.1006/jcph.1996.0252>
 50. Mohammadi, B., and Mohammadi, B. "Optimal shape design, reverse mode of automatic differentiation and turbulence," *35th Aerospace Sciences Meeting and Exhibit*. American Institute of Aeronautics and Astronautics, 1997.
 51. Mader, C. A., Martins, J. R. R. A., Alonso, J. J., and van der Weide, E. "ADjoint: An Approach for the Rapid Development of Discrete Adjoint Solvers," *AIAA Journal* Vol. 46, No. 4, 2008, pp. 863-873. doi: 10.2514/1.29123
 52. Lyu, Z., Kenway, G. K., Paige, C., and Martins, J. R. R. A. "Automatic Differentiation Adjoint of the Reynolds-Averaged Navier-Stokes Equations with a Turbulence Model," *21st AIAA Computational Fluid Dynamics Conference*. American Institute of Aeronautics and Astronautics, 2013.
 53. Sagebaum, M., Albring, T., and Gauger, N. "High-Performance Derivative Computations using CoDiPack," *arXiv.org*, 2017.
 54. Wang, L., Diskin, B., Biedron, R. T., Nielsen, E. J., and Bauchau, O. A. "Evaluation of High-Fidelity Multidisciplinary Sensitivity-Analysis Framework for Multipoint Rotorcraft Optimization," *Journal of Aircraft* Vol. 57, No. 5, 2020, pp. 830-842. doi: 10.2514/1.C035748
 55. Fabiano, E., Mishra, A., Mavriplis, D. J., and Mani, K. "Time-dependent Aero-acoustic Adjoint-based Shape Optimization of Helicopter Rotors in Forward Flight," *57th AIAA/ASCE/AHS/ASC Structures, Structural Dynamics, and Materials Conference, AIAA 2016-1910*. American Institute of Aeronautics and Astronautics, 2016.
 56. Fabiano, E., and Mavriplis, D. "Adjoint-Based Aeroacoustic Design-Optimization of Flexible Rotors in Forward Flight," *Journal Of The American Helicopter Society* Vol. 62, No. 4, 2017. doi: 10.4050/JAHS.62.042005

57. Palacios, F., Alonso, J., Duraisamy, K., Colonno, M., Hicken, J., Aranake, A., Campos, A., Copeland, S., Economon, T., Lonkar, A., Lukaczyk, T., and Taylor, T. "Stanford University Unstructured (SU²): An open-source integrated computational environment for multi-physics simulation and design," *51st AIAA Aerospace Sciences Meeting including the New Horizons Forum and Aerospace Exposition*. American Institute of Aeronautics and Astronautics, 2013.
58. Palacios, F., Economon, T. D., Aranake, A., Copeland, S. R., Lonkar, A. K., Lukaczyk, T. W., Manosalvas, D. E., Naik, K. R., Padron, S., Tracey, B., Variyar, A., and Alonso, J. J. "Stanford University Unstructured (SU2): Analysis and Design Technology for Turbulent Flows," *52nd Aerospace Sciences Meeting*. American Institute of Aeronautics and Astronautics, 2014.
59. Economon, T., Palacios, F., and Alonso, J. "Optimal Shape Design for Open Rotor Blades," *30th AIAA Applied Aerodynamics Conference*. American Institute of Aeronautics and Astronautics, 2012.
60. Albring, T. A., Sagebaum, M., and Gauger, N. R. "Development of a Consistent Discrete Adjoint Solver in an Evolving Aerodynamic Design Framework," *16th AIAA/ISSMO Multidisciplinary Analysis and Optimization Conference*. American Institute of Aeronautics and Astronautics, 2015.
61. Economon, T. D., Palacios, F., Copeland, S. R., Lukaczyk, T. W., and Alonso, J. J. "SU2: An Open-Source Suite for Multiphysics Simulation and Design," Vol. 54, No. 3, 2016, pp. 828-846. doi: 10.2514/1.J053813
62. Burghardt, O., Gauger, N. R., Gomes, P., Palacios, R., Kattmann, T., and Economon, T. D. "Coupled Discrete Adjoint for Multiphysics in SU2," *AIAA AVIATION 2020 FORUM*. American Institute of Aeronautics and Astronautics, 2020.
63. Zhou, B. Y., Albring, T. A., Gauger, N. R., Economon, T. D., Palacios, F., and Alonso, J. J. "A Discrete Adjoint Framework for Unsteady Aerodynamic and Aeroacoustic Optimization," *16th AIAA/ISSMO Multidisciplinary Analysis and Optimization Conference*. 2015.
64. Zhou, B. Y., Albring, T. A., Gauger, N. R., Economon, T. D., and Alonso, J. J. "An Efficient Unsteady Aerodynamic and Aeroacoustic Design Framework Using Discrete Adjoint," *17th AIAA/ISSMO Multidisciplinary Analysis and Optimization Conference, AIAA 2016-3369*. American Institute of Aeronautics and Astronautics, 2016.
65. Zhou, B., Albring, T. A., Gauger, N. R., Ilario, C., Economon, T. D., and Alonso, J. J. "Reduction of Airframe Noise Components Using a Discrete Adjoint Approach," *18th AIAA/ISSMO Multidisciplinary Analysis and Optimization Conference*. 2017.
66. Donea, J., Huerta, A., Ponthot, J.-P., and Rodríguez-Ferran, A. "Arbitrary Lagrangian–Eulerian Methods," *Encyclopedia of Computational Mechanics Second Edition*. Second Edition ed., 2017, pp. 1-23.
67. White, F. M. *Viscous Fluid Flow*. New York: McGraw-Hill, 2006.
68. Spalart, P., and Allmaras, S. "A one-equation turbulence model for aerodynamic flows," *30th Aerospace Sciences Meeting and Exhibit*. American Institute of Aeronautics and Astronautics, 1992.
69. Jameson, A. "Origins and Further Development of the Jameson–Schmidt–Turbel Scheme," *AIAA Journal* Vol. 55, No. 5, 2017, pp. 1487-1510. doi: 10.2514/1.J055493
70. Saad, Y. "A Flexible Inner-Outer Preconditioned GMRES Algorithm," *SIAM Journal on Scientific Computing* Vol. 14, No. 2, 1993, pp. 461-469. doi: 10.1137/0914028

71. Farassat, F. "Derivation of Formulations 1 and 1A of Farassat," *NASA/TM-2007-214853*. NASA Langley Research Center, 2007.
72. Francescantonio, P. D. "A new boundary integral formulation for the prediction of sound radiation," *Journal of Sound and Vibration* Vol. 202, No. 4, 1997, pp. 491-509.
73. Kraft, D. "Algorithm 733: TOMP—Fortran modules for optimal control calculations," *ACM Trans. Math. Softw.* Vol. 20, No. 3, 1994, pp. 262–281. doi: 10.1145/192115.192124
74. ANSI. "American National Standard Specification for Sound Level Meters." Vol. S1.4-1983, American Institute of Physics for the Acoustical Society of America, 1985.
75. Hubbard, H. H. *Aeroacoustics of Flight Vehicles: Theory and Practice. Volume 1: Noise Sources*. Langley Research Center: NASA, 1991.
76. Lopes, L. V., Iyer, V. R., and Born, J. "Robust Acoustic Objective Functions and Sensitivities in Adjoint-Based Design Optimizations," *55th AIAA Aerospace Sciences Meeting, AIAA 2017-1673*. American Institute of Aeronautics and Astronautics, 2017.
77. Brentner, K. S., and Farassat, F. "Modeling aerodynamically generated sound of helicopter rotors," *Progress in Aerospace Sciences* Vol. 39, No. 2, 2003, pp. 83-120. doi: [https://doi.org/10.1016/S0376-0421\(02\)00068-4](https://doi.org/10.1016/S0376-0421(02)00068-4)
78. Brès, G. A., Brentner, K. S., Perez, G., and Jones, H. E. "Maneuvering rotorcraft noise prediction," *Journal of Sound and Vibration* Vol. 275, No. 3, 2004, pp. 719-738. doi: <https://doi.org/10.1016/j.jsv.2003.07.005>
79. Brentner, K. S., Brès, G., Perez, G., and Jones, H. E. "Maneuvering Rotorcraft Noise Prediction: A New Code for a New Problem." 2002.
80. Gropp, W., Gropp, W. D., Lusk, E., Skjellum, A., and Lusk, A. D. F. E. E. *Using MPI: portable parallel programming with the message-passing interface*: MIT press, 1999.
81. Karypis, G., Schloegel, K., and Kumar, V. "Parmetis parallel graph partitioning and sparse matrix ordering library," *Department of Computer Science and Engineering University of Minnesota, TR 97-060*. University of Minnesota, Minneapolis, MN, USA, 1997.
82. Squire, W., and Trapp, G. "Using Complex Variables to Estimate Derivatives of Real Functions," *SIAM Review* Vol. 40, No. 1, 1998, pp. 110-112. doi: 10.1137/s003614459631241x
83. Martins, J. R. R. A., Sturdza, P., and Alonso, J. J. "The complex-step derivative approximation," *ACM Trans. Math. Softw.* Vol. 29, No. 3, 2003, pp. 245–262. doi: 10.1145/838250.838251
84. Achenbach, E. "Experiments on the flow past spheres at very high Reynolds numbers," *Journal of Fluid Mechanics* Vol. 54, No. 3, 1972, pp. 565-575. doi: 10.1017/S0022112072000874
85. Caradonna, F. X., and Tung, C. "Experimental and analytical studies of a model helicopter rotor in hover," *NASA Technical Memorandum, 81232*. 1980.
86. Lopes, L., and Burley, C. "Design of the Next Generation Aircraft Noise Prediction Program: ANOPP2," *17th AIAA/CEAS Aeroacoustics Conference (32nd AIAA Aeroacoustics Conference)*. 2012.
87. Lopes, L., and Burley, C. "ANOPP2 User's Manual: Version 1.2," *NASA/TM-2016-219342*. NASA Langley Research Center, Hampton, Virginia, 2016.
88. "Advancement of proprotor technology. Task 1: Design study summary," *NASA-CR-114682*. Bell Helicopter Co., 1969.

89. "Advancement of proprotor technology. Task 2: Wind-tunnel test results," *NASA-CR-114363*. Bell Helicopter Co., 1971.
90. Marr, R. L. "Wind Tunnel Test Results of 25 Foot Tilt Rotor During Autorotation," *NASA-CR-137824*. Bell Helicopter Co., 1976.
91. Hanson, D. "The influence of propeller design parameters on far field harmonic noise in forward flight," *5th Aeroacoustics Conference*. 2012.
92. Schiltgen, B., Hooker, H., and Wick, A. "CFD Correlation with WT Test Data WIPP Workshop," *AIAA Aviation Forum and Exhibit - Presentation*. 2019.
93. Economon, T., Palacios, F., and Alonso, J. "Unsteady Aerodynamic Design on Unstructured Meshes with Sliding Interfaces," *51st AIAA Aerospace Sciences Meeting including the New Horizons Forum and Aerospace Exposition*. American Institute of Aeronautics and Astronautics, 2013.
94. Hooker, J. R., Wick, A., Ginn, S. R., Walker, J., and Schiltgen, B. T. "Overview of Low Speed Wind Tunnel Testing Conducted on a Wingtip Mounted Propeller for the Workshop for Integrated Propeller Prediction," *AIAA AVIATION 2020 FORUM*. American Institute of Aeronautics and Astronautics, 2020.
95. "Wind Tunnel Testing of Propeller Wingtip Interactions," *Tech. rep., NASA SBIR Phase III Final Report*. 2019.
96. Pettingill, N. A., Zawodny, N. S., Thurman, C., and Lopes, L. V. "Acoustic and Performance Characteristics of an Ideally Twisted Rotor in Hover," *AIAA Scitech 2021 Forum*. American Institute of Aeronautics and Astronautics, 2021.
97. Zawodny, N. S., Boyd, D. D., and Nark, D. M. "Aerodynamic and Acoustic Interactions Associated with Inboard Propeller-Wing Configurations," *AIAA Scitech 2021 Forum*. American Institute of Aeronautics and Astronautics, 2021.
98. Ingraham, D. "Design of a Low-Noise Propeller with Low-Order Tools - Preliminary Results," *NASA Acoustics Technical Working Group*. NASA Langley Research Center, Virtual, 2021.
99. Mayer, D., Nijso, B., Travis, C., and Economon, T. "Adjoint-based design optimization of pollutant emissions in heat exchangers," *1st Annual SU2 Conference*. SU2 Foundation, Virtual Event, 2020.
100. Romano, J. P., and Baysal, O. "An Auto-Encoder Convolutional Neural Network for Synthetic Upscaling of Computational Fluid Dynamics Simulations," *AIAA Scitech Forum 2022*. AIAA, San Diego, CA, 2022.

VITA

Ramiz Omur Icke
Department of Aerospace Engineering, Old Dominion University
Norfolk, VA 23529

EDUCATION

Ph.D., Aerospace Engineering, Old Dominion University, USA, Aug 2021.

M.S., Mechanical Engineering, Heat & Fluids, Istanbul Technical University, Turkey, Dec 2015 Thesis:
“Numerical Investigation of Aerodynamic and Aero-acoustic Properties of A Supersonic Jet,” 419068,
2015.

B.S., Aeronautical Engineering, Istanbul Technical University, Turkey, June 2011 Thesis:
“Reverse engineering of a micro turbojet.”

B.S., Astronautical Engineering, Istanbul Technical University, Turkey, June 2011 Thesis:
“Vortex-lattice code development for biplane applications.”

PUBLICATIONS

- [1] R. O. Icke, O. Baysal, L. Lopes and B. Diskin “Optimizing Proprotor Blades Using Coupled Aeroacoustic and Aerodynamic Sensitivities,” AIAA AVIATION 2021 Forum, AIAA-2021-3037, August 2-6, 2021
- [2] R. O. Icke and O. Baysal, “Wing-Tip Mounted Propeller: Analysis and Adjoint Sensitivities of Noise Generation and Propagation,” AIAA AVIATION 2021 Forum, AIAA-2021-2283, August 2-6, 2021
- [3] R. O. Icke, O. Baysal, L. Lopes, B. Y. Zhou, B. Diskin, and A. Moy, “Toward Adjoint-Based Aeroacoustic Optimization for Propeller and Rotorcraft Applications,” AIAA AVIATION 2020 Forum, AIAA-2020-3140, 2020
- [4] R. O. Icke and O. Baysal, “Extending a Multi-Physics Tool for Simultaneous CFD-CAA Simulations and Comparisons for a Mounted Propeller,” ASME IMECE 2020, IMECE2020-25319, November 16-19, 2020
- [5] R. O. Icke and O. Baysal, “Adjoint-Based Aeroacoustic Optimization for Near-Optimal Wing Placement Over Propeller,” AIAA SciTech Forum 2022, January 3-7, 2022, (Submitted/Under review)
- [6] R. O. Icke, C. Dinc, M. B. Acikgoz, S. Mestanlı, K. Anbarcı, A.R. Aslan, “Des analysis and drag prediction of a light commercial road vehicle,” 8th International Conference on Computational Heat and Mass Transfer ICCHMT8, Istanbul, Turkey, May 25-28, 2015
- [7] R. O. Icke, O. Tuncer, “Investigation of a Micro Turbojet Engine Via Reverse Engineering,” 9 Eylul University, Science and Engineering Journal, 2016, 18(3), 552-579 Doi: 10.21205/deufmd.2016185422
- [8] K. Anbarcı, B. Acikgoz, R. A. Aslan, O. Arslan, R. O. Icke, “Development of an Aerodynamic Analysis Methodology for Tractor-Trailer Class Heavy Commercial Vehicles,” SAE Technical Paper, 2013-01-2413, 2013, DOI: 10.4271/2013-01-2413
- [9] A. R. Aslan, K. Anbarcı, M. B. Acikgoz, R. O. Icke, O. Arslan, C. Dinc, “Numerical Modelling and Prediction of the effect of Cooling Drag on the total Vehicle Drag,” Eighth International Conference on Computational Fluid Dynamics ICCFD8, Chengdu, China, July 14-18, 2014, ICCFD8-2014-427